Prototype Fan Beam Optical Computed Tomography Scanner for Three-Dimensional Radiotherapy Dose Verification

by

David Rudko

BSc, University of British Columbia, 2005

A Thesis Submitted in Partial Fulfillment of the
Requirements for the Degree of

Master of Science

in the Department of Physics and Astronomy

Prototype Fan Beam Optical Computed Tomography Scanner for Three-Dimensional Radiotherapy Dose Verification

by

David Rudko

BSc, University of British Columbia, 2005

Supervisory Committee

Dr. A. Jirasek, Supervisor (Department of Physics and Astronomy)

Dr. D. Wells, Supervisor (British Columbia Cancer Agency - Vancouver Island Centre)

Dr. M. Hilts, Member (British Columbia Cancer Agency - Vancouver Island Centre)

Dr. G. Steeves, Member (Department of Physics and Astronomy)

Dr. C. Duzenli, Outside Member (British Columbia Cancer Agency - Vancouver Centre)

Supervisory Committee

Dr. A. Jirasek, Supervisor (Department of Physics and Astronomy)

Dr. D. Wells, Supervisor (British Columbia Cancer Agency - Vancouver Island Centre)

Dr. M. Hilts, Member (British Columbia Cancer Agency - Vancouver Island Centre)

Dr. G. Steeves, Member (Department of Physics and Astronomy)

Dr. C. Duzenli, Outside Member (British Columbia Cancer Agency - Vancouver Centre)

Abstract

A prototype, rapid, high precision fan beam optical computed tomography (OptCT) scanner for three-dimensional polymer gel dosimetry of complex radiotherapy protocols has been developed. This study documents the design, construction and characterization of the system, as well as preliminary reconstructed optical attenuation images and dosimetric verification experiments. The principal goal in scanner design and implementation was to satisfy the Radiotherapy Accuracy and Precision (RTAP) criteria consisting of a spatial resolution of $1\times1\times1$ mm^3, an imaging time of 60 minutes, a dose accuracy within 3% and a precision within 1%. The scanner, which employs a sixty degree fan beam of 543 nm laser light to scan irradiated polymer gel samples up to 19 cm in cross-sectional diameter, has several defining attributes. Data acquisition for a single slice through a dosimeter is achieved in

two minutes, using one signal acquisition per CT projection angle over a total of 360 projections. The effects of scatter and refraction of visible light are minimized by using the unique radial design of the matching medium tank, the concentric arrangement of a prototype, computer numerical control (CNC)-machined collimator and five Hamamatsu photodiode detector arrays for light detection. The novel tertiary collimation eliminates scattered light by 13% and improves reconstructed image contrast-to-noise ratio. Other characteristics of the scanner include: a laser power output variation of only 0.7%, signal-to-noise ratio (SNR) for calibration projections of up to 294:1, SNR for transmission projections through an irradiated polymer gel dosimeter of up to 161:1, a large absorbance dynamic range extending from 0.1 to 1.7 absorbance units and a spatial resolution of 0.25 mm^2 in the axial plane of the scanning geometry and 0.8 mm along the longitudinal z-axis of the scan plane. Images of optical attenuation coefficients and concomitant dose maps extracted from irradiated, normoxic N-isopropylacylamide (NIPAM) polymer gels were used to investigate the potential of the system for dosimetric verification. Three different NIPAM gel irradiation experiments were performed and the resultant OptCT dose distributions were compared to the Eclipse® (Varian Medical Systems, Palo Alto, CA.) treatment planning system model. While the fan beam OptCT scanner provides promising initial images of reconstructed optical attenuation coefficients, its dosimetric accuracy compared to Eclipse - nominally 7% in low dose gradient regions and 5% on the field edges - constitutes the most significant area for future refinement.

Table of Contents

List of Tables

List of Figures

Acknowledgements

The research documented in this study would not have been possible without the exceptional guidance, support and encouragement of a few key people. First and foremost, I would like to thank my two supervisors, Dr. Derek Wells and Dr. Andrew Jirasek. Each contributed his unique perspective to the development of the OptCT project. Derek's contributions to my understanding of computed tomography theory, radiation therapy dosimetry, treatment planning and medical image processing greatly enhanced this research. Andrew's thoughtful discussions and guidance with the programming involved in this project were an immense benefit, as was his patient assistance with polymer gel preparation and the characterization portion of the study. Most important of all, both Andrew and Derek were outstanding role models of what is essential to become successful in the field of medical physics.

My experience as a graduate student in the Medical Physics program at the University of Victoria has been incredibly rewarding thanks to the stimulating work with fellow graduate students and professors in the Physics and Astronomy Department, as well as the motivating interactions with the Medical Physics Group at the Vancouver Island Cancer Center. In particular, I'd like to acknowledge three fellow students in the Medical Physics graduate program. Quinn Matthews was a great friend and cohort during the rigours of first year graduate courses. Karl Bush continually provided leadership and support during my work in the Physics Department at the Vancouver Island Cancer Center. And last but certainly not least, Conor Shaw's good-natured perspective on life and graduate school helped preserve my sanity - as did his dragging me away from my desk and out into the Victoria sun periodically during the course of writing this thesis. I wish all three the very best in their continued careers

in the field of Medical Physics.

The construction of the OptCT scanner itself was expeditiously facilitated with the technical assistance of the University of Victoria Electronics Department and both the machine shop and electronics shops at the Vancouver Island Cancer Center. I am particularly grateful to Nick Braam for the significant amount of time he devoted to constructing and programming the microcontroller circuit board for the project, Mark Lenckowski and Neil Honkanen for their patient and exacting help with the design and construction of the collimator and Steve Gray and Dave Yardley for their precise and tireless machining work on the matching medium tank, initial prototype collimator and general construction elements of the scanner.

Finally, special thanks to my Father, Mother and Grandfather for their unwavering support, interest and encouragement during this project.

Chapter 1

Introduction

Rapid advances in three-dimensional, conformal and intensity-modulated radiation therapy have created a pivotal need for precise, high-resolution, three-dimensional dose verification methods [1]. Currently, conformal radiation treatment techniques can deliver an escalated dose to a cancerous tumour while minimizing the dose to surrounding healthy tissue. However, because of the very high dose gradients used, an error in spatial dose distribution can lead to serious complications. To utilize new radiation delivery technologies effectively, accurate measurement systems are needed for mapping, to millimetre resolution, cumulative three-dimensional dose distributions in phantoms. Additionally, such measurement systems must be compared with the radiotherapy treatment plan. Current dosimetry measurement systems, including ion chamber, film and electronic portal imaging dosimeters do not provide a simultaneous, three-dimensional measurement of the radiation therapy beam in a tissue equivalent medium. This study focuses on the development, characterization and preliminary dosimetric results of a prototype, fan-beam optical computed tomography (OptCT) scanner for radiotherapy dose verification with a normoxic, N-isopropylacrylamide (NIPAM) polymer gel dosimeter.

1.1 Radiation Therapy

The first chapter is partitioned into four sections. Section 1.1 presents an overview of the radiation therapy process. Current radiation therapy dosimetry methods are outlined in section 1.2. In section 1.3, the most prominent three-dimensional dosimeters are described. Lastly, imaging modalities used for dosimetry verification with three-dimensional dosimetry are described in section 1.4.

1.1.1 Overview of The Radiation Therapy Process

In clinical radiation therapy, megavoltage (>1 MV) photons or electrons produced by a medical linear accelerator are used to deliver high-energy to a tumour volume. The goal of this ionization radiation delivery is to deposit a lethal dose to the tumour site while ensuring minimal damage to the surrounding normal tissue [1]. This is accomplished by conforming the dose to a planning target volume (PTV) which includes the tumour, as well as a margin accounting for microscopic disease, patient setup errors and tumour motion [2]. The PTV, a static volume used only for treatment planning, can be considered a three-dimensional delineation of the region where dose would be ideally deposited within the patient. Localization of the tumour volume, identification of the anatomical structures at risk and determination of the PTV comprise part of the radiotherapy treatment planning stage initiated before treatment delivery [3]. Optimum beam configuration for irradiating the PTV and calculation of the resultant dose distribution are also determined at this point. Essentially, radiotherapy planning translates the therapeutic strategy of the radiation oncologist into a set of treatment instructions which can be directly implemented by a radiation therapist [2].

Prior to treatment, a patient normally undergoes an x-ray computed tomography (x-ray CT) scan [4] which yields a set of cross-sectional, two-dimensional images of patient anatomy (figure 1.1). The set of reconstructed x-ray CT images is then

uploaded into a software treatment planning system which uses the images in the process of dose calculation. During this process, a medical physicist (or dosimetrist) and a radiation oncologist decide on the optimal number, angular arrangement, energy and shape of the radiation fields for the treatment [2].

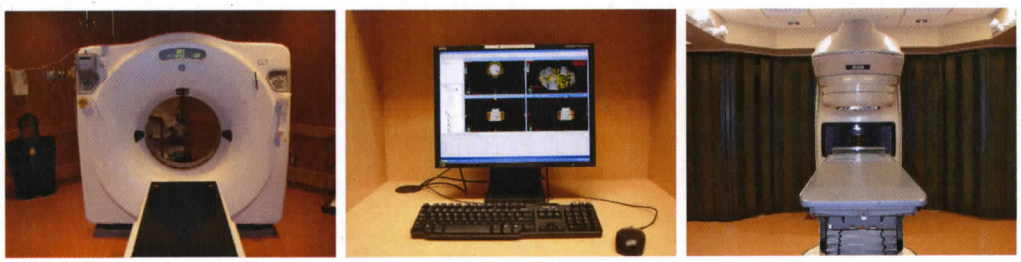

(a) (b) (c)

Figure 1.1: Radiotherapy planning and delivery: cross-sectional, two-dimensional attenuation maps of patient contour are acquired using (a) an x-ray computed tomography scanner. The data is uploaded into (b) a software treatment planning system. (c) A medical linear accelerator (LINAC) is normally used to deliver the planned treatment.

Once the planning stage is complete and the medical physicist and radiation oncologist have approved treatment, radiation therapists deliver the treatment to the patient using, typically, a medical linear accelerator (LINAC). This process is described in the following section.

1.1.2 Radiation Delivery with Medical Linear Accelerators

Most external beam radiation therapy treatments are delivered using a LINAC. When the accelerator beam is initially activated, microwave frequency electromagnetic waves (~3000 MHz) accelerate electrons discharged from an electron gun in the accelerator waveguide to relativistic velocities [3]. The electron beam exits the waveguide as a pencil beam approximately 3 mm in diameter [5]. This beam is then bent directly towards the patient using a 270^o bending magnet and either passes directly to the patient via a scattering foil (electron therapy) or strikes a high atomic number target such as tungsten, producing a broad, forward-peaked energy distribution

of bremsstrahlung photons (photon therapy) [2]. Because megavoltage photons are more penetrating than electrons, the choice of delivery mode (photons or electrons) is largely dictated by the location of the tumour.

The treatment beam is collimated by a fixed primary collimator located directly below the photon target (figure 1.2). Such an arrangement allows only forward scattered photons to escape the linear accelerator head and greatly reduces scattered photon leakage [2].

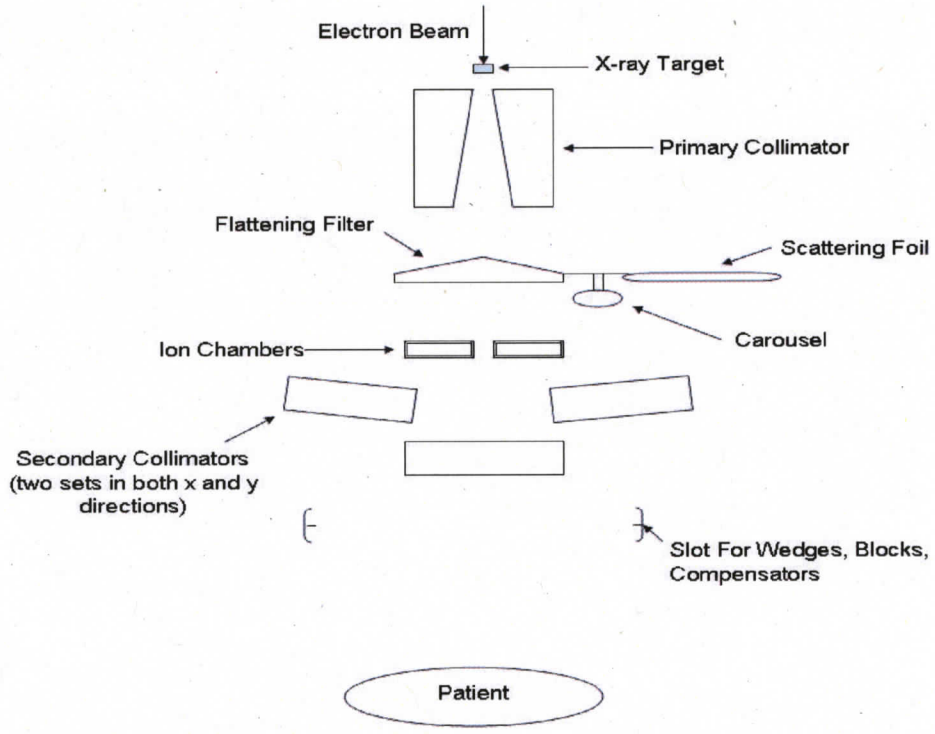

Figure 1.2: Components of a typical medical linear accelerator head

If a photon beam is being produced, the energy profile of the beam is flattened using a cone-shaped, tungsten or lead alloy flattening filter located below the primary collimator [5]. The flattening filter is thicker towards the center to compensate for the forward peaked, bremsstrahlung spectrum. If an electron beam is produced, the target and flattening filter are replaced by a thin lead scattering foil which spreads the electron beam and produces a uniform fluence across the treatment field [3]. Below

the flattening filter, two dose monitoring ionization chambers are used to verify the dose rate, integrated dose and symmetry of the treatment beam.

Secondary collimating jaws consisting of two tungsten or metal alloy blocks approximately 8 cm in thickness are mounted below the monitor ionization chambers. The collimators can move in and out of the beam to allow definition of fields up to 40×40 cm^2 in cross-sectional area [2]. Modern linear accelerators also use a variety of tertiary collimation devices positioned below the secondary collimator jaws to further shape the rectangular photon field into a specific geometry before it exits the linear accelerator head. The most common tertiary collimation system today is the multi-leaf collimator (MLC) (figure 1.3). MLCs are sets of up to 120 computer-programmable, interleaving, thin lead or tungsten leaves which allow for customized field apertures as well as rapid, real-time adjustment of the field geometry and intensity during the course of a treatment. Other tertiary collimation systems, placed below the secondary collimator for modulating field intensity, include static wedges, dynamic wedges and compensators. These devices are variable thickness absorbers placed below the secondary collimator jaws to modify the photon beam fluence. For electron therapy, the secondary collimator and MLCs are not used, since electrons scatter more readily in air than do photons. Field apertures are defined by an auxiliary electron collimator which extends down to the surface of the patient skin [5] to reduce lateral electron scatter in air. The electron collimator is usually made of lead, tungsten or cerrobend and is shaped to define the desired field dimensions.

During the delivery of radiation therapy, the therapist positions the patient on a computer-controlled treatment couch which allows vertical, horizontal, and rotational movement for patient position adjustment. For a single fraction radiation treatment, multiple fields of radiation are typically delivered from different angles, while the fluence of the photon beam is modulated using one or more of the aforementioned collimation devices.

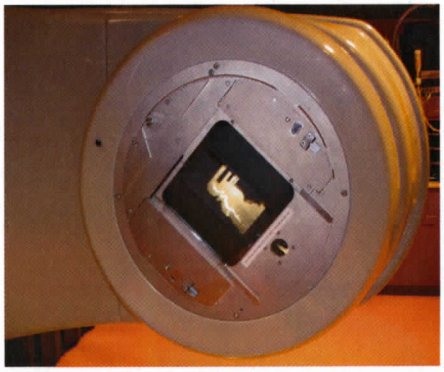

Figure 1.3: Multi-leaf collimator arrangement.

1.1.3 Modern Radiation Therapy

Modern radiation therapy delivery methods such as intensity-modulated radiation therapy (IMRT), intensity modulated arc therapy (IMAT), tomotherapy, and image-guided radiation therapy (IGRT) employ advanced beam shaping and fluence modulation strategies to enhance the conformation of the absorbed dose to the tumour volume. These techniques also produce extremely sharp gradients between regions of high and low dose. This subsection introduces the basic principles of conformal and intensity modulated radiation therapy.

Three parameters are manipulated to deliver a dose distribution that better conforms to the tumour volume: the number and orientation of the radiation beams, the shape of each beam, and the intensity of radiation within each beam. Modern intensity modulated techniques employ computer-controlled, MLCs for shaping the beam aperture and delivering each dynamically modulated field. In conventional, sliding window IMRT, opposing collimator leaf pairs sweep simultaneously and unidirectionally across the treatment field with different velocities as a function of time [5]. The goal of treatment planning with IMRT is to deliver the planned intensity modulated dose profiles within the constraints of maximum possible leaf velocity and minimum treatment time.

Intensity modulated arc therapy (IMAT) is an extension of IMRT. In IMAT,

the MLC is used to shape the fields while the gantry rotates in an arc therapy mode. Tomotherapy is yet another intensity modulated delivery method in which the patient is treated in a slice by slice manner analogous to CT imaging, while a special collimator generates the treatment fields [5]. The latest treatment delivery technique is image-guided or adaptive radiation therapy, where x-ray CT or portal images of the patient, acquired immediately prior to or during the course of treatment may be used to modify the treatment delivery in order to compensate for organ or patient motion.

1.1.4 Uncertainties in the Radiation Therapy Process

Although the ultimate goal of radiation therapy delivery is to eradicate tumorous tissue based on a precise, computer-generated treatment plan, the implementation of a fractionated, radiation delivery conforming exactly to the treatment plan is not always possible. Geometric uncertainties such as patient set-up errors, organ motion during treatment and patient body movement, as well as dosimetric uncertainties such as daily variations in linear accelerator output, MLC fluence variations between planned and delivered treatments, treatment planning algorithm deficiencies and mechanical misalignment of treatment fields contribute to inaccuracies in the radiotherapy delivery process.

Numerous studies have noted that substantial organ motion and deformation, patient movement and daily setup error in patient positioning can occur during a radiotherapy treatment [6]. As a result, the received dose distribution differs from the planned dose distribution. Organ motion can occur either during a treatment fraction (intra-fractional) or between treatment fractions (inter-fractional) [7]. Inter-fractional organ motion occurs when either the tumour position changes on a day-to-day basis (usually associated with organs adjacent to the digestive system) or the patient undergoes significant weight gain or loss.

Respiratory and cardiac motions are considered the main source of intra-fractional

organ motion and are prevalent throughout the thorax and abdomen. Breath-hold and free-breathing gated radiotherapy methods have been implemented to synchronize the radiotherapy treatment with patient breathing [8]. These techniques employ an image-guidance or spirometry system to track physiological breathing and coordinate the treatment beam-on time with a fixed phase of the respiratory cycle [8]. Inaccurate patient positioning during setup is another serious source of geometric uncertainty in radiation therapy.

Both variations in patient positioning and breathing-induced dose inaccuracies can be minimized with the help of positioning systems and rigid immobilization devices. However, these devices place constraints on the patient's anatomy which can cause unwanted discomfort over the course of an extended treatment.

Dosimetric variables can also contribute to the received dose distribution differing from the planned dose distribution. Miscalibration of the therapeutic beam and mechanical misalignment of the treatment field are two sources of uncertainty in the mean absorbed dose to the target volume. Various machine quality assurance tests are performed on a weekly and monthly basis and include, for example, checks of beam output energy and symmetry [2].

1.2 Current Radiation Therapy Dosimetry Methods

The increasing complexity of modern radiation therapy delivery underlines a need for a comprehensive, practical method for measuring three-dimensional dose distributions in the treatment room. In view of the aforementioned uncertainties in the radiotherapy process, a radiotherapy dosimeter should ideally provide a three-dimensional, simultaneous measurement of the treated volume and be highly tissue equivalent. Additionally, it should facilitate comparing the reading extracted from the dosimeter to the dose distribution modeled by the planning system. The following subsection, which discusses current dosimetry methods employed in radiotherapy,

supports the need for three-dimensional dosimetry.

Radiation therapy dosimeters measure the absorbed dose, D, or dose rate, $\dot{D}$, resulting from ionizing radiation interaction with matter [9]. The absorbed dose, D, is the expectation value of the energy, ϵ, deposited in matter per unit mass at a point:

$$D = \frac{d\epsilon}{dm} \tag{1.1}$$

Dose is typically measured in the SI unit, Gray (Gy), where 1 Gy = 1 $\frac{\text{J}}{\text{Kg}}$. A dosimeter provides a reading which can be related to the absorbed dose using a calibration measurement. The goal of this measurement is not to determine absorbed dose in the dosimeter medium, but rather to determine an equivalent measure of absorbed dose in the tissue-equivalent medium where the dosimeter is located.

1.2.1 Ion Chamber Dosimetry

The most common point dosimeter used in current radiotherapy is the cavity ionization chamber which consists of a solid (usually graphite) envelope surrounding a gas-filled cavity in which an electric field is established to collect ion-pairs produced by ionizing radiation interacting with the gas volume. Cylindrical ion chambers having gas volumes from 0.1-3 cm^3 are the most common. A TG-51 protocol, for clinical reference dosimetry of external photon beams with nominal energies between ^{60}Co and 50 MV and electron beams with nominal energies between 4 and 50 MeV, has been established to measure the absorbed dose to water when using the cavity ionization chamber [10]. In the TG-51 protocol, the dose to water, D_w, is related to the corrected ionization chamber electrometer reading, $M_{corrected}$, by the absorbed dose to water calibration factor for a Cobalt-60 beam, $N_{D,W}^{^{60}Co}$, and the quality conversion factor, k_Q, for a beam of quality Q [10]:

$$D = M_{\text{corrected}} k_Q N_{D,W}^{^{60}Co} \tag{1.2}$$

In order to obtain $M_{corrected}$, the raw exposure readings taken from the electrometer, M_{raw}, must be adjusted for changes in temperature and pressure, incomplete collection of charge in the ion chamber and leakage or drift of the instrument readings in the absence of the radiation being measured. These correction steps, as well as the high atomic number of the metal envelope surrounding the cavity ionization chamber, are the main sources of uncertainty leading to inaccurate dosimetry when using cavity ionization chambers [11].

1.2.2 Thermoluminescent Dosimetry

The thermoluminescent dosimeter also provides point measurements of absorbed dose in radiation therapy. Thermoluminescent dosimeters (TLDs) are nonconducting, inorganic crystals most commonly available either sieved as 75-150 μm grains or in 3.2 mm square pellets 0.9 mm thick [9]. When irradiated, they absorb ionizing radiation. When heated, the crystals emit optical light in proportion to the amount of radiation energy absorbed. TLDs are strong alternatives to ion chamber dosimetry for measuring kilovoltage x-rays and performing dosimetry in regions where the treatment planning software provides inaccurate estimates of the absorbed dose. They have a response that is dose-rate independent over a range from 0 - 10^9 $\frac{\text{Gy}}{\text{s}}$, can be re-used and achieve a reading accuracy of 1-2% with proper handling and care. However, because of their small size, they cannot provide a full field measurement of the radiation beam. As well, most TLDs are composed of organic crystals such as Lithium-Fluoride doped with Titanium and Magnesium and, therefore, are not tissue equivalent. Moreover, because of the differing composition of each TLD, the response of these dosimeters varies from one TLD chip to the next.

1.2.3 Radiographic Film Dosimetry

A second class of radiation dosimeters acquires two-dimensional readings which can be related to absorbed dose and includes film and electronic portal imaging detec-

tor arrays. Radiographic film is an integrating, two-dimensional, relative dosimeter consisting of a clear polyester base coated on one or both sides with a radiosensitive emulsion. The emulsion is composed of silver halide crystals with diameters of 0.2-2 μm suspended in a high-quality, clear gelatin. The film undergoes a chemical change and blackens in response to ionizing radiation. The darkening film can be assessed quantitatively using a film densitometer which measures optical density (OD), defined as $\log_{10}(\frac{I_o}{I})$ where I_o is the light intensity measured from the source in the absence of film and I is the intensity transmitted through the film in a direction perpendicular to its plane.

Radiographic film possesses several advantages. If the fluence is not exceedingly large, OD is proportional to fluence and concomitantly, to dose in the emulsion. Although the specific dose response characteristics vary from one film dosimeter to the next, over useful dose ranges, the standard density of an irradiated film is proportional to dose and shows an independent response as a function of dose rate (except at very high and very low dose rates). In addition, the flat shape of film allows collection of a full set of central axis depth dose data which is extremely laborious and time-consuming to collect when using an ionization chamber. A disadvantage of film dosimetry, however, is its energy dependent response to dose. In particular, the high atomic number of silver bromide grains constituting the film emulsion gives rise to the photoelectric effect for x-rays below 100 keV, causing the film to absorb x-ray energy 10-50 times more readily than for energies above 100 keV [9]. Among other disadvantages, film is not re-usable, not strongly tissue equivalent, its response to dose is temperature and humidity dependent and it is only able to measure dose in a two-dimensional plane.

1.2.4 Electronic Portal Imaging Dosimetry

An electronic portal imaging device (EPID) consists of a semiconductor detector array system in which each pixel houses a light sensitive photodiode and a thin film

transistor to enable readout [9]. Electric charge generated by incident photons is accumulated in the photodiodes until the signal is read out and digitized through an analogue to digital converter. Overlaying the array of photodiodes is a scintillating layer of gadolinium oxysulphide and a copper plate of 1 mm thickness, making the portal imager an indirect detection system. The phosphor scintillator converts incident radiation into optical photons, enhancing the sensitivity of the detector accordingly. Dose is indirectly obtained from a measurement of fluence by the photodiode array [3]. The small size and concomitant high spatial resolution of semiconductor detectors, combined with their capability to perform real-time dosimetry on patients in the treatment position, make EPID devices very useful for radiation therapy dosimetry. However, diode arrays show a non-linear energy and dose-rate dependence at high energies and require re-calibration for clinical use. As well, many EPID imaging systems display a directional dependence in reconstructed images [2].

1.3 Three-Dimensional Dosimeters

In contrast to the traditional dosimeters described above, three-dimensional dosimeters, in the form of gels or polyurethane plastics, are ideally suited to modern radiation therapy dosimetry and have an effective atomic number and mass attenuation coefficient very close to that of water. Such dosimeters can also be shaped or placed in a specifically molded container to mimic any volume of interest.

Three-dimensional, integrating dosimeters record a quantitative chemical change in a liquid or solid or gaseous volume when irradiated. Polymer gel dosimeters, which are used in this research, form a precipitate consisting of cross-linked, carbon-based monomers spatially retained in a gelatin matrix. Using MRI, OptCT, or x-ray CT, a particular physical property of the polymer precipitate can be imaged and related to the dose deposited in the gel by using a calibration curve [12].

The following subsection focuses on the most prominent three-dimensional dosime-

ters used in radiotherapy and highlights the dose-response mechanisms that occur in response to megavoltage irradiation.

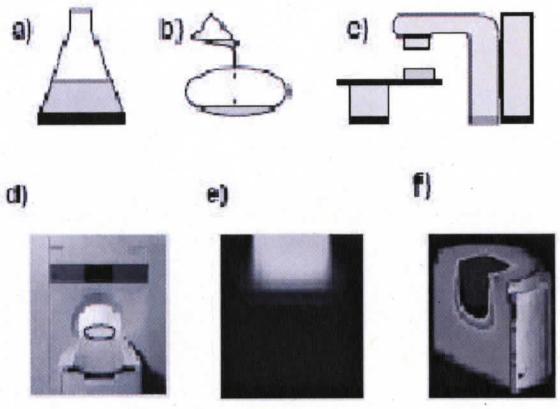

Figure 1.4: Schematic of (a/b) gel preparation, (c) irradiation, (d/e) imaging and (f) dosimetric analysis of polymer gel dosimeters

1.3.1 Types of Three-Dimensional Dosimeters

Since the first use of a ferrous sulphate (Fricke) dosimeter for three-dimensional radiotherapy verification in 1984 [13], a variety of aqueous chemical and solid three-dimensional dosimeters have been utilized for experimental dosimetry. The three most prevalent volumetric dosimeters are the Fricke dosimeter, the polymer gel dosimeter and the newly introduced PRESAGE, polyurethane dosimeter.

The ferrous sulphate (Fricke) gel dosimeter is composed of an aqueous solution of ferrous ion, (Fe^{2+}) [14]. Its dosimetric basis is the dose dependent oxidizaton of ferrous (Fe^{2+}) ions into ferric (Fe^{3+}) ions. When the dosimeter volume is irradiated, a water radiolysis reaction occurs in which the hydrogen atoms produced react with oxygen to produce the hydroperoxy radical [14]:

$$H\bullet + O_2 \longrightarrow HO_2\bullet \tag{1.3}$$

This preliminary reaction initiates the conversion of ferrous (Fe^{2+}) to ferric (Fe^{3+}) ions.

Upon irradiation, the change in concentration of ferric ion in the Fricke solution is directly proportional to the dose deposited in the gel matrix. The dose absorbed by an irradiated Fricke dosimeter can be determined by measuring the concentration change of Fe^{3+} [14] in the irradiated region of the gel. In Fricke gels, however, ferric ion diffusion leads to blurring of the dose distribution within minutes after irradiation [15]. Fricke solutions with either gelatin, agarose, sephadex and polyvinyl alcohol gelling agents or chelating agents such as xylenol orange have been investigated to reduce the ferric ion diffusion problem. The results of these studies indicate that, although the diffusion coefficient of ferric ions can be reduced to values as low as $1-1.4\times10^{-3}\frac{cm^2}{hr}$ with the use of gelatin in concentrations of 8% by weight or polyvinyl alcohol in a concentration of 20% by weight, the loss of dose sensitivity with higher gelatin concentrations and the appreciable (although reduced) ion diffusion still make the diffusion problem a significant impediment to gel dosimetry using Fricke aqueous dosimeters.

Polymer materials were first used for radiation dosimetry in 1954 when Alexander et al. examined the effects of ionizing radiation on an aqueous solution of polymethylmethacrylate [16]. Subsequently, Audet and Schreiner successfully utilized polymer gels in a radiotherapy application in 1991 by performing relaxation measurements on irradiated polyethelene oxide [17]. Since then, a variety of polymer gel formulations have been explored as potential candidates for three-dimensional radiotherapy dosimetry. The two most widely studied formulations have been polymethacrylic-acid-based and polyacrylamide-based gels [18]. Although such dosimeters have differing chemical compositions, the fundamental process of polymerization occurring in response to radiation is similar [19]. A polymerization reaction occurs where the cross-linking of the monomers induced by the free radical products of water radiolysis yields a precipitate sustained in the gelatin matrix [18]. Additionally, experimental and environmental factors such as gel irradiation temperature, time between prepa-

ration and irradiation and time between irradiation and imaging can differentially affect all such polymer gels. When a polymer gel is irradiated, a radiolysis reaction occurs where water molecules in the dilute aqueous solution are ionized to produce primary radicals:

$$H_2O + \text{Ionizing Radiation} \longrightarrow [H_2, H_2O_2, e^-_{aq}, H\bullet, OH\bullet, H_3O^+, H_2O^*] \qquad (1.4)$$

Such primary radicals react in an initiation step with monomers in the gel solution to generate cross-linked polymer chains suspended in the hydrogel matrix. The concentration of precipitated monomer is dependent on dose. Because oxygen reacts with primary radicals formed in the radiolysis reaction and diminishes the radiation-induced polymerization levels in the gel, an oxygen scavenging chemical is added to prevent inhibition of the polymerization. The presence of gelatin enhances the spatial stability of the polymer which forms and reduces the rate of polymerization.

Polyacrylamide (PAG) gel dosimeters rely on the radiation induced copolymerization of acrylamide and bisacrylamide monomers in an aqueous gel matrix of either agarose or gelatin [20]. These gels are composed of 3% by weight acrylamide, 3% bisacrylamide, water (89% by weight), and small amounts of an oxygen scavenging agent such as tetrakis-hydroxymethyl-phosphonium chloride (THPC). In the case of the present study, N-isopropylacrylamide was used in lieu of acrylamide because of the high toxicity of acrylamide in pure form. This type of polymer gel is termed NIPAM [21]. As the system is irradiated, growing polymer chains containing reactive pendant double bonds are steadily formed in the aqueous gel phase. Many of these reactive bonds undergo intramolecular cross-linking with radicals at the end of their own chain, resulting in cyclization of the monomer subunits [20]. However, some unreacted pendant-double bonds are still available for intermolecular cross-linking [20]. The resultant intermolecular cross-linking of polymer and monomer chains forms a

precipitate in the gel matrix known as the polymer phase (figure 1.5).

Figure 1.5: Top view of an N-isopropylacrylamide (NIPAM) polymer gel irradiated with 3×3 cm^2 square photon field. The irradiated square region where dose has resulted in polymerization is visible.

The PRESAGE dosimeter is a three-dimensional radiochromic plastic composed of a clear polyurethane (elemental composition of 61% C, 9% H, 10% N, and 20% O to give a $Z_{eff} = 6.6$ with a mass density of 1050 $\frac{kg}{m^3}$) combined with the leuco-dye (usually leuco malachite green, although the choice of dye can be altered depending on the wavelength of laser light used for reading-out the gel) [12]. The dosimeter is manufactured by reacting an equivalent of commercially available polyol with two equivalents of a di-isocyanate to form a pre-polymer "A" [22]. A free radical initiating leuco dye and a catalyst are then mixed with a commercially available polyol to form pre-polymer "B". The pre-polymers "A" and "B" are next mixed in equal proportions and blended. The material is placed in the appropriate mold and incubated at an optimal temperature under 60 psi to minimize gassing [22].

Irradiation of the PRESAGE dosimeter results in radiolytic oxidation of the leuco dye, yielding a visible absorbance maximum (633 nm for leuco malachite green) corresponding to the helium-neon laser output (633 nm for red light). Although PRESAGE dosimeters are not suitable for magnetic resonance imaging, they can be used with OptCT scanning [12].

1.4 Imaging/Readout of Three-Dimensional Dosimeters

In 1984, John Gore demonstrated that changes in the nuclear magnetic resonance relaxation properties of irradiated ferrous sulphate (Fricke) dosimeters could be quantified to the degree that conversion of ferrous ions (Fe^{2+}) to ferric ions (Fe^{3+}) by ionizing radiation alters the magnetic moment and electron spin relaxation times of hydrogen ions in solution [13]. Since then, various readout modalities have been utilized to determine the dose distribution within a three-dimensional dosimeter. For instance, magnetic resonance imaging, optical computed tomography, x-ray computed tomography, ultrasound and Raman spectroscopy have all successfully extracted dose information from an irradiated matrix of a three-dimensional dosimeter. The mechanism for dose readout with each of these modalities is outlined in the following subsections.

1.4.1 Magnetic Resonance Imaging

Nuclear magnetic resonance (NMR) was the first modality used to measure dose distributions in three-dimensional dosimeters [13]. The spin relaxation times (T1 and T2) of the hydrogen nuclei of water molecules in the dosimeter solution are reduced significantly upon irradiation with megavoltage x-rays [12]. In polymer gels, localized polymerization of monomer species decreases the longitudinal (T1) and transverse (T2) relaxation times of water protons in the vicinity of the polymer chains by magnetization exchange between the polymer and water protons [23]. The changes in T1 and T2 relaxation times are then measured using standard NMR pulse sequences such as Hahn spin-echo, multiple spin-echo or Carr-Purcell Meiboom Gill sequences [24].

A spatial map of T1 or T2 relaxation times reconstructed in a magnetic resonance image can be related to the dose distribution in a three-dimensional dosimeter because the R1 (1/T1) and R2 (1/T2) relaxation constants are linearly correlated with the

absorbed dose [25]. A plot of R2 vs. dose, known as a calibration curve, is derived from calibration samples in gel vials irradiated to known doses.

The principal disadvantages of conventional MR imaging of polymer gels are the relatively long imaging time (on the order of hours) required to obtain precise T2 values, as well as the lack of availability of MR scanners in some hospitals and research centers due to high patient throughput. Moreover, MRI is susceptible to geometrical distortions in reconstructed images because of deviations in the magnetic field distribution of the scanner during excitation or signal acquisition. The deviations arise from machine related sources such as eddy currents, main magnetic field inhomogeneities and gradient non-linearity [26].

1.4.2 X-Ray Computed Tomography

X-ray computed tomography was first used as a method of extracting dose information from irradiated polymer gels in 1999 [27]. The accessibility of x-ray CT scanners in hospitals and radiation therapy centers make them an attractive modality for dosimeter read-out. To date, most x-ray CT imaging has been performed by imaging polymer gels using commercially available kilovoltage CT scanners. A series of projection measurements are obtained which represent measurements of attenuation of a fan beam of x-rays through a polymer gel.

The radiation-induced polymerization of gels results in an increase in local density, $\Delta\rho_{gel}$, which is proportional to CT number (ΔN_{CT}) recorded in a reconstructed x-ray CT image [27]:

$$\Delta\rho_{gel} = K\Delta N_{CT} \tag{1.5}$$

In equation 1.5, K is a constant which is a function of the un-irradiated gel density. It has an approximate value of one for polyacrylamide gel dosimeters [27]. The dose is determined from a calibration curve displaying N_{CT} as a function of dose

for calibration vials irradiated to different doses. The x-ray CT dose response for a standard polyacrylamide gel is mono-exponential with a saturation dose of 25 Gy [27].

Currently, one factor limits the widespread use of x-ray CT in three-dimensional dosimetry research. The density changes occuring in irradiated polymer gels are small (1%), resulting in low image contrast in x-ray CT polymer gel images.

1.4.3 Optical Computed Tomography

The measurement of three-dimensional dose distributions using optical computed tomography was first introduced by Gore and Maryanski in 1996 [28]. The principle employed for extracting radiation-induced dose distributions from changes in the optical density is similar to that used in x-ray computed tomography. Specifically, a cross-sectional image of an object is constructed from a series of projection data measurements recorded at different angles around the sample. Projection data is collected by passing a linear, parallel or broad monochromatic beam of laser light through the dosimeter volume and recording the intensity of light rays on the exit side of the dosimeter.

According to Beer's Law, the OptCT laser beam is attenuated exponentially when passing through a two-dimensional slice of the dosimeter [28]:

$$I(x) = I_o e^{-\int \mu(x,y)dy} \tag{1.6}$$

where I_o represents the intensity of the laser beam before passing through the dosimeter, I(x) represents the attenuated intensity of the beam after passing through the dosimeter and $\mu(x, y)$ denotes the set of optical attenuation coefficients in the gel matrix. The projection data, I(x), is collected at equally spaced angles around the dosimeter, allowing reconstruction of optical attenuation coefficients in the dosimeter using the filtered backprojection method. A complete description of this recon-

struction algorithm is given in chapter two. The spatial map of optical attenuation coefficients, $\mu(x, y)$, in a reconstructed OptCT image can be related to the dose distribution in a three-dimensional dosimeter, since the magnitude of optical attenuation coefficients is linearly correlated with absorbed dose over a useful range dictated by the dosimeter ($\sim$ 0 - 10 Gy for polyacrylamide-based gel dosimeters).

Because of short scanning times (on the order of seconds to minutes for a single slice), high signal-to-noise ratios for reconstructed images and low cost (OptCT scanners cost between one and two orders of magnitude less than MR systems), optical scanners present an attractive alternative to current imaging modalities. However, refraction, reflection, and scattering artefacts present in reconstructed OptCT images can perturb dose information. Refractive index variations in the dosimeter and matching liquid, as well as refractive index mismatch between the matching liquid and the wall of the dosimeter, can cause rays of the laser light source to refract and cross. When fan beam rays deviate from their straight ray paths they are recorded in the wrong detector element and this may lead to unwanted bright and dark regions in a reconstructed image [29]. Nonetheless, several methods can be used to counteract these phenomena, including close matching of the refractive index bath to the three-dimensional dosimeter, tertiary collimation of the light source, post-processing of data, iterative reconstruction methods and changes in chemical composition of the dosimeter solution [30].

1.4.4 Other Methods

Ultrasound imaging and Raman spectroscopy have also been employed in imaging three-dimensional polymer gel dosimeters. In 2002, Mather et al. utilized ultrasound imaging to examine both the dose dependence of the speed of sound and the ultrasound attenuation coefficient for polyacrylamide gels (PAG) and methacrylic acid-based (MAGIC) gels prepared in cuvettes [31]. Ultrasound attenuation displayed the most noticeable response over a dose range of 0-50 Gy. Further work is necessary to

confirm the reproducibility of these early results and extend them to more realistic radiotherapy dosimetry situations.

Fourier transform Raman spectroscopy has been employed in the direct monitoring of acrylamide monomer consumption and polymer chain formation following irradiation in polymer gel dosimeters [19]. In 2003, Rintoul et al. described the potential of FT-Raman spectroscopy for ionizing radiation dosimetry using PAG gels [32]. This work demonstrated that the integrated peak areas of the acrylamide (1285 cm^{-1}) and bis-acrylamide (1256 cm^{-1}) vinyl, δCH_2 vibrational bands varied according to an expected percent depth dose curve (peak area decreased with depth). The Raman technique is more direct than MRI dosimetry in that the compositional changes detected are more closely related to radiation induced copolymerization than are NMR relaxation time changes. However, Raman spectroscopy measurements over a full three-dimensional volume are not feasible in a clinical setting because of the lengthy time required (many hours) to make measurements of a full, three-dimensional dosimeter.

1.5 Thesis Scope

This thesis outlines the design, construction, characterization and preliminary dosimetric results of a prototype, fan beam optical computed tomography scanner for three-dimensional radiotherapy verification.

The first section of this study presents the design and development of the prototype, fan beam OptCT scanner. The apparatus has several defining attributes. It uses a unique, CNC-machined, 1.5 cm thick acrylic collimator and matching medium tank to maximally reject stray light. Dosimeters 10 cm in height can be scanned in three hours and 20 minutes (two minutes/slice) using one signal acquisition per angle over a total of 360 projection angles in a reconstructed slice. The system is designed to be modular and easily scalable to image gels as large as 19 cm in cross sectional di-

ameter. Further, the absence of large telecentric lenses present in parallel-beam CCD scanners minimizes optical aberration artefacts, sometimes present in parallel-beam systems.

In the second section of this thesis, a series of commissioning tests developed to analyze the spatial resolution, precision and accuracy of the system are described and provide benchmarks for the imaging quality possible with the scanner. The precision of individual transmission and calibration projections, as well as the the accuracy of reconstructed images of an irradiated polymer gel, are then quantified using standard error and signal-to-noise ratio.

In the final section of this research, the performance of the fan beam scanner for dose readout is evaluated by comparing OptCT dose maps with modeled dose distributions from the Eclipse (Varian Medical Systems, Palto Alto, CA) treatment-planning system. Three different irradiations of a NIPAM gel (5% by weight gelatin, 89% water, 3% N-isopropyl-acrylamide and 3% N,N-methylene-bis-acrylamide) dosimeter are performed to demonstrate the capabilities for dose readout possible with the OptCT scanner. The specifics of these irradiations are described further in the results section of this thesis.

The following is a brief overview of each chapter of this study. The second chapter discusses different optical computed tomography methods for scanning three-dimensional dosimeters. Chapter three describes the design, protocol and procedural steps used in the construction and testing of the prototype fan beam OptCT scanner, while chapter four examines scanner characterization results. Chapter five highlights reconstructed OptCT images of three-dimensional polymer gel dosimeters (both reconstructed images of optical attenuation and of dose are presented) and compares the dose derived from OptCT scanning with the dose calculated using the Eclipse treatment planning system. The sixth and final chapter suggests several ways of extending the preliminary dosimetric results through future research.

Chapter 2

Optical Scanning of Three-Dimensional Dosimeters

The purpose of this chapter is to introduce computed tomography theory and outline the principles of OptCT scanning of three-dimensional dosimeters. The chapter is divided into three sections. Section 2.1 underlines the fundamentals of computed tomography theory including the mathematical basis for the filtered backprojection reconstruction algorithm used in OptCT. The three most common OptCT scanning geometries used are introduced in section 2.2. Finally, factors affecting image quality in OptCT are discussed in section 2.3.

2.1 Computed Tomography Theory

The process of image reconstruction is hugely pervasive in science. On the smallest scale, data from electron microscopes are used to reconstruct the molecular structure of bacteriophages, while at the largest scale, data from satellites orbiting the earth are used to reconstruct images of the x-ray composition of distant supernova remains [33]. The most prevalent application of image reconstruction however, occurs in medical diagnostics where the science of computed tomography has revolutionized radiology.

It was Johann Radon in 1917 who first developed the mathematical principles of computed tomography (CT) [34]. He illustrated that complete cross-sectional

images of the interior of an unknown object could be generated if an infinite number of transmission measurements were made through the object at different angles. Because acquiring an infinite number of transmission measurements is not feasible, medical scanners today utilize the filtered backprojection method to approximate cross-sectional images of a sample using a finite number of transmission measurements [35]. The OptCT scanner developed in this research applies the filtered backprojection method to reproduce two-dimensional cross-sections of optical attenuation coefficients within a three-dimensional (3D) dosimeter. The following section outlines the basic principles of data acquisition and image reconstruction used in optical computed tomography.

2.1.1 Data Acquisition: The Sinogram Space

In CT terminology, a ray is a single transmission measurement through an object measured by a single detector. In like manner, a projection or view is a collection of rays passing through an object at a given orientation. In conventional CT acquisition, a series of projections are gathered at different angles around an object [35]. Three main acquisition geometries are employed in CT scanning. In a pencil beam geometry, a single ray passes through the object and is recorded by a single detector. Both the source and detector then translate a short distance and another ray is recorded. This process is repeated until a full projection is gathered across the object (figure 2.1). To acquire a second projection, the source and detector then rotate by a given angle (e.g. one degree) and the translation scanning is repeated. This process is reiterated until a full projection data set is acquired [36]. In a parallel beam geometry, a number of line sources and detectors record many rays simultaneously and all rays are parallel to each other. In a fan beam geometry, a diverging set of rays from a source pass through the object and are acquired by a detector array with either an arc geometry (figure 2.1) or a flat, linear geometry.

The sinogram is a two-dimensional visual representation of the raw data acquired

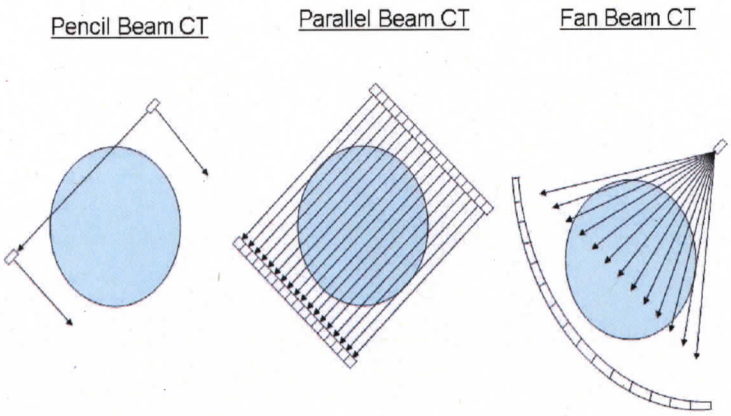

Figure 2.1: Schematic representation of three different CT geometries: pencil beam, parallel beam and diverging, fan beam.

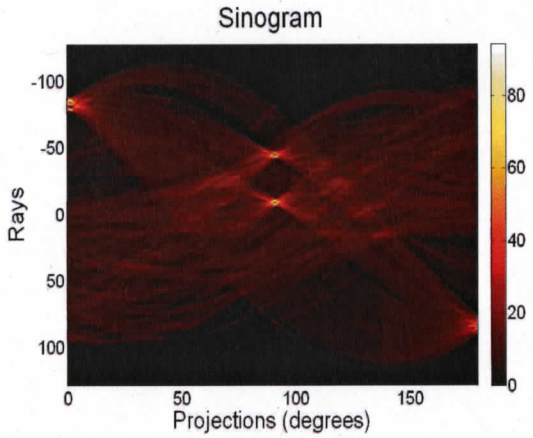

Figure 2.2: Sinogram of an image with dark edges used for computer vision. The strong peaks in intensity in the sinogram correspond to the dark, straight lines in the original image

from one CT slice before reconstruction [37]. The vertical axis of the sinogram corresponds to the different rays in each projection, while the horizontal axis corresponds to different projections as shown in figure 2.2. This information is not directly utilized for clinical evaluation in x-ray CT radiology or in dosimetry in OptCT. Nevertheless, it is useful in assessing the quality of the data. For instance, a sinogram will reveal whether one detector is faulty or whether one projection in the data set is incomplete. Further, frequency domain analysis of the sinogram is useful for revealing systematic trends in CT data acquisition. For example, in OptCT, the sinogram helps to assess any light source drift in intensity or detector gain fluctuation as a function of time.

Once the transmission data is acquired, a series of steps are undertaken to reconstruct an approximation of the object cross-section. A description of such reconstruction methods used in CT is offered later in this section. At this point, however, it is helpful to understand the mathematical basis for CT data acquisition. Transmission data sets acquired in CT are mathematically expressed using the Radon transform. If the cross-section of the object being scanned is represented by a two dimensional function, f(x,y), and each ray scanning through the object is oriented at an angle, θ, to the y-axis, the following line integral represents the projection through the object [37]:

$$P_\theta(t) = \int_{(\theta,t)line} f(x,y)ds \tag{2.1}$$

where

$$\begin{aligned} t &= xcos(\theta) + ysin(\theta) \\ \text{and} \quad s &= -xsin(\theta) + ycos(\theta) \end{aligned} \tag{2.2}$$

Using the Dirac delta function, equation 2.1 can be written as

$$P_\theta(t) = \int_{-\infty}^{\infty}\int_{-\infty}^{\infty} f(x,y)\delta(xcos(\theta) + ysin(\theta) - t)dxdy \tag{2.3}$$

The problem of image reconstruction from the projection data is that of inverting equation 2.3 and recovering f(x,y) from the projection data. In practice, direct inverse transform methods for the inversion of equation 2.3 are not used because of the time required for performing this process on large CT data sets. The following subsections document approximation methods used in CT to obtain f(x,y) from the projection data in a time-efficient manner.

2.1.2 Data Pre-Processing

The raw data acquired in a CT scan is pre-processed before image reconstruction [36]. The number of pre-processing procedures depends on the scanning geometry, the detection system and the scanning transmission source. Nonetheless, one step almost universally undertaken is detector calibration. Commonly, a number of test scans are acquired with no object in place and the average of these acquisitions is used to provide correction information to adjust for the varying electronic gain of each detector in an array [35]. Electronic gain is a measure of the ability of an amplifier to increase the amplitude of a signal (usually expressed as the mean ratio of the signal output to the signal input of the system). This quantity varies from one detector to the next in an array. The calibration scan is also used to compensate for the geometric efficiencies of each detector. In an x-ray CT scan, the x-ray tube rotates around the patient while transmission data is recorded on the output end by a bank of detectors. As the tube rotates, the angle and distance between the source and each detector may change slightly. The calibration scan is used to compensate for this geometric variation.

In straight ray tomography theory, after the digital data is appropriately cali-

brated, Beer's law is applied to compute the logarithm of the signal:

$$ln(\frac{I_o}{I_t}) = \mu(x,y)t \tag{2.4}$$

where I_o is the calibration scan data, I_t is the transmission scan data corresponding to each ray in each view, t is the overall object thickness and $\mu(x,y)$ is the linear attenuation coefficient (in cm^{-1}). In truth, $\mu(x,y)$ in equation 2.4 is a composite representation of the linear sum of all the different attenuating media the radiation passes through before being detected.

In the ideal case of a large number of equally spaced attenuating slabs of thickness *dy*, Beer's law becomes:

$$ln(\frac{I_o}{I_t}) = -\int \mu(x,y)dy \tag{2.5}$$

In conventional tomography, equation 2.5 is expressed in discrete form as:

$$ln(\frac{I_o}{I_t}) = -\sum_{i}^{N} \mu_i(x,y)\Delta y \tag{2.6}$$

2.1.3 Image Reconstruction Methods

After the projection data has been pre-processed, planar data sets are used to reconstruct images. The goal of any two-dimensional reconstruction algorithm is to reconstruct an object function, f(x,y), from measured projection data [37]. In OptCT, the object function represents the two-dimensional distribution of optical attenuation coefficients in a slice through the dosimeter. Although a number of general reconstruction algorithms are available in CT, the two most prevalent techniques are filtered backprojection and iterative reconstruction [38].

Because of its ease of implementation and speed of calculation, filtered backprojection is currently the reconstruction method of choice in both clinical x-ray CT

scanning [35] and OptCT for radiotherapy dosimetry. The Fourier slice theorem forms the basis of the filtered backprojection reconstruction algorithm: for parallel beam projection data, the Fourier transform of the object function is equal to the Fourier transform of the projection data [37]:

$$F(u,\theta) = S_\theta(u) \tag{2.7}$$

where $S_\theta(u)$ is the Fourier transform of the projection data collected at an angle θ. In the following derivation, the Fourier slice theorem is used to indicate how the object function can be derived from projection measurements. To begin, the object function can be expressed using a two dimensional inverse Fourier transform as follows:

$$f(x,y) = \int_{-\infty}^{\infty}\int_{-\infty}^{\infty} F(u,v)e^{j2\pi(ux+vy)}dudv \tag{2.8}$$

Exchanging the rectangular coordinate system, (u,v), for a polar coordinate system, (w,θ):

$$\begin{aligned} u &= wcos(\theta) \\ v &= wsin(\theta) \\ \text{and} \quad dudv &= wdwd\theta \end{aligned} \tag{2.9}$$

and splitting the integral into two by defining θ from 0^o to 180^o as well as from 180^o to 360^o, the two-dimensional Fourier transform is re-defined as:

$$f(x,y) = \int_0^{\pi}\int_0^{\infty} F(w,\theta)e^{j2\pi w(ucos(\theta)+vsin(\theta))}wdwd\theta + \int_0^{\pi}\int_0^{\infty} F(w,\theta+180^o)e^{j2\pi w(ucos(\theta)+vsin(\theta))}wdwd\theta \tag{2.10}$$

If we apply the property,

$$F(w,\theta+180^o) = F(-w,\theta) \tag{2.11}$$

and use the rotation of coordinates: $t = xcos(\theta) + ysin(\theta)$ in conjunction with equation 2.7, the object function, f(x,y), is determined from the Fourier transform of the projection data at angle θ, $S_\theta(w)$:

$$f(x,y) = \int_0^{\pi}[\int_{-\infty}^{\infty} S_\theta(w) \mid w \mid e^{j2\pi wt}dw]d\theta \tag{2.12}$$

Equation 2.12 gives an estimate of f(x,y) from the Fourier transform of the projection data. Specifically, this equation describes the projections being filtered using a filter of frequency response, $\mid w \mid$, and being backprojected across the image space [37]. The factor, $\mid w \mid$, in equation 2.12 has dimensions of spatial frequency. Because the energy contained in the Fourier transform of a CT image can be considered bandlimited (energy above a certain frequency is negligible), it is desirable to implement equation 2.12 in an alternate form to de-emphasize high frequencies which contribute

mostly observation noise to the projection data:

$$Q_\theta(\frac{k}{2W}) \approx (\frac{2W}{N}) \sum_{n=-\frac{N}{2}}^{\frac{N}{2}} S_\theta(m\frac{2W}{N})H(m\frac{2W}{N})e^{j2\pi(\frac{mk}{N})} \tag{2.13}$$

In equation 2.13, $Q_\theta(\frac{k}{2W})$ represents the projection data filtered by a Hamming window, $H(m\frac{2W}{N})$, which removes high frequency components from the image [37]. Further, W is a frequency higher than the highest frequency component in each iteration, $m = \frac{-N}{2}..0..\frac{N}{2} - 1$, $k = \frac{-N}{2}..0...\frac{N}{2}$ of the backprojection reconstruction algorithm. Equation 2.13 gives the final mathematical representation of the object function acquired from the projection data.

Iterative reconstruction is another approach to image reconstruction. However, it is rarely used in conventional CT due to long reconstruction times. It is used in nuclear medicine (positron emission tomography and single photon emission computed tomography) where signal-to-noise ratios are much lower.

2.2 Optical Scanning Methods for Three-Dimensional Dosimeters

Optical computed tomography (OptCT) was originally proposed in 1996 by Gore et al. as a low cost, high spatial resolution alternative to MRI scanning of three-dimensional dosimeters [39]. The low noise achieved using OptCT scanning is a result of the sensitivity and precision of the photodiode/CCD-based technology employed to measure transmitted laser light [40]. Although physically similar to x-ray CT, OptCT system design can be significantly more flexible and easier to adjust quickly because a variety of different light sources can be used in conjunction with optical elements such as mirrors, lenses, polarizers and miniaturized digital detectors [29]. Current OptCT scanning methods rely on the attenuation of light in the dosimeter volume through scatter or absorption of light along ray lines. However, other physical properties

such as fluorescence and polarization of light can also be exploited in reconstructing cross-sectional images of a three-dimensional dosimeter [41].

When optical scanners are used in conjunction with three-dimensional dosimeters, the dose-response mechanism relies on either the production of light-scattering micro-particles (polymer gels) or light-absorbing molecules (polyurethane plastics). Scattering or absorption of monochromatic laser light produces an attenuation of transmitted light intensity that is correlated to the dose [29]. Cross-sectional images of dose distributions are reconstructed using filtered backprojection. The principal obstacles to accurate imaging in OptCT are refraction and scattering of light at the different interfaces of the dosimeter and scanner. Unlike conventional x-ray CT imaging where rays approximately follow straight line paths through heterogeneous media, optical light changes direction when it encounters regions of varying refractive index.

Three different scanner geometries have been introduced for OptCT scanning of 3D dosimeters. These include first, second and third generation CT regimes. An ideal geometry for scanning radiotherapy dosimeters has not yet been identified. A choice among the three geometries depends on the type of dosimeter being used (gel or polyurethane plastic), the requirements set on spatial resolution, dose resolution and precision of the dosimetry process, maximum allowable cost of the scanner, size of the dosimeter being imaged, and time allowed for imaging.

2.2.1 Pencil Beam Optical Computed Tomography

The first OptCT scanning device used a pencil beam geometry and was developed in 1996 by Gore et al. [39] in the Department of Diagnostic Radiology at Yale University. Since then, a number of different first generation (pencil beam) scanners have been developed. A pencil beam OptCT system uses a single laser beam and photodiode detector to scan in raster fashion across the face of a dosimeter and collect projection data. Commonly, the dosimeter sample is immersed in an aquarium filled with a fluid whose refractive index is similar to that of the dosimeter. Line scans are taken

with the laser stepping in small (e.g. 1 mm) increments across the dosimeter flask (figure 2.3).

The laser is usually translated an additional 1.5 cm on either side of the dosimeter sample, allowing padding for the projection data. Image padding introduces new pixels around the edges of an image. These pixels act as an additional boundary area around the existing image and are often added in OptCT to assure the projection data has the necessary dimensions to perform a filtered backprojection reconstruction with no aliasing. Padding may also be used to assure the size of the image corresponds to the size of a masking filter.

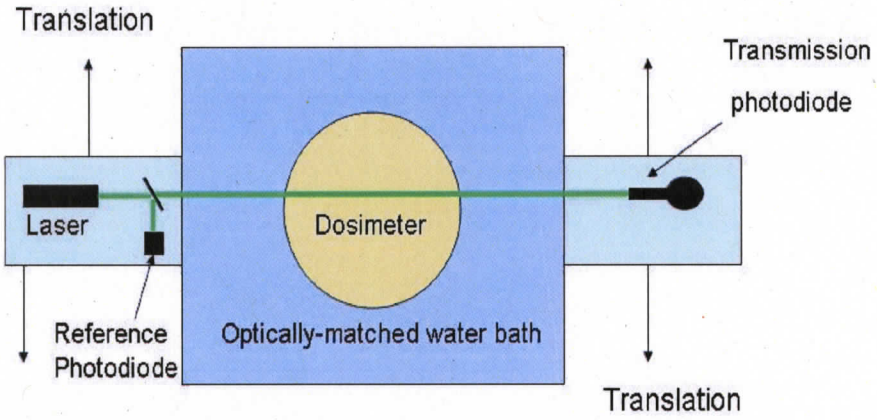

Figure 2.3: Schematic of a pencil beam, translate/rotate optical CT scanner. The laser beam and detector are stepped in synchrony across the face of the dosimeter and matching tank until a full projection is recorded. To acquire the next projection, the dosimeter is then rotated by a small angular increment using a stepper motor .

After each complete translation across the face of the dosimeter, the sample is rotated by a small angular increment (e.g. 1^o) using a sealed rotation platform centered on the bottom of the aquarium. In this way, another projection is acquired. The rotation platform ensures the axis of the dosimeter is coaxial with the axis of rotation of the motor. The translate/rotate process is repeated until the vessel has been rotated through a full 180^o to collect the complete projection data set. Before scanning through the dosimeter, the pencil laser beam is divided by a beam splitter.

One beam from the beam splitter is detected by a reference photodiode to provide a measurement of the input light intensity while the second beam is normally incident upon the flat wall of the aquarium.

Although a number of prototype, first generation OptCT scanners have emerged, the most developed model and first commercially available system, OCTOPUS, advanced by MGS research [30] is an extension of the design shown in figure 2.3. Scatter rejection and pixel-value accuracy are achieved with both laser auto-collimation and the use of a single photodiode and 16-bit A/D resolution for measuring the intensity of the transmitted light. The scanner allows a minimum pixel size of 0.3 mm and a typical pixel size of 2 mm with a dose accuracy of 4% and a dose precision of 2% for gels irradiated with uniform fields to doses of less than 2 Gy. The principal disadvantage of first generation scanners however, is their long data acquisition times. For large matrix sizes, data acquisition can take several hours.

2.2.2 Parallel Beam Optical Computed Tomography

The first parallel beam OptCT scanner was introduced by Simon Doran et al. in 2001 at the University of Surrey [42]. A mercury lamp was used as a light source and rays from the lamp were passed through a cylindrical lens, pinhole and filter to generate a pseudo point-source. The diverging rays from the point source were re-directed through a large telecentric lens to generate parallel rays which reflected 90^o off a mirror and impinged normally on the walls of a scanning tank containing the dosimeter sample [42]. The scanning tank, consisting of a hollow perspex cube with sides of 30 cm length was filled with 3 L of water (refractive index of 1.33) mixed with 1 L of glycerol (refractive index of 1.4729) to match the refractive index of the fluid to that of the dosimeter ($\sim$ refractive index of 1.35). To acquire different projections, the dosimeter was rotated on a motorized turntable. On the output end of the scanner, the parallel rays passed through a diffuser screen, reflected 90^o off a mirror and were detected by a two-dimensional CCD detector.

A second version of this scanner was developed in 2007 by Doran and Krstajic, using an LED light source located behind a circular pinhole of diameter 1 mm [43]. The pinhole is placed on the focal point of a large telecentric, collimating lens, creating parallel beams which pass through the sample and are attenuated by the gel dosimeter as illustrated in figure 2.4. The parallel beams are then focused by another telecentric lens on the other side of the aquarium onto a CCD lens which concentrates light onto a 2/3 inch CCD chip inside the camera [43]. In order to reduce spherical aberration, the convex side of the telecentric lenses face the parallel beam.

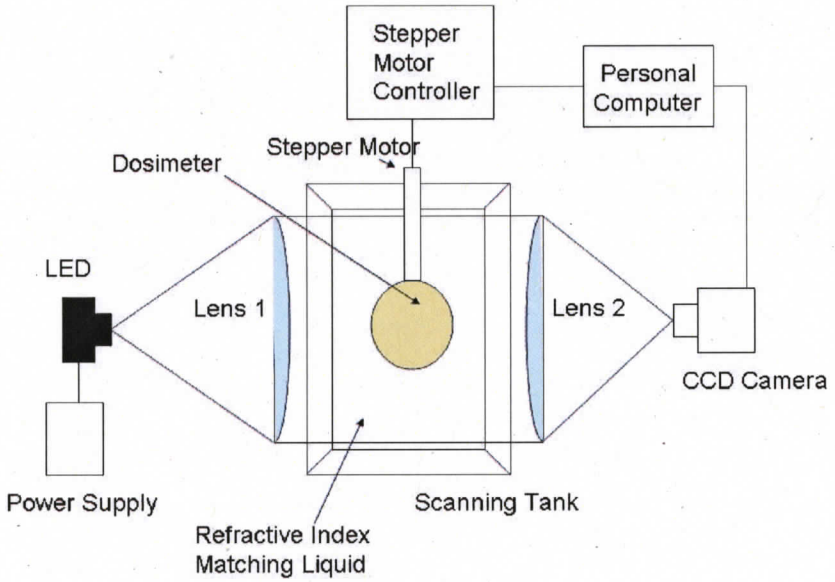

Figure 2.4: Schematic diagram showing a parallel beam OptCT scanner.

A key advantage of parallel-beam, CCD-based OptCT scanning is its speed. Using continual rotation of the dosimeter sample when acquiring projection data, it is possible to obtain three-dimensional data sets within a minute (more than two orders of magnitude faster than the pencil beam scanning). The only limitation to its speed is imposed by the CCD readout and data transfer time to the host computer [43]. The main drawback with parallel beam scanners using telecentric lenses is their overly noisy projections. Specifically, if a gel dosimeter is not mixed thoroughly dur-

ing chemical preparation, refractive index inhomogeneities within the dosimeter may lead to individual rays refracting away from straight ray paths. Since the filtered backprojection reconstruction algorithm currently used with these scanners calculates an image under the assumption that all rays travel along straight paths, light ray refraction may result in artefacts in the reconstructed image. Increasing the light source aperture by shining the LED into a small diffuser (e.g. 8 mm diameter) reduces these effects but introduces ring artefacts in OptCT images [43]. Parallel beam OptCT scanners are also prone to scatter artefacts and inhomogeneities in the matching fluid. As well, they are several hundred dollars more costly than other scanners because of their large telecentric lenses.

2.2.3 Converging Beam Optical Computed Tomography

OptCT imaging using a converging beam from a diffuse light source was first introduced by Wolodzko et al. at Rutgers University in 1999 [44]. The imaging light source used in this work was a fluorescent illumination lamp with a colour temperature of 5000 K. This light source emits most of its energy over a range of wavelengths extending from about 400 to 700 nm [44]. The diffuse light is passed through a translucent diffuser panel to provide uniformity, while adjustable cardboard shutters positioned between the diffuser panels and the scanning water tank collimate the light source to the width of the dosimeter array (figure 2.5). This collimation prevents angle-dependent, tangential reflection of light from the surfaces of the dosimeter. A direct-to-digital CCD video camera interfaced to a desktop computer collects the signal on the output side of the scanner tank. In his original work, Wolodzko scanned six irradiated glass vials arranged in a close, hexagonal array. The array itself was positioned on a rotating turntable in the water tank to collect projection data sets.

In 2006, a diverging, cone beam OpCT Scanner named Vista was advanced by Modus Medical Systems. This was a more compact extension of Wolodzko's original design. Specifically, the scanner used 630 or 590 nm LEDs to illuminate a dosimeter

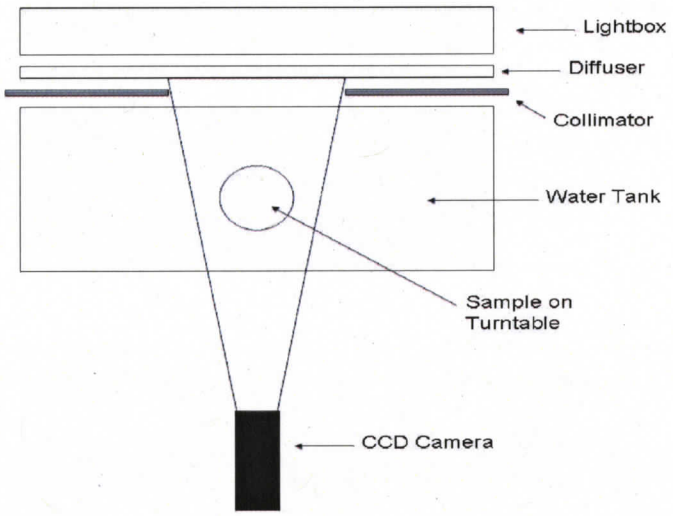

Figure 2.5: The components and layout of a converging beam OptCT imaging system using a diffuse light source.

sample and collect projection data in a 1024 x 768 matrix using an 8-bit monochrome CCD camera. The acquisition and reconstruction time for 340 frames using a 360^o Feldkamp backprojection for a 10 cm cube with 1 mm voxels was 15 minutes [45]. The scanner has the ability to scan cylindrical three-dimension dosimeters 15 cm in diameter and 12 cm in height with 0.56 mm isotropic resolution for uniformly irradiated gels. Because the scanner is still in the developmental phase, irradiation restrictions using low dose conditions to minimize scatter must be maintained for quality dosimetry. When higher radiation doses are delivered to the gels, scatter of the broad beam light source is more significant and leads to lower signal-to-noise ratios with larger inaccuracies in the reconstructed images [29].

In general, broad beam geometries achieve faster scanning times than pencil beam scanners, with a minimal increase in computer processing requirements for reconstruction. Because scatter and refraction artefacts can be more severe however, necessary procedures must be undertaken to account for these physical effects.

2.3 Factors Affecting Optical CT Image Quality

High resolution, three-dimensional dosimetry using OptCT is sufficiently sensitive to allow doses as low as 5 cGy and as high as 20 Gy to be measured, depending on gel sensitivity and OptCT scanner dynamic range [30]. Further, OptCT systems can also allow sub-millimetre spatial resolution if images are free from artefacts. However, in order for OptCT in conjunction with three-dimensional dosimeters to become clinically viable, a number of issues must be confronted. They include a better understanding of reflection, refraction and scatter in three-dimensional dosimeters as well as the ability to manufacture high quality dosimeters with uniform response and optical clarity [30].

The sections which follow underscore some of the physical challenges involved in optical imaging of three-dimensional dosimeters. They also review methods that have been used to improve OptCT imaging spatial and contrast resolution.

2.3.1 Artefacts Due to Scatter

The mechanism of optical attenuation in three-dimensional polymer gel dosimeters involves the production of light scattering microparticles 400-700 nm in diameter as a result of radiation induced copolymerization of monomer species embedded in the gel matrix [29]. Consequently, most of the visible photons arriving at the detector elements in OptCT do not follow straight paths dictated by geometrical ray tracing. Nonetheless, simulation and experimental OptCT imaging indicate that a large number of the visible photons are only refracted slightly about straight ray trajectories during their course through the dosimeter [42]. The degree to which this approximation is accurate depends on both the magnitude of the refractive index changes in the dosimeter and the distribution and density of scattering microparticles embedded in the gel. The microparticle distribution and density is directly related to the dose given to the gel. For uniformly irradiated polymer gels, when scattered photons

contribute to the intensity profile in a measured projection data set, the attenuation of a slice is typically underestimated at the centre of an OptCT image [45]. However, when complex microparticle distributions exist in a gel the effect of scatter is more difficult to predict. The following subsection examines the effects of visible light scattering on OptCT imaging.

The scattering of light may be conceptualized as the redirection of an electromagnetic wave or incident light ray when it encounters an inhomogeneity [46]. In the case of OptCT imaging of polymer gels, these inhomogeneities take the form of microparticles. As an electromagnetic wave interacts with a discrete particle, the electron orbits within the constituent molecules of the particle are perturbed periodically with the same frequency as the electric field of the incident wave [47]. This perturbation of the electron orbits produces an induced dipole moment within the molecule that acts as a source of electromagnetic radiation which is seen as scattered light (figure 2.6). A large fraction of the light scattered by the particle is emitted at the same frequency as the incident light, a process referred to as elastic scattering.

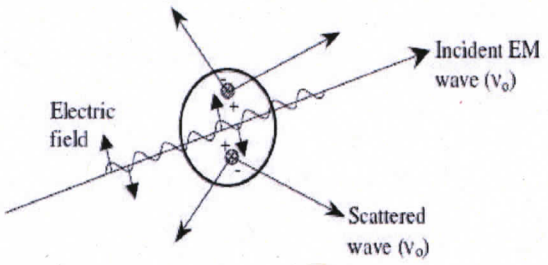

Figure 2.6: Scattered light is produced when electromagnetic radiation perturbs the electron cloud of a molecule, inducing an oscillating dipole moment in an atom.

Visible light scattering theory may be categorized into two theoretical frameworks: the theory of Rayleigh scattering and the theory of Mie scattering. Rayleigh scattering applies to small, dielectric (non-absorbing) spherical particles. It pertains to elastic collisions in which the diameter, 'a', of the spherical scattering particle is significantly less than the wavelength, λ, of the incoming light according to $\alpha \ll 1$

where

$$\alpha = \frac{2\pi a}{\lambda} \tag{2.14}$$

Mie scattering is a general spherical solution to Maxwell's equations for absorbing and non-absorbing particles without a bound on particle size. It converges to the limit of geometrical optics for large particles. In OptCT, Mie scattering may be used in conjunction with Monte Carlo simulation to understand the scattering of visible light in the dosimeter volume [30]. The cross-section for Mie scattering is:

$$\sigma_{scat} = (10\pi)(\frac{1}{3})(a^2)(ka)^3 \tag{2.15}$$

where 'a' is the mean diameter of microparticle scatterers in the gel and k is the wave number of incident radiation:

$$k = \frac{2\pi}{\lambda} \tag{2.16}$$

σ_{scat} may be used to simulate the mean free path between scattering events, redirection of light particles in the dosimeter medium and the contribution of scattered light to the projection data.

Monte Carlo simulations performed by Oldham in 2004 [30] to mimic a 638 nm pencil beam scanning through a simulated gel irradiated with a 5 $\times$ 5 cm^2, 6 MV photon field (projection data collected using a simulated 2 $\times$ 2 cm^2 square detector) indicated that, by only assuming a square distribution of scattering microparticles of radius 475 nm, density 40 000 cm^{-3} and refractive index of 1.54, profiles which compare to experimental profiles could be generated. Specifically, a profile from the reconstructed image generated from the Monte Carlo process displayed a depression in the middle of the profile due to scattered photons.

Also in 2004, Oldham et al. [30] examined the effects of scatter experimentally

using the first generation, OCTOPUS, OptCT scanner [40]. Polyacrylamide-based gels irradiated uniformly to different doses were imaged multiple times under varying levels of scatter rejection achieved by varying the diameter of a scatter-rejecting collimator positioned at the face of the single photodiode detector. Increased dose in gels caused a depression of reconstructed attenuation values in the middle of the field by a fixed proportion [30]. Presumably, this was due to photons being scattered away from the central detectors and flooding the outer elements. With the introduction of a collimator, reconstructed attenuation coefficients were found to be 13% greater when the collimator was closed to a 3 mm diameter than when fully open to a 20 mm diameter.

2.3.2 Artefacts Due to Reflection and Refraction

Two of the most significant sources of artefacts in OptCT images arise from reflection and refraction of light rays at the walls of the dosimeter flask, as well as within the dosimeter volume [42]. Gore [39] first proposed limiting the range of projection data to exclude regions close to the edges of the flask in order to restrict these edge effects. Although useful for radiation treatments which do not impinge within 90% of the diameter of the flask, this technique discounts dosimetry of many clinically relevant protocols where the beam is delivered axially through the side of the dosimeter container. In order to minimize the effects of refraction at the wall of the dosimeter flask, all modern OptCT geometries immerse the dosimeter in a matching fluid whose refractive index approximates that of the dosimeter. If a matching fluid is not used, the dosimeter acts like a converging cylindrical lens and light rays traveling close to the edge of the cylinder are severely refracted. Most notably, in first generation OptCT scanners, such refraction results in loss of transmission data at the dosimeter edge, making interpolation methods necessary to recover the missing data [41]. The path of light rays through the scanning tank and dosimeter volume is described by Snell's law:

$$n_i sin(\theta_i) = n_t sin(\theta_t) \tag{2.17}$$

where n_i and θ_i are the refractive index of the material and angle relative to a normal vector to the surface on the incident side of the boundary and n_t and θ_t are the corresponding values on the transmission side. If the paths of light rays through the aquarium and dosimeter can be accurately simulated using ray tracing (figure 2.7), the projection data can be scaled appropriately to account for some detectors recording higher intensities than others because of refraction.

Losses in laser beam intensity due to reflections of the beam at the aquarium walls and the four surfaces of the dosimeter flask can also be corrected numerically [41]. In particular, at each interface of the dosimeter cylinder, a fraction of the incident light is reflected and the remaining light is transmitted according to the Fresnel equations [42]. The Fresnel equations are different for polarization of incident light parallel and perpendicular to the surface. In the case of OptCT, the intensity transmission coefficients T_E and T_H for light polarized with the E- and H-fields parallel to the surface are:

$$T_E = (\frac{n_t}{n_i})(\frac{2n_i cos(\theta_i)}{n_i cos(\theta_t) + n_t cos(\theta_i)})^2 \tag{2.18}$$

and

$$T_H = (\frac{n_t}{n_i})(\frac{2n_i cos(\theta_i)}{n_i cos(\theta_i) + n_t cos(\theta_t)})^2 \tag{2.19}$$

If necessary, these coefficients can be used to scale the recorded projection data to account for reflection of the laser beam at the aquarium walls and dosimeter flask interfaces.

Physical refraction effects can also lead to geometrical distortion. In particular, light ray refraction can cause compression artefacts where object dimensions are

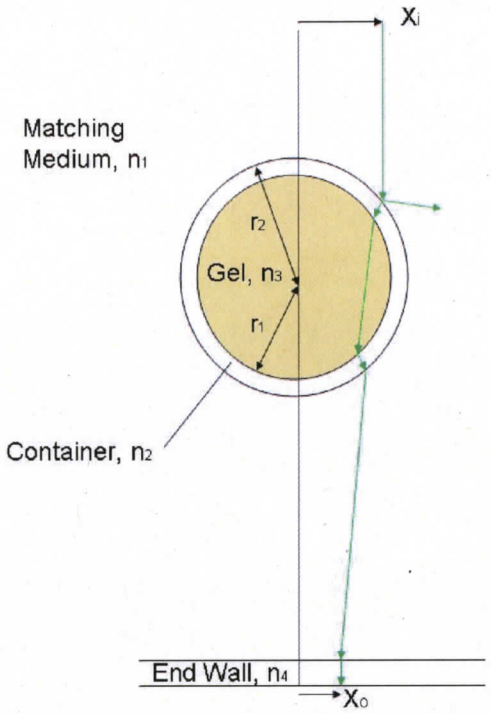

Figure 2.7: Geometry of rays passing through gel container and scanner tank.

inaccurately represented in a reconstructed OptCT image. In this regard, Oldham *et al.* have performed a series of phantom tests to quantify the degree of geometrical distortion in optical CT images [30]. Using the OCTOPUS first generation scanner, the tests examined the position, dimension and orientation of optically opaque, steel needles embedded in a gelatin phantom placed in a clear cylinder 11 cm in diameter [40]. True needle positions were determined by x-ray CT scanning along the central slice of the phantom. An equivalent OptCT image of the central slice was obtained and superimposed on the x-ray CT images showing negligible distortion (<0.25 mm) when the refractive index of the matching solution matched that of the gel. When the refractive index of the bath was not appropriately matched, a radial compression distortion was observed, the magnitude of which was linear with increasing refractive index mismatch [30].

In addition to the above test, other groups have used commercially available test

targets to assess geometrical distortion. Using their parallel beam scanner and a distortion test target from Edmund optics, Doran et al. [43] found the minimum distortion measurable for a 400 × 400 pixel projection was 0.18%. Although these methods illustrate that distortion can be minimized for idealized field geometries (in the case of Oldham) and simple test targets (in the case of Doran), little work has been done to examine the effects of light ray refraction effects for dosimeters irradiated with complex field arrangements typical of modern radiotherapy.

Noise in OptCT images can also contribute distortion of an image matrix. For instance, optical-CT projections may be noisy if a gel dosimeter is not mixed properly. In this case, some projections may overemphasize the refractive index inhomogeneities within a dosimeter [48]. Such homogeneities within a dosimeter can partially be accounted for by either averaging projections or choosing low-noise projections. For the most part however, refractive index inhomogeneities within the dosimeter are easiest to remove at the gel manufacture stage [48].

2.3.3 CT Scanning Parameters and System Design

Generally, the scanning parameters and system design details which affect x-ray CT are also applicable to OptCT imaging. However, because visible rather than x-ray wavelength electromagnetic radiation is used in OptCT, the specific way each of these factors affect CT spatial resolution and contrast may differ for OptCT.

A wide range of reconstruction parameters and system design characteristics can be manipulated in OptCT to affect image quality. Acquisition and reconstruction parameters which may be altered include optical laser step size in first generation scanners, number of projections, projection angular increment, number of data readings taken at each projection angle, detector gating time, and a variety of reconstruction algorithm related parameters. Similarly, system design characteristics which may be changed to improve imaging include light source, detector collimation, dosimeter vessel wall size, detector pitch, detector aperture width, object magnification and

scanner field of view. A brief discussion of some of the most relevant of these parameters in OptCT follows. A more thorough discussion is offered in the results section of this study.

Detector pitch is the center-to-center spacing of detectors in an array. It determines the spacing of accepted rays in the projection data. The number of rays sampled has a profound impact on the radial component of spatial resolution. If it is reduced by increasing the detector pitch, low-resolution, blurred images will result [35]. The detector aperture width constitutes the width of one active element in a detector array or one pixel on a CCD camera. The use of a smaller detector aperture allows higher spatial resolution at all frequencies. The number of projections or views acquired in an image influences the ability of the CT system to convey a high resolution image without the presence of artefacts [49]. Using too few projections results in radiating line artefacts in an image. These are more apparent towards the edges of the image [35]. Lastly, it is important to determine an appropriate number of projection averages and detector integration time at each projection angle.

Several OptCT research groups have examined the effect of optimum scanning parameters on image quality. Although image quality tests were not strictly performed in any of these dosimetry-based studies, the goals were to achieve high spatial and dose resolution with minimal effects due to artefacts. In 1998, Jordan et al. specified a set of ideal parameters for a pencil beam scanner with a ferrous xylenol orange gel [41]. They included a pencil beam translational increment of 1.0 mm, projection range of rotation of 180^o with a rotational increment of 2.25^o and a complete slice scan of 8000 projection data points. Oldham et al. [50] also have published results detailing nominal operating characteristics of their first generation OptCT scanner. They used a laser step size of 1 mm and 120 projections at 1.5^o intervals. As well, each projection was averaged over 50 acquisitions [50]. Finally, Doran identified the optimal acquisition and reconstruction parameters for his parallel beam scanner as:

1000 projections and a 128 $\times$ 128 image matrix size across a 64 mm field-of-view (FOV) [43]. In his image reconstruction algorithm, he employed a standard filtered back-projection algorithm with a hamming filter.

Chapter 3

Experimental Design, Protocol and Procedure

The overall focus of this chapter is to detail the design of the prototype fan beam OptCT scanner, the techniques used in its characterization and its initial gel dosimetry protocols.

The chapter is partitioned into five sections. Section 3.1 details the planning, design and construction of the fan beam scanner itself. The wet chemistry and handling procedures used for preparation of the gel phantoms are then described in section 3.2. In section 3.3, the treatment planning steps and irradiation methods used for dosimetry verification are highlighted. The methods used in scanning the gel phantoms and reconstructing optical density images are identified in section 3.4. Lastly, the data analysis techniques used to process the reconstructed images are described in section 3.5.

3.1 Optical Scanner Design and Instrumentation

A photograph and schematic of the OptCT scanner are shown in figure 3.1. The scanner has been built on a Newport optical bench 60.96 cm in width, 121.92 cm in length.

The OptCT scanner is the optical equivalent of a third generation x-ray CT

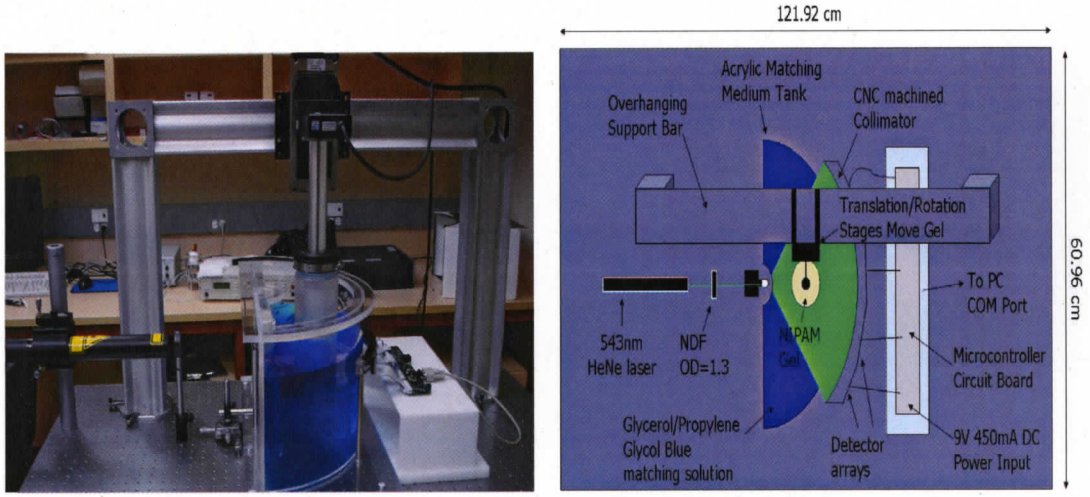

(a) (b)

Figure 3.1: OptCT scanner (a) digital picture and (b) schematic.

scanner. To acquire a two-dimensional transmission slice, the dosimeter is suspended in a refractive index matching fluid, composed of 3 L of de-ionized water and 1 L of concentrated glycerol (a blue polypropylene glycol dye may be added to the solution as shown in figure 3.1 to homogenize the attenuation of the fan beam through the matching solution), and rotated in small angular increments by a Newport (Irvine, California), URS series rotational stage. The transmitted portion of the fan beam is detected on the output side of the scanner by five concentrically arranged Hamamatsu (Hamamatsu City, Japan), S8865 Series, linear, photodiode detector arrays each consisting of 64 detector elements (320 detectors total). At each projection angle, the same detector records the same ray traveling through the dosimeter.

3.1.1 Fan Beam Light Source

The light source employed for illumination with the scanner is a class IIIa, 543 nm (green) Helium-Neon, laser from Research Electro-Optics (Boulder, Colorado). The laser, shown in figure 3.1(a) produces a collimated, 0.83 mm diameter, circular beam of laser light with a divergence of 0.84 millirads. The power output of the laser is 2.0

mW and it is mounted 17.5 cm above the surface of the optical table on a ULM series cylindrical mount from Newport. The laser mount allows both horizontal and vertical alignment of the laser beam and, when tightly adjusted, prevents laser movement and concomitant beam wobble. It is attached with 340-RC Newport rod clamps to a post which inserts directly into the optical bench.

In scanning all but the most dense polymer gels, the signal from the photodiode array detectors was found to saturate without the use of an optical filter. Hence, when the laser is turned on, a pencil beam passes through a spectrally flat, reflective, neutral density filter (Edmund Optics, Barrington, New Jersey) held in place by a Newport lens mount positioned 17.5 cm above the surface of the optical table in direct alignment with the laser beam port. For calibration scanning and precision tests, the net optical density of the neutral density filter was 1.8-2.1. For transmission scanning, the optical density of the neutral density filter was 1.5-1.8. The specific optical density depended on the density of the polymer gel being scanned. Different optical densities of the neutral density filter were achieved by using stacks of single filters to create intermediate density values.

After passing through the neutral density filter, the pencil beam is incident upon a line generating lens. The lens, composed of SF6 glass with an index of refraction of 1.805, creates a fan of laser light subtending a 60^o angle. To prevent light rays from refracting, the position of the lens relative to the front aperture of the tank is critical. Specifically, the lens must be positioned half-way between the two front edges of the semi-circular front aperture of the matching medium tank. To ensure the centre of the lens is fixed accurately relative to the front of the tank, the lens is mounted on two micrometer-based, translational stages allowing fine left/right and back/forth positioning.

3.1.2 Tank Design and Motion Stages

During a scan, the polymer gel dosimeter is immersed in a matching medium solution composed of 3 L of deionized water mixed with 1 L of concentrated glycerol. Such a solution has a refractive index of 1.35 which is similar to that of the dosimeter and reduces the effects of light ray refraction at the four walls (both internal and external walls) of the gel cylinder. The matching solution is contained in a matching medium tank (figure 3.2) having semi-circular front and back apertures. The apertures are designed so light rays from the fan beam source strike the tank interfaces at right angles, thus eliminating refraction effects. The tank has flat front side walls composed of a clear, acrylic plastic, 9.5 mm in thickness. The front, curved aperture is composed of polycarbonate plastic with an inside radius of 31.75 mm and an outside radius of 34.90 mm (figure 3.2). A segment of the front window 3 mm in height and 34.90 mm in radius where the fan beam passes through was removed and replaced with a 1 mm thick mylar sheet to eliminate the effects of groove-related optical inhomogeneities in the polycarbonate plastic. The back curved aperture (inner radius = 228 mm, outer radius = 231 mm) is composed of 3 mm thick, acrylic, clear plastic with no groove-related optical inhomogeneities.

A metal cross-bar is positioned over the top of the scanning tank and supports a rotational stage which suspends and rotates the dosimeter. When a scan is being performed, the dosimeter is tightly held by a circular rubber joint attached to the rotational stage by a 19 cm long bar suspending the dosimeter in the matching fluid (figure 3.1(a)). A projection scan is acquired when the gel dosimeter is incrementally rotated in either 1^o or 0.5^o increments by the rotational stage. This procedure is repeated until projection data is acquired over a full 360^o. When multiple slices through the gel are being acquired, a translational stage moves the rotational stage and, concomitantly, the gel up or down in the desired direction (figure 3.1(a)). Both the rotational and translational stages are controlled remotely by a PC using software

written in-house in Matlab (The Mathworks, Natick, MA), firmware and C++ code. The rotational stage has a resolution of 0.0005^o, a maximum velocity of 80 $\frac{deg.}{s}$ and a maximum acceleration of 320 $\frac{deg.}{s^2}$, while the translational stage has a resolution of 1 μm, a maximum velocity of 2.5 $\frac{mm}{s}$ and a maximum acceleration of 10 $\frac{mm}{s^2}$. For full volumetric scanning, dosimeters 10 cm in height can be scanned in 100 minutes, using one signal acquisition per angle over a total of 360 projection angles. Such a volumetric scan can be recorded with a slice thickness of 0.8 mm (detector element height) and a slice spacing of 0.2 mm. Further, an image of a single slice through a dosimeter can be reconstructed in one minute, using one signal acquisition per angle over a total of 360 projection angles. Dosimeters as large as 19 cm in cross-sectional diameter can be accommodated in the matching tank for scanning.

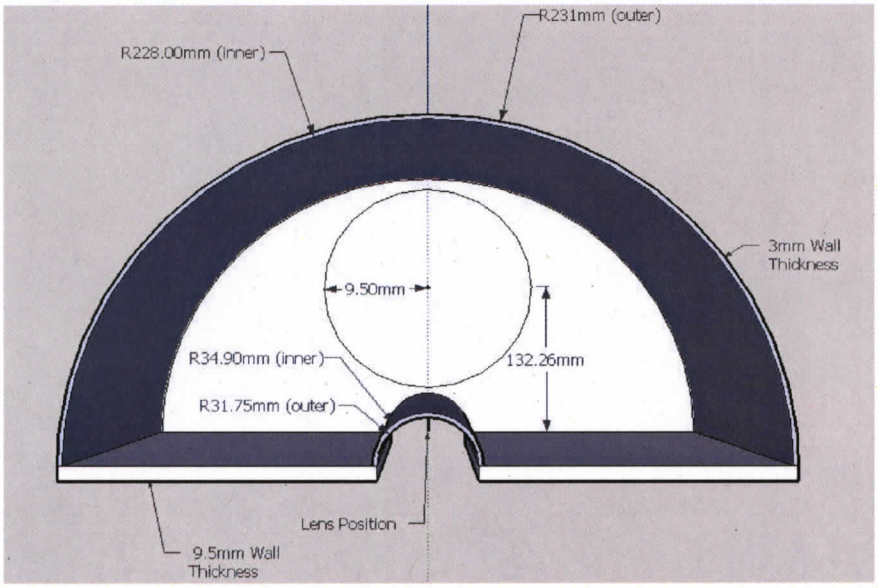

Figure 3.2: Three-dimensional CAD diagram of matching tank.

3.1.3 Photodiode Detectors and Circuit Board

The fan beam of laser light scanned through the dosimeter in the OptCT system is detected using a combination of five concentrically arranged Hamamatsu, S8865 series silicon photodiode arrays (figure 3.3(a)). The flat arrays consist of 64 detector

elements with 0.7 mm width, 0.8 mm height and 0.1 mm element spacing. The total active area length of each detector array is 51.2 mm. The detectors are fixed with screws on the back of a custom computer numerical control (CNC) machined collimator, as shown in figure 3.3(b). Using ribbon cables, a microcontroller-based circuit board connects to each of the detectors (figure 3.3(b)). This circuit board interfaces with a PC.

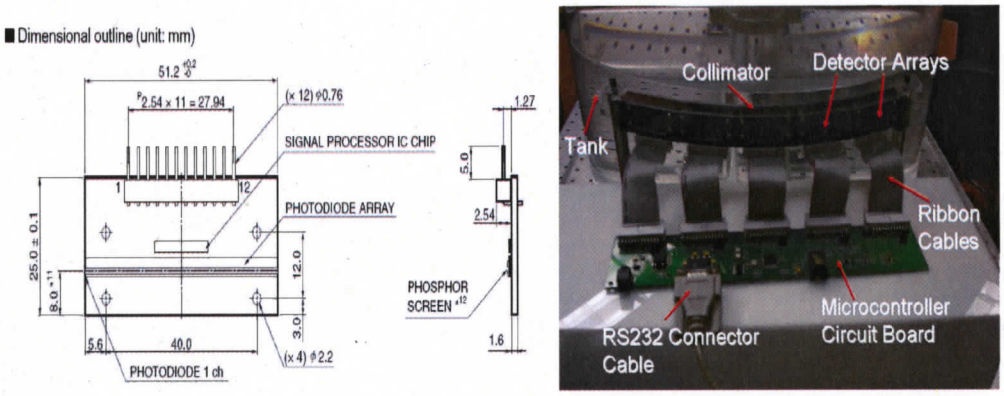

(a) (b)

Figure 3.3: Hamamatsu S8865 series silicon photodiode array (a) schematic and (b) digital picture showing five ribbon cables attaching the photodiode arrays to the OptCT microcontroller circuit board. Each of the five detector arrays is mounted onto the back of the CNC custom-machined collimator.

The microcontroller circuit board, developed in-house for the OptCT scanner, allows for a variable photodiode detector integration time between 250 ns and 25 μs. The microcontroller has also been engineered to provide an extended dynamic range of input pixel values by using a 14-bit analogue-to-digital (A/D) converter with the circuit board.

3.1.4 Light Collimation

Projection images in area detector-based scanners are susceptible to detection of contaminant scattered light known to cause cupping depressions or cross-shaped artefacts in the line profile through an irradiated polymer gel [30]. The contribution of scat-

tered light in projection images is greatly reduced however, by introducing customized telecentric collimation [51].

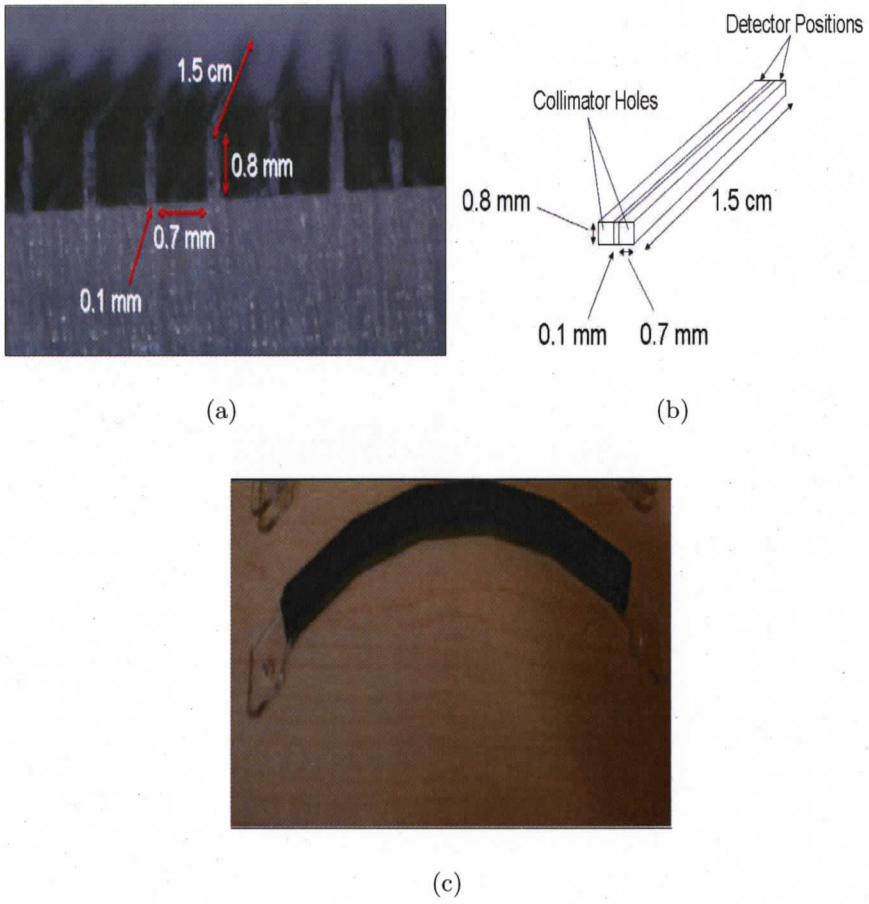

Figure 3.4: Collimator diagrams showing (a) front view of a section of the collimator (only bottom half of collimator is shown), (b) schematic of two collimator holes, (c) top view of the complete collimator assembly.

Accordingly, a collimator was generated using a CNC milling machine. The holes of the collimator were rectangular and had widths of 0.7 mm, heights of 0.8 mm and 0.1 mm separations as illustrated in figure 3.4(a). The collimator hole and separation dimensions mimic the dimensions of the individual detector elements. Based on imaging tests at the outset of the scanner's construction, a uniform thickness of 1.5 cm was determined for the collimator. Each collimator hole drilled to the left or right of the central beam axis was oriented at an angle of (n + 0.179) degrees

where n is the number of detector elements/collimator holes to the left or right of the central detector/collimator hole. The collimator material was black acrylic to enhance absorption of scattered light striking the collimator septa (figure 3.4(c)). The collimation served not only to reduce scattered light, but also to position the photodiode detector arrays in the correct, concentric geometric orientation.

3.2 Polymer Gel Manufacture

Gelatin-based phantoms for both characterization and dosimetry verification tests of the OptCT system were prepared on a chemistry bench (figure. 3.5(a)) and mixed under a fume hood (figure 3.5(b)) at VIC.

(a) (b)

Figure 3.5: Gel chemical preparation (a) lab bench and (b) fume hood and hot plate for chemical manufacture.

3.2.1 Characterization Phantoms

To characterize the fan beam OptCT system, a series of simple test phantoms were prepared. Using the test phantoms, the influence of the refractive index matching solution and tertiary collimation were evaluated. Additionally, the optimum acquisition and reconstruction parameters were established.

To examine spatial resolution of the system and identify the optimum refractive index of the matching solution, a needle phantom was prepared. The needle phantom

consisted of a gelatin gel composed of 5% (by weight), 300 bloom porcine skin gelatin (Sigma Aldrich, Chemical Co., St. Louis, MO.) and 95% deionized water from an ion exchange purifier. To prepare the phantom, 50 g of gelatin powder were weighed on an electronic balance in a 125 mL Erlenmeyer flask. The powder was then mixed for one hour with 950 mL of deionized water in a 2 L cylindrical flask using a magnetic stirring rod on an electronically conrolled hot plate (Fisher, Ottawa, Ontario) at 35°C. After mixing, the solution was poured into a transparent, one litre, Barex, cylindrical flask and refrigerated for three hours. Once the gel mixture had solidified, the flask was removed from the fridge and four, 0.92 mm steel needles were inserted, as shown in the OptCT image of figure 3.6.

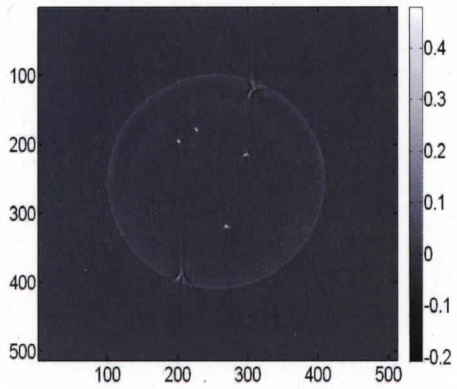

Figure 3.6: OptCT image of needle phantom.

Besides the needle phantom described above, a highly irradiated N,N-isopropyl acrylamide-based polymer gel was utilized to examine the contribution of scattered light to the intensity of a single photodiode positioned along the central axis of the scanner.

3.2.2 Dosimetry Phantoms

Two gel containers were used for dosimetry verification: a one litre, cylindrical, transparent, Barex jar (figure 3.7(b)) and a 500 mL, coffee-cup shaped Barex jar

(figure 3.7(a)). The polymer gels prepared in these jars to test dosimetric accuracy of the scanner were composed of: (a) porcine skin gelatin (5% by weight), approximately 300 Bloom (a gel strength indicator), (b) electrophoresis-grade N-isopropyl acrylamide monomer (NIPAM, 3% by weight), (c) electrophoresis-grade N, N'-methylene-bisaclylamide cross-linker (3% by weight), water obtained from an ion-exchange purifier (89% by weight) and 4.625 mM tetrakis hydroxymethyl phosphonium chloride (THPC)(Sigma Aldrich, Chemical Co., St. Louis, MO.).

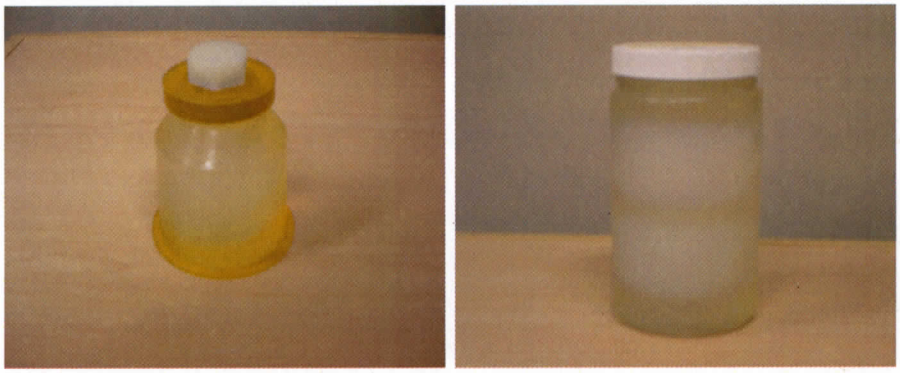

(a) (b)

Figure 3.7: Gel containers: (a) 500 mL Barex coffee cup phantom and (b) one litre Barex cylindrical phantom.

Litre volumes of NIPAM gel were prepared by weighing out 50 g of gelatin powder, 30 g of N-isopropyl acrylamide and 30 g of N, N'-methylene-bisaclylamide in separate 125 mL Erlenmeyer flasks and then mixing these chemical compounds with water, according to the following process: (1) 890 mL of deionized water was added to a two litre cylindrical glass jar. The water was then heated on an electronically operated hot plate (Fisher, Ottawa, Ontario), set to a target temperature of 45°C and stirred at 500-600 rpm for 5 minutes with a magnetic stirring rod. When the water temperature had risen to 30°C, 50 g of gelatin powder from the Erlenmeyer flask were poured into the water and allowed to mix for ten minutes. (2) After ten minutes, when the plate temperature had risen to approximately 35°C, 30 g N-

isopropyl acrylamide was added to the gel solution. (3) After a further 30 minutes, when the plate temperature had risen to 38°C, 30 g of N,N'-methylene-bisacrylamide was added to the gel solution. The target plate temperature was then dropped to 40°C to prevent chemical denaturation of the bis monomers due to heat shock. (4) After the addition of the N,N'-methylene-bisacrylamide, the preparation was allowed to mix for one hour until a homogeneous gel solution had formed. (5) After one hour, the preparation was removed from the hot plate and 4.625 mM (818.5μL) THPC oxygen scavenger was added to the gel solution. (6) The gel solution was immediately poured into either the 1 L or 500 mL Barex dosimetry container and housed in a fridge at 5°C to allow for gelation.

3.3 Polymer Gel Irradiation

The accuracy of fan beam OptCT dose readout was analyzed using three polymer gel irradiations. The radiation field arrangements for these irradiations varied from a basic single field geometry to a complex, seven-field, IMRT arrangement, as outlined below.

3.3.1 Treatment Planning

Each polymer gel irradiation performed for this study was pre-planned on the Eclipse treatment planning system. The dose distributions modeled with the planning system served as the gold standard against which to evaluate OptCT dosimetry. To generate a treatment plan, complete volumetric CT scans of both the one litre, cylindrical, Barex container and the 500 mL container were acquired. Prior to scanning, the one litre container was filled with a background gel and the 500 mL coffee-cup phantom was filled with water to simulate water equivalence of CT numbers inside the containers. CT scans were acquired utilizing a GE HiSpeed FX/i CT scanner (GE Medical Systems, Milwaukee WI) at the VIC using a tube voltage of 80 kVp, a tube current of 250 mA, a slice thickness of 2 mm, and a standard helical reconstruction

for a small field of view object.

After obtaining full CT volume sets, both containers were contoured in Eclipse to generate three-dimensional volumes of interest in Houndsfield units. Eclipse uses these volumes to calculate dose for a planned treatment. Altogether, three individual treatment plans were developed: The first plan consisted of a single, static, 3×3 cm^2 photon beam (6 MV photons, SSD = 98.5 cm) impinging through the bottom of the one litre Barex container. This treatment was planned and programmed into the treatment planning system using a prescription dose of 500 cGy (548 MU) at a depth of 1.5 cm from the bottom of the gel container to investigate small field and steep dose gradient dosimetry. The model generated for this treatment is indicated in figure 3.8(a).

Next, a four-field box arrangement with a 60^o wedge along the long axis (6 MV photons, SSD = 96.5 cm) was developed for delivery to the 500 mL, Barex container in order to investigate: (a) steep dose gradients in the axial plane of the OCT dose distribution, (b) moderate dose gradients in the z-axis of the three-dimensional dosimeter volume and (c) fields which impinge axially through the side of the container. The plan was prepared to deliver a prescription dose of 500 cGy to the isocenter, located at a 5 cm depth from the top of the container, as illustrated in figure 3.8(b). The field setup included fields directed axially through the phantom at 0^o (164 MU), 90^o (163 MU), 180^o (165 MU) and 270^o (163 MU) angles. Each of the fields was 4.5 cm in width in the x direction. A 60^o wedge modulated the dose distribution longitudinally in the z-direction, as indicated in figure 3.8(b).

Lastly, to investigate dosimetry of complex protocols with modulated dose distributions, a more involved, seven-field, intensity-modulated radiation therapy plan (6 MV photons, SSD = 98.5 cm) producing a ring-shaped dose pattern was developed for delivery to the one litre Barex container. The plan was developed using a prescription dose of 600 cGy to a ring structure, as illustrated in figure 3.8(c). The

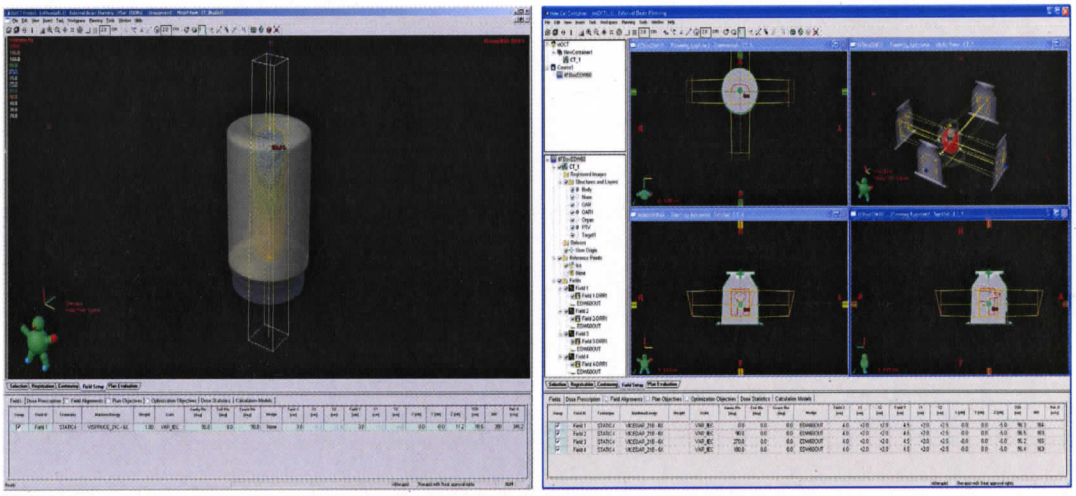

(a) (b)

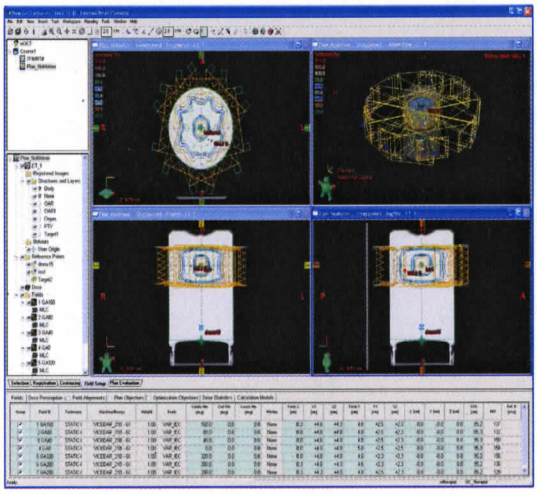

(c)

Figure 3.8: Eclipse treatment plan for (a) static 3 x 3 cm^2 photon beam delivered through the base of the one litre Barex container, (b) four-field box treatment plan delivered to 500 mL of NIPAM gel in the Barex, "coffee-cup" container and (c) seven-field IMRT distribution delivered to one litre of NIPAM gel in the Barex, cylindrical container

gantry angles, monitor units, and collimator settings are indicated in table 3.1.

Table 3.1: Gantry angles, monitor units and collimator settings for the seven-field IMRT plan delivered to the one litre, Barex container.

Gantry Angle(^{o})	Monitor Units	X-Field(cm)	Y-Field(cm)
160	137	(X1=4.0)+(X2=4.3)=8.3	(Y1=2.5)+(Y2=2.3)=4.8
80	132	(X1=4.0)+(X2=4.0)=8.0	(Y1=2.5)+(Y2=2.3)=4.8
40	150	(X1=4.0)+(X2=4.0)=8.0	(Y1=2.5)+(Y2=2.3)=4.8
0	158	(X1=4.0)+(X2=4.0)=8.0	(Y1=2.5)+(Y2=2.5)=5.0
320	156	(X1=4.0)+(X2=4.0)=8.0	(Y1=2.3)+(Y2=2.3)=4.6
280	136	(X1=4.0)+(X2=4.3)=8.3	(Y1=2.3)+(Y2=2.3)=4.6
200	129	(X1=4.3)+(X2=4.0)=8.3	(Y1=2.5)+(Y2=2.3)=4.8

3.3.2 Treatment Delivery

Polymer gel flasks were irradiated at room temperature, four hours post-manufacture, using 6 MV photons from a Varian CL21EX linear accelerator (Varian Medical Systems, Palo Alto CA). For the 3 $\times$ 3 cm^2, 6 MV photon field delivered through the bottom of the one litre Barex container, the gel was positioned upside-down on the treatment couch at a source to surface distance (SSD) of 98.5 cm. The LINAC gantry was stationed at an angular orientation of 0^o with respect to the central axis of the gel container, as shown in figure 3.8(a).

To irradiate the 500 mL, Barex coffee cup phantom with a four-field, wedged box arrangement, the coffee cup phantom was suspended horizontally in the path of the treatment beams using a specially designed stabilizing arm. With the gel suspended horizontally outward, treatment beams were then directed axially through the side of the gel container from 0^o, 90^o, 180^o and 270^o angles, as shown in figure 3.8(b).

Using the specially designed stabilizing arm, treatment beams were also delivered to the one litre, Barex container for the seven field IMRT plan. The treatment beams were delivered axially through the side of the container as indicated in table 3.1 and figure 3.8(c).

3.4 Polymer Gel Imaging

A fixed set of acquisition and reconstruction parameters was employed for dosimetric verification with the NIPAM polymer gels. However, to determine the effect of different reconstruction parameters on detector signal response, image contrast, spatial resolution and imaging time, a number of characterization tests with different acquisition parameters were initially undertaken.

3.4.1 Data Acquisition - Characterization Tests

To characterize the OptCT system, nine performance tests were employed. First, to determine the absorbance dynamic range of the system, the neutral density filter (NDF) was removed and an average intensity reading from 720 detector acquisitions of the laser fan beam through the matching medium solution was calculated. With no NDF in place, the detectors saturated, yielding a histogram of the full well capacity (FWC) of the arrays. The readout noise (Nread) of the detector arrays was then determined by acquiring the average of 720 detector readings with the laser source off and all ambient room lights also turned off. The absorbance dynamic range was calculated from the ratio of FWC to Nread.

Next, to ascertain the effect of tertiary collimation, the collimator was attached and two-hundred detector intensity readings through the matching solution were acquired. This same test was performed with a 3×3 cm^2 irradiated NIPAM gel (3 cm depth) in place. The collimator was then removed and these steps were repeated. This data was used to determine quantitatively the fraction of scattered light rejected by the collimator and the effect of tertiary collimation on absorbance measurements.

The firmware written with the scanner microcontroller allows digital configuration of photodiode array signal integration time between 250 ns and 25 μs. To determine the optimum detector integration time for collecting data, 200 static detector intensity readings of the fan beam through the matching solution were acquired for integration

times of 250 ns, 500 ns, 1000 ns, 2000 ns and 4000 ns. For each case, the standard deviation in pixel value of each detector over 200 acquisitions was calculated and the results for all detectors were averaged together.

OptCT images can be corrupted by the presence of geometric distortion appearing as a compression artefact when light rays refract at interfaces of differing refractive index within the scanned dosimeter volume. To characterize this effect, images of the needle phantom of figure 3.6 were reconstructed with the matching solution refractive index set at n=1.33 and n=1.35. The gel cylinder diameter and distance between two of the needles was then compared to the true physical dimensions, obtained using electronic calipers.

Next, the spatial resolution of the apparatus was examined by determining the point-spread and modulation transfer function of the OptCT system. The central slice at 5 cm depth from the gelatin phantom (5% gelatin and 95% water) with a 0.92 mm steel needle inserted along the midline was reconstructed (the finite width of the needle was deconvolved) to generate an image of the point-spread function of the OptCT system. By obtaining the area-normalized discrete Fourier transform of the deconvolved point-spread function, the modulation transfer function of the system was determined.

The temporal stability of the laser was analyzed by recording the intensity of all detector elements after laser warming periods of one minute, 30 minutes and one hour and a necessary warming time was identified for the laser.

Subsequently, to investigate system standard error in the projection domain, 200 acquisitions of the laser beam intensity through the matching medium tank were acquired over the course of five minutes. Using this data, the detector pixel standard error as a function of acquisition number was plotted. This same test was performed for the fan beam passing through the 3×3 cm^2 irradiated gel at 3 cm depth.

The presence of rings in reconstructed images with no gel in place was examined

by warming the laser for one hour and then recording 720 signal acquisitions of the fan beam through the matching solution at five minute intervals over the course of 25 minutes. For each successive five minute interval, an image was reconstructed. However, for all data sets, an average of the first 100 acquisitions from the first scan (0-5 mins.) was used as the calibration data. This experiment was designed to map the effect of any system temporal instability on reconstructed images and determine if laser or detector drift was resulting in ring artefacts in reconstructed images

The influence of the number of signal acquisitions per projection angle on reconstructed image signal-to-noise ratio, defined as the ratio of the mean pixel value in the irradiated region of an OptCT image to the standard deviation in pixel value in that same region, was observed by comparing SNR of OptCT reconstructed images of the NIPAM gel irradiated with a 3×3 cm^2 field, with two, four and eight signal acquisitions per projection angle. All reconstructions for this test were performed with 720 projection angles taken at 0.5^o increments.

3.4.2 Data Acquisition - Irradiated Gels

The three polymer gels irradiated for comparison of dosimetric accuracy of the OptCT system with Eclipse were scanned using the following scan parameters: 720 projections and 0.5 degree angular increments between projections, eight ADC averages per projection angle, 512×512 output image matrix size with each pixel representing a spatial distance of 0.23 mm in the scan plane. The gating time for each acquisition was 250 ns. The full scan time for a single slice was 16 minutes. Prior to scanning each irradiated polymer gel, a pre-calibration scan through the matching solution, consisting of 720 acquisitions, was executed. Similarly, a post-calibration scan consisting of 720 acquisitions was acquired after the transmission scan. The pre and post scans were averaged together to obtain a final calibration data set which accounts for any laser output drift, laser wobble, or linear detector gain increase or decrease.

Scans through the matching medium solution were used as the calibration data

sets for all experiments in this study. However, it would have been equally valid to use scans through an unirradiated gel for this purpose [43]. Scans through the matching medium solution were chosen because identical alignment of pre- and post-calibration scans is more difficult using an unirradiated gel. Further, it is quicker to obtain a large number of signal averages through the matching solution than it is to perform a full scan with rotation using a background gel.

3.4.3 Image Reconstruction

A Feldkamp, filtered backprojection reconstruction algorithm [37] in Matlab was used to reconstruct two-dimensional planes of optical density from the transmission and calibration data obtained for each scan. This CT reconstruction algorithm uses the distance from the lens (vertex) to the centre of rotation of the gel, the angular spacing between detectors, and the geometrical orientation of the detector array to re-bin fan projection data into projection data collected under parallel beam conditions. It then backprojects this data to calculate two-dimensional attenuation coefficients.

The reconstruction algorithm requires the position of the axis of rotation of the dosimeter to be at the centre of each transmission profile. This requires the centre of the dosimeter to be located exactly halfway between the centre of the line-generating lens and the centre-most detector element. To verify that the axis of rotation of the dosimeter was coincident with the centre of the transmission profile, the distance from the centre of the lens to the centre of the gel was measured using electronic calipers. Because of uncertainty in the position of the detector element, it was not possible to precisely measure the distance from the lens to the centre-most detector. The measured distance from the centre of the lens to the centre of the gel was used in the reconstruction algorithm to determine a theoretical pixel resolution ($0.2288 \frac{mm}{pixel}$) for the reconstructed OptCT images. Using this value in combination with the known outer physical diameter of 9.64 cm for the Barex, one litre gel cylinder (determined using electronic calipers), the angular separation of each detector used in the recon-

struction algorithm was altered until cylinder diameter in the reconstructed image matched 9.64 cm.

3.5 Data Processing Techniques

Image processing may be used either to enhance some property of a CT slice or volume or to restore detail which has been degraded by artefacts introduced in data acquisition or image reconstruction. The following subsection provides a brief overview of some of the relevant image processing methods used in this OptCT study.

3.5.1 Spatial Domain and Frequency Domain Image Processing Techniques

Reconstructed optical attenuation images produced with the fan beam scanner displayed faint ring artefacts. To compensate for this, five image enhancement methods were employed. The effect of these post-processing techniques on image accuracy was analyzed by calculating the mean and standard deviation in pixel value in the irradiated region of the gel images and using the ratio of these values as the signal-to-noise (SNR) ratio for comparison.

The first post-processing method applied was a median filter mask with a square neighbourhood of 10 $\times$ 10 pixels. The median, order-statistics filter ranks pixels contained in a given area encompassed by the filter and replaces the value of the center pixel with the median value determined by the ranking result. Such a filter was applied to the reconstructed image as one of the post-processing techniques. Three variants of the median filtering operation were also used: (i) median filtering in one dimension between 10 individual projection angle values for all detectors, (ii) median filtering in one-dimension between 10 individual detector absorbance values and (iii) median filtering in two-dimensions over a 10 $\times$ 10 neighborhood of the sinogram/projection data matrix. The principal goals of these additional filtering tests were to determine whether significant inter-projection or inter-detector variation

in intensity was causing rings and whether this variation could be suppressed.

A final method of post-processing the reconstructed OptCT images used Gaussian lowpass filtering (GLPF) in the frequency domain. To apply a Gaussian filter to the two-dimensional, cross-sectional images of the dosimetric verification phantoms, the following steps were applied:

1. The raw input image was multiplied by $(-1)^{x+y}$ to center the discrete Fourier transform of the image.

2. The discrete Fourier transform of the raw image was then computed.

3. The discrete Fourier transform of the image was multiplied by a filter function of the form, $H(u,v) = e^{\frac{-D^2(u,v)}{2D_o^2}}$ where D(u,v) is the distance from the origin of the Fourier transform and D_o is the cutoff frequency for the Gaussian filter (for the image in the Fourier domain, frequencies above this cutoff were eliminated from the data). A cutoff frequency of $D_o = 15$ was used for this study.

4. The inverse discrete Fourier transform of the image was computed.

5. The real part of this image was obtained.

6. The image was multiplied by $(-1)^{x+y}$ to account for the centering effect in step one.

3.5.2 Dosimetry Verification

Prior to dosimetry verification, a linear calibration curve of dose as a function of optical attenuation in the polymer gel was produced for doses in the region from 0 - 10 Gy (clinically relevant). The curve was generated by averaging optical attenuation coefficients in the irradiated region of the OptCT image of the 3×3 cm^2 gel at 1.5 cm depth (depth where the maximum dose is typically deposited for a 6 MV photon beam [5]). The average optical attenuation coefficient in this region was then compared to

the maximum Eclipse treatment planning system dose in the corresponding slice. In this manner, a single point was produced on a plot of dose (Gy) as a function of optical attenuation coefficient. Other points were interpolated from this value. Using the calibration curve, reconstructed images of optical attenuation were then converted to images of dose.

Four radiotherapy metrics were used to compare the dosimetric accuracy of the fan beam OptCT system to Eclipse. Specifically dose profiles, two-dimensional dose difference maps, contour plots, and depth dose curves were generated. The depth dose curve was generated by imaging slices of the NIPAM gel irradiated with a 3×3 cm^2 photon field at increasing depths. Singular values of dose at each depth were obtained by averaging the dose in the irradiated square region of the gel.

Chapter 4

Results and Discussion I - Development and Characterization of a Fan Beam OptCT Scanner

Fast, accurate and precise three-dimensional radiotherapy dosimetry using the fan beam OptCT system detailed in this research was only possible once proper characterization of the scanner had been performed. The principal goal of characterization was to identify the maximum accuracy, precision and speed of OptCT scanning under different conditions and thus determine whether or not clinical radiotherapy standards were being met. Oldham et al. [40] have suggested a 3D dosimetry system should meet a Radiotherapy Accuracy and Precision (RTAP) criteria consisting of a spatial resolution of $1\times1\times1$ mm^3, an imaging time of 60 minutes, a dose accuracy within 3%, and a precision within 1%.

Nine characterization tests conducted on the prototype OptCT scanner of this study are documented in this chapter: (1) The absorbance dynamic range is determined and the maximum theoretical dose resolution is derived from this. (2) The effect of the custom-machined tertiary collimator on rejection of scattered light is quantified. (3) The effect of increasing detector signal integration time on pixel standard deviation is outlined. (4) The presence of geometrical distortion in OptCT

images is analyzed with reference to the refractive index of the matching solution. (5) The spatial resolution of the system is identified using both a theoretical measure and an experimental measure (the modulation transfer function). (6) The temporal stability of the HeNe laser power output is examined. (7) The standard error of individual projections through the matching solution and through an irradiated polymer gel is determined. (8) The effect of system temporal instability is analyzed using reconstructed images of the matching solution. (9) The accuracy of the OptCT scanner, quantified using the signal-to-noise ratio in reconstructed gel images, is documented as a function of different numbers of acquisitions at each projection angle.

4.1 Absorbance Dynamic Range of Scanner

Before examining the absorbance dynamic range of the fan beam OptCT scanner, two relevant quantities must be defined: absorbance (A_λ) and optical density (OD_λ). When imaging three-dimensional dosimeters using a laser light source, absorbance quantifies the fraction of light absorbed or scattered from the dosimeter volume [43]:

$$A_\lambda = log_{10}(\frac{I_o}{I}), \tag{4.1}$$

where I is the intensity of light at a specified wavelength, λ, that has passed through a sample and I_0 is the intensity of the light before it enters the sample.

The absorbance is related to OD_λ as follows:

$$A_\lambda = \int_{Path} OD_\lambda(\mathbf{r})dl \qquad \text{or} \qquad OD_\lambda = \frac{A_\lambda}{l} \tag{4.2}$$

The goal of optical CT imaging is to reconstruct 3D maps of OD_λ which can be related to dose via an appropriate calibration. OD_λ is thus the analogue of the monochromatic linear attenuation coefficient, μ_E, in x-ray CT.

4.1.1 Photodiode Detector Absorbance Dynamic Range

One of the main properties of interest in imaging with the fan beam OptCT scanner is its maximum detectable range of absorbance in reconstructed optical density images. Maximum absorbance is dictated by the detector dynamic range (DR) which is the ratio of the pixel full well capacity (FWC) to the readout noise (Nread) [43]. FWC defines the amount of charge an individual pixel in the detector array can hold before saturating, while Nread indicates the number of electrons introduced per pixel into the final signal, upon the readout of the array. A histogram displaying the FWC of the Hamamatsu, S8865 series silicon photodiode arrays is illustrated in figure 4.1(a), while a histogram displaying the Nread for the OptCT system is shown in figure 4.1(b). To determine a specific value for Nread, the average pixel value over all detectors was taken.

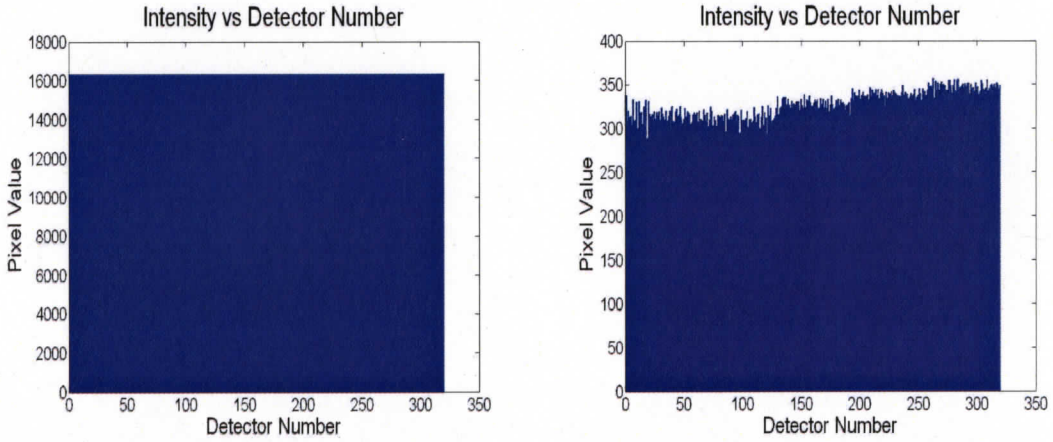

(a) (b)

Figure 4.1: Histogram displaying (a) full well capacity of the Hamamatsu, S8865 series silicon photodiode arrays and (b) readout noise of the photodiode arrays.

From figure 4.1(a) and figure 4.1(b), the DR of the photodiode array is given by [35]:

$$DR = \frac{FWC}{N_{read}} = \frac{16384}{328} = 49.95 \tag{4.3}$$

The absorbance dynamic range is then determined by using the relation [43]:

$$DR_A = log_{10} DR = log_{10}(\frac{16384}{328}) \approx 1.70 \tag{4.4}$$

4.1.2 Theoretical Dose Resolution

From the absorbance dynamic range (DR_A) defined above, the maximum theoretical dose resolution of the fan beam OptCT system may be approximated for a polymer gel irradiated to 3 Gy. More specifically, the dynamic range of detector pixel values for the photodiode arrays consists of detector intensity values between 328 (Nread) and 16383 (FWC). This corresponds to 16056 detector pixel values, each of which is converted to gray-scale units in the image-processing software. Assuming OptCT scans are performed with constant laser fluence and the full dynamic range of detector pixel values is exploited in generating a reconstructed image, the maximum theoretical dose resolution would be:

$$\textbf{Max Theory Dose Res (3 Gy)} = \frac{3\ Gy}{16056\ contrast\ units} = 0.187 \frac{cGy}{contrast\ unit} \tag{4.5}$$

For a polymer gel irradiated to 10 Gy, the maximum theoretical dose resolution would be:

$$\textbf{Max Theory Dose Res (10 Gy)} = \frac{10\ Gy}{16056\ contrast\ units} = 0.623 \frac{cGy}{contrast\ unit} \tag{4.6}$$

The maximum theoretical resolution in any computed tomography imaging sys-

tem is typically degraded because of the presence of statistical or electronic noise in projection data or image artefacts produced by the reconstruction algorithm.

4.2 Scatter Reduction Effect With Collimator

Optical density variations in polymer gel dosimeters result from the formation of radiation-induced scattering microparticle clusters 400-700 nm in diameter. Hence, the 543 nm fan of laser light passing through the gel is susceptible to the effects of scatter. When light is scattered, it deviates from straight ray paths and may be detected in the wrong element causing inaccuracies in reconstructed optical attenuation coefficients.

One method for reducing the effects of scatter in OptCT is the application of tertiary collimation. With the fan beam OptCT scanner, tertiary collimation in the form of a CNC-machined collimator with angled holes mimicking the dimensions of the detector elements was developed to reduce scattered radiation. In designing the collimator, the appropriate angle of orientation of each collimator hole was determined based on the angle of incidence of each principal ray. The primary goal in collimator design was to maximize the ratio of primary/scattered light arriving at each detector element. This goal had to be counter-balanced with the requirement for machining precise, square holes 0.7 mm in diameter separated by only a 0.1 mm spacer/septal wall. The following subsections detail the theoretical considerations and experimental tests undertaken in designing the tertiary collimator.

4.2.1 Theoretical Considerations for Collimator Manufacture

At the outset of collimator design, the maximum allowable collimator hole thickness (i.e. hole depth) was calculated. Specifically, the walls separating individual collimator holes become thinner towards the front side of the collimator since they mimic each ray of the fan beam and must be considerably more angled toward the outer detectors. This places a constraint on collimator hole depth because the collimator

wall would become overly thin toward the front side if the collimator holes were too deep. A schematic of this principle is displayed in figure 4.2. The width of each individual detector element is 0.7 mm, while the spacing between detector elements is 0.1 mm.

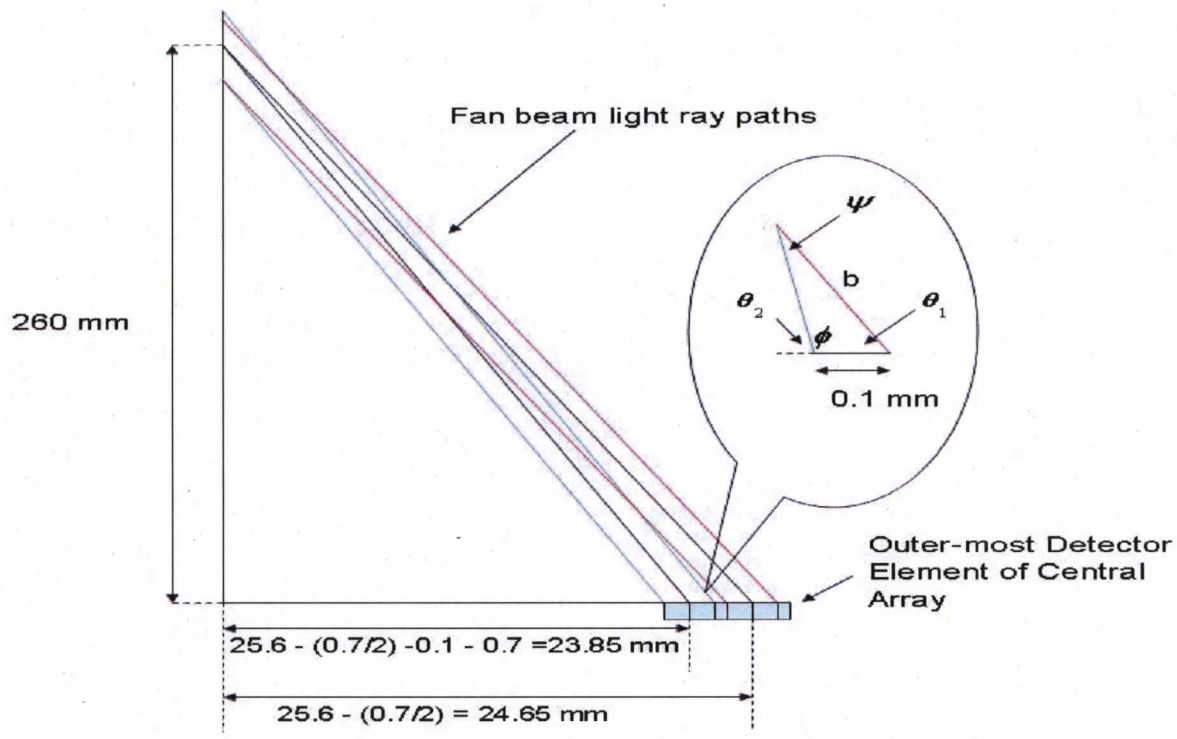

Figure 4.2: The maximum depth of tertiary collimator holes is indicated by the dimension, b, in the enlarged circle of the figure.

Figure 4.2 indicates that, if the walls of the tertiary collimation are thicker/deeper than a given terminal thickness denoted by the variable 'b', the wall of the collimator will become excessively thin and crumble upon machining. The value of the terminal thickness was calculated using geometric considerations. According to equation 4.7, the ray striking the outermost detector element on the right side of the central photodiode array of the scanner is subtended from the central beam axis at an angle θ_1, while the ray one detector to the left of this is subtended from the central beam axis at an angle θ_2.

$$\theta_1 = tan^{-1}\frac{260\ mm}{24.65\ mm} = 84.58^o$$
$$\theta_2 = tan^{-1}\frac{260\ mm}{23.85\ mm} = 84.76^o \tag{4.7}$$

The angles θ_1 and θ_2 can be used to determine the two interior angles ϕ and ψ of the enlarged triangle illustrated in figure 4.2:

$$\phi = 180 - \theta_2 = 95.24^o$$
$$\psi = 180 - \phi - \theta_1 = 0.18^o \tag{4.8}$$

With these angles now identified, the sine law allows for determination of the terminal collimator thickness, as shown in equation 4.9,

$$b = \frac{(0.1)sin(95.24^o)}{sin(0.181^o)} = 31.5\ mm = 3.15\ cm \tag{4.9}$$

Hence, the maximum collimator thickness for use with the fan beam OptCT system to allow detection of all primary rays is b = 3.15 cm.

4.2.2 Preliminary Central Axis Scatter Fraction Test

The collimator thickness of 1.5 cm was chosen by measuring the intensity of the laser fan beam along the central beam axis through an irradiated polymer gel irradiated to 10 Gy. This gel was used to simulate maximum scattering conditions. Intensity readings were acquired from a single Hamamatsu S1087 Series test photodiode. The S1087 photodiode was chosen because of its similar photosensitivity characteristics to

the arrays used with the scanner. Progressively increasing collimator thicknesses from 2.5 mm up to 2.25 cm were placed in front of the diode to measure the intensity drop associated with scatter rejection. This test was performed in ten separate trials. The data was averaged to reduce noise and plotted to determine an optimal collimator thickness (figure 4.3). The intensity registered by the photodiode along the central axis falls to a nearly constant value when collimator thicknesses of 1.5 cm through 2.25 cm are used, indicating that 1.5 cm is a sufficient level of collimation to reduce scattered radiation to acceptable levels along the central beam axis. With collimation thicker than 1.5 cm, only primary rays from the fan beam are recorded and there is no benefit to thicker collimation which is harder to manufacture with the CNC milling machine.

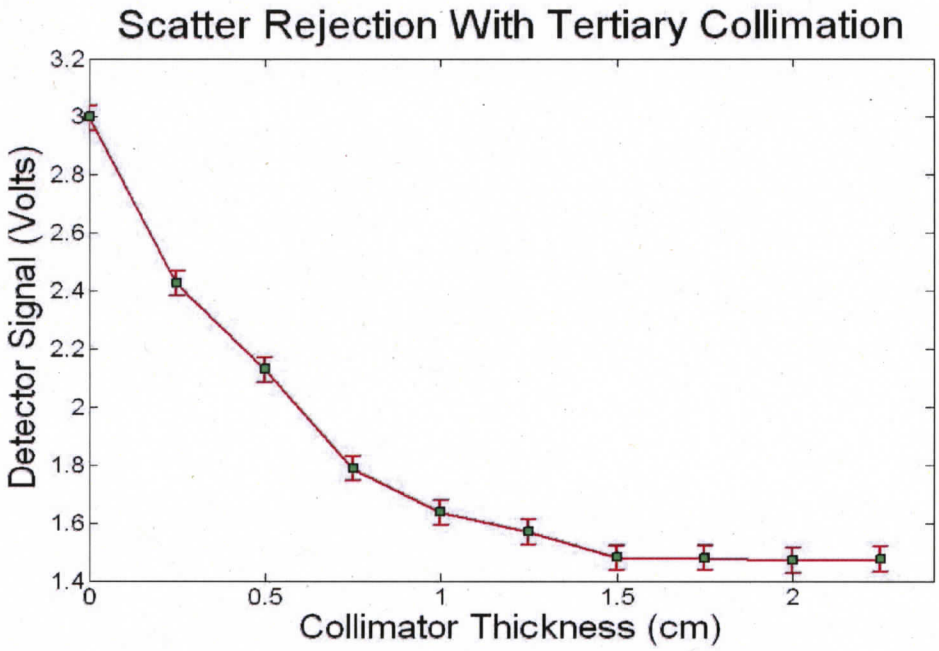

Figure 4.3: Hamamatsu S1087 Series test photodiode intensity along central beam axis through an irradiated gel with varying thicknesses of collimation placed in front of the diode.

4.2.3 Collimator Effect

The effect of introducing tertiary collimation is further examined in figures 4.4(c) and 4.4(d) which display histograms of detector intensity for the fan beam passing through the NIPAM gel irradiated with a 3 $\times$ 3 cm^2 field to a dose of 5 Gy. The histograms, shown with and without tertiary collimation, were generated by scanning a slice at a depth of 3 cm from the bottom of the one litre, Barex container. Light traveling to the center detectors is most prevalently scattered by the polymerized 3 $\times$ 3 cm^2 region. The average pixel value over detectors 110-200 for the collimated transmission scan was 2264, while a value of 4748 was obtained for the un-collimated scan. This indicates a 52% suppression in intensity values with tertiary collimation in place. However, it is inaccurate to attribute this reduction in intensity values solely to scatter rejection. As illustrated in figures 4.4(a) and 4.4(b), even with no gel in place, the collimator reduces incident light striking the detectors by approximately 39%. This is likely caused by the fact that most of the rays striking the detectors have deviated slightly from straight ray paths when traveling through the dosimeter medium, flask and matching medium tank. Rays that deviated only slightly from straight ray trajectories and were detected without the collimator may be absorbed in the collimator walls when the collimator is attached. Figures 4.4(a) and 4.4(b) were generated by scanning the fan beam through the matching medium solution with no gel in place and taking readings with and without tertiary collimation. Since a 39% reduction in intensity is seen in the calibration scans upon addition of collimation, the scattered light contribution eliminated by the tertiary collimation with a polymer gel in place is on the order of 13% of the total signal. This test was performed for a NIPAM gel irradiated to 500 cGy at a depth of 1.5 cm. For a similar gel irradiated to a lower dose, a smaller fraction of scattered light rejection would likely be observed

As a final examination of the effect tertiary collimation, absorbance values with and without the collimator in place were recorded. Absorbance was calculated ac-

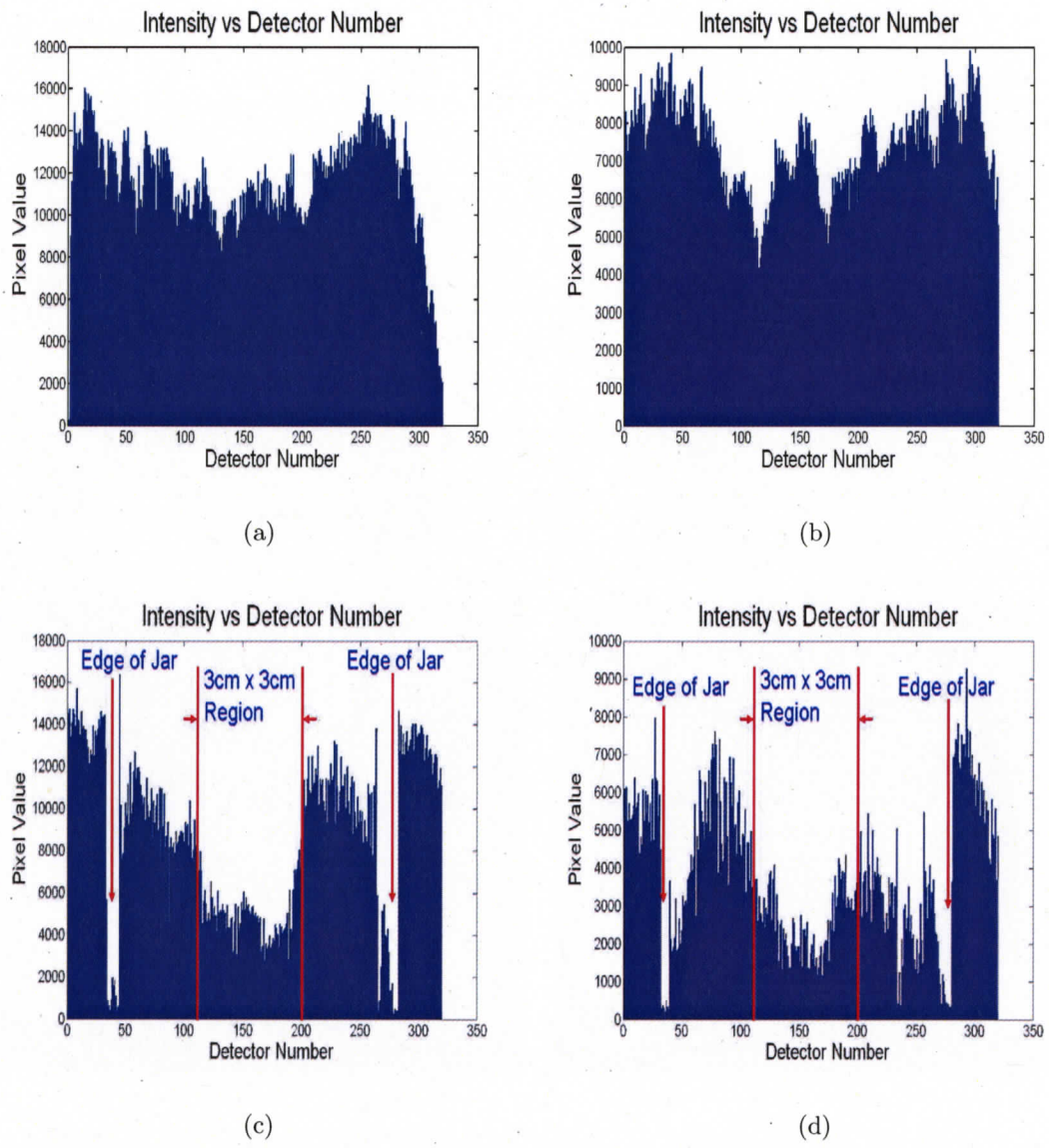

Figure 4.4: Histograms of detector intensity for the fan beam passing through (a) matching solution with no collimator in place, (b) matching solution with collimator in place, (c) 3×3 cm^2 gel at 3 cm depth with no collimator in place, (d) 3×3 cm^2 gel at 3 cm depth with collimator in place.

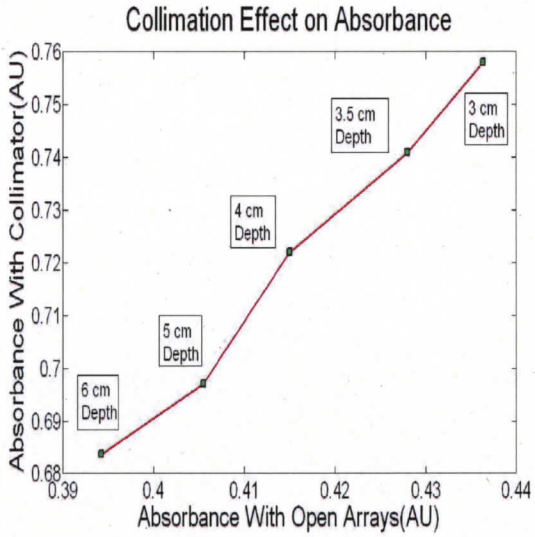

Figure 4.5: Collimator effect on absorbance measurements through slices of an irradiated polymer gel.

cording to equation 4.1. Absorbance measured by each detector in each projection is ultimately backprojected into the image space to reconstruct an OptCT image. Consequently, an increase in absorbance values with the collimator in place directly translates into improved image contrast. The results of the absorbance measurements with and without the collimator are shown in figure 4.5. The plot charts absorption coefficients with and without collimation for the fan beam passing through the 3 $\times$ 3 cm^2 irradiated NIPAM gel at depths of 3 cm, 3.5 cm, 4 cm, 5 cm, and 6 cm. On average, the absorption coefficient is found to be increased by 42% with the addition of the collimator. This indicates that a significant increase in contrast resolution in reconstructed OptCT images is possible with the tertiary collimator in place.

4.3 Standard Deviation in Pixel Value With Detector Integration Time

The standard deviation in pixel value as a function of integration time is plotted in figure 4.6. Raw pixel value is plotted instead of percent standard error because the optical density of the neutral density filter was raised as the integration time

was increased. The photodiode arrays were extremely sensitive and saturated if the neutral density filter level was not raised when the integration time was increased by 500 ns increments in this experiment.

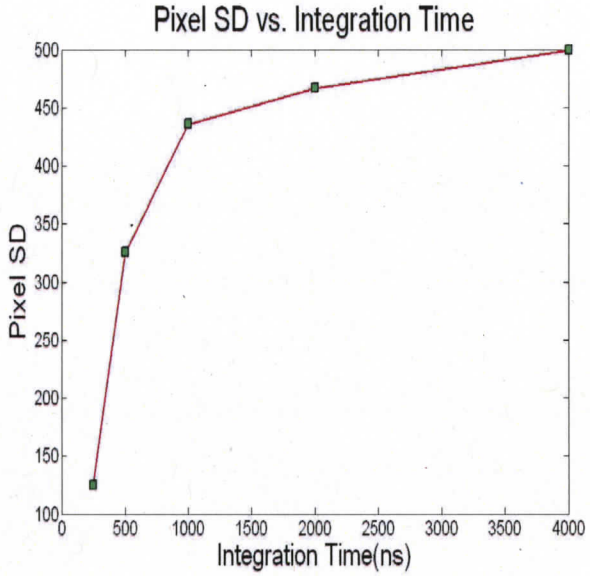

Figure 4.6: Standard deviation of detector pixel value about the mean as a function of detector integration time.

The effect of raising the optical density of the neutral density filter as the integration time was increased was compensated-for by scaling-up the detector intensities obtained at each successive integration time by a factor $10^{\Delta OD}$, where ΔOD represents the increase in the filter level from one integration time to the next. Consequently, in figure 4.6 an increase in integration time does not reflect an increase in the number of photons counted by the detector, as is the case in conventional x-ray imaging applications. The data from figure 4.6 illustrates that an increase in integration time and neutral density filter level leads to increased standard deviation in pixel value. This was likely due to increased variability in the laser light source signal when increased filter was introduced. From figure 4.6, 250 ns was chosen as the optimum integration time to reduce pixel standard deviation at each acquisition.

4.4 Examining for Geometric Distortion Effects

A common artefact in OptCT associated with light ray refraction effects is geometric distortion. Refraction results in distortion of reconstructed optical density maps when the attenuation of a ray is backprojected along a line which is not the same as the path actually traversed by that ray [30]. In this research, using both OptCT and x-ray CT, needle phantoms were imaged to examine the effects of geometric distortion.

4.4.1 Needle Phantom Test for Geometric Distortion

The influence of geometric distortion, based on refractive index mismatch between the tank solution and the polymer gel, was examined using a needle phantom. Images of the needle phantom were reconstructed with the matching solution refractive index set at n = 1.33 and n = 1.35. The gel cylinder diameter and distance between two of the needles was then compared to the true physical dimensions, obtained using electronic calipers.

Table 4.1: Magnitude of geometric distortion effects seen when the matching solution refractive index does not match that of the polymer gel.

	Gel Cylinder Diameter(cm)	Needle Separation(cm)
True Physical Distance	9.64±0.01	3.00±0.01
Image Distance(n=1.33)	9.51±0.01	2.94±0.01
Image Distance(n=1.35)	9.64±0.01	3.00±0.01

The magnitude of the geometric compression artefact seen in OptCT images is linear with the percent refractive index mismatch between the matching fluid and the gel. To minimize this effect, glycerol (index of refraction of 1.47) was added to the water (index of refraction of 1.33) in the tank solution to match the refractive index of the solution to that of the gel (1.35). Geometric compression artefacts are observed if the matching medium solution is not matched to the gel refractive index of 1.35, as indicated in table 4.1.

4.5 Spatial Resolution of Fan Beam OptCT System

In the following subsections, the spatial resolution of the OptCT system is calculated both theoretically and experimentally. The theoretical predictions are then compared to the experimentally determined value.

4.5.1 Theoretical Spatial Resolution

A theoretical value for the OptCT system spatial resolution is derived from geometric ray tracing. According to this model, a finite number of fan beam rays pass through the gel sample and are recorded by a finite number of detector elements. That being the case, the theoretical spatial resolution at the center of the gel cylinder can be determined by the geometric considerations illustrated in figure 4.7.

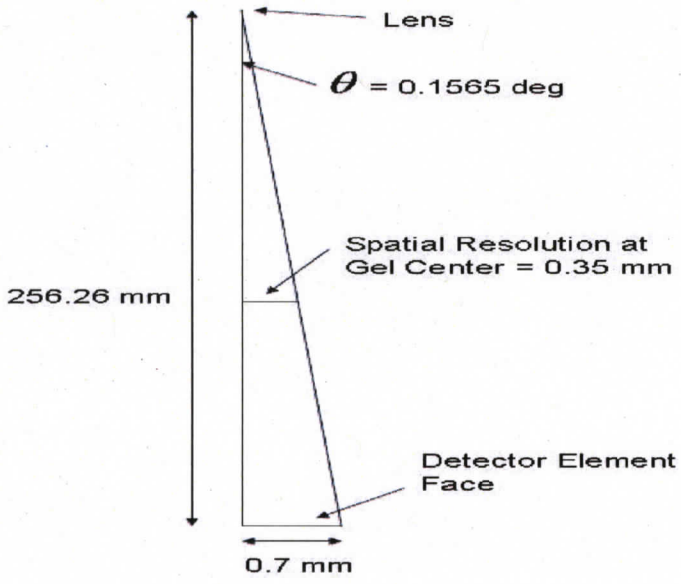

Figure 4.7: Theoretical spatial resolution at the center of the gel dosimeter, as determined by ray tracing.

Noting that the distance from the lens to the central detector is approximately 256±2 mm and the distance from the lens to the center of the gel cylinder is 128 mm (measured using electronic calipers), the angular increment of the first ray to the left or right of the central beam axis can then be calculated:

$$\theta = \arctan(\frac{0.7 \text{ mm}}{256 \text{ mm}}) = 0.1567^o \tag{4.10}$$

The theoretical spatial resolution at the center of the gel dosimeter is then given by SR in equation 4.11:

$$\text{SR} = \text{Tan}(0.1567^o) \cdot 128 \text{ mm} = 0.35 \text{ mm} \tag{4.11}$$

In radiography and CT imaging, spatial resolution is often expressed in line pairs per millimetre ($\frac{lp}{mm}$). The spatial resolution of the OptCT system in $\frac{lp}{mm}$ is given as follows:

$$\text{SR} = 2 \times 0.35 \text{ mm} = 0.70 \frac{\text{mm}}{\text{lp}} \text{ or } 1.3 \frac{\text{lp}}{\text{mm}} \tag{4.12}$$

The filtered backprojection algorithm used for reconstructing images from projection data in Matlab also defines a spatial resolution for the OptCT system. Specifically, the algorithm uses the distance in pixels from the lens to the center of the gel cylinder as an input for the reconstruction algorithm. For the OptCT images reconstructed in this research, a distance of 560 pixels was employed. This distance reconstructed the OptCT images with the proper magnification for viewing in a 512 $\times$ 512 matrix. When this figure is used in conjunction with the true physical distance from the lens to the center of the gel cylinder (128.13 mm, measured using electronic calipers), these two values define a spatial resolution of 0.2288 $\frac{mm}{pixel}$. Hence, the pixel spacing does not limit the system spatial resolution.

4.5.2 Modulation Transfer Function

To measure the spatial resolution of the fan beam OptCT system experimentally, a 0.92 mm steel needle was inserted along the midline of a 1 L background gel (5% gelatin and 95% water) housed in a transparent, cylindrical, 1 L Barex container.

A slice from this phantom was reconstructed (the finite width of the needle was deconvolved) to extract the point-spread function of the system. The modulation transfer function was then acquired by taking the area-normalized Fourier transform of the point-spread function. The MTF is plotted in figure 4.8. A common way of estimating the spatial resolution from the MTF is to record the inverse of the value along the x-axis at 30% of the y-axis value [38]. From figure 4.8, the value of spatial resolution after the MTF curve has fallen to 30% of its maximum value is 0.25 $\frac{mm}{lp}$. This compares to within 9% of the pixel resolution as defined by the reconstruction algorithm. The value of 0.25 $\frac{mm}{lp}$ or 4 $\frac{lp}{mm}$ corresponds to a spatial resolution approximately three times more accurate than the theoretically predicted value from equation 4.12. This may be due to the choice of the 30% point on the MTF curve used to score the spatial resolution.

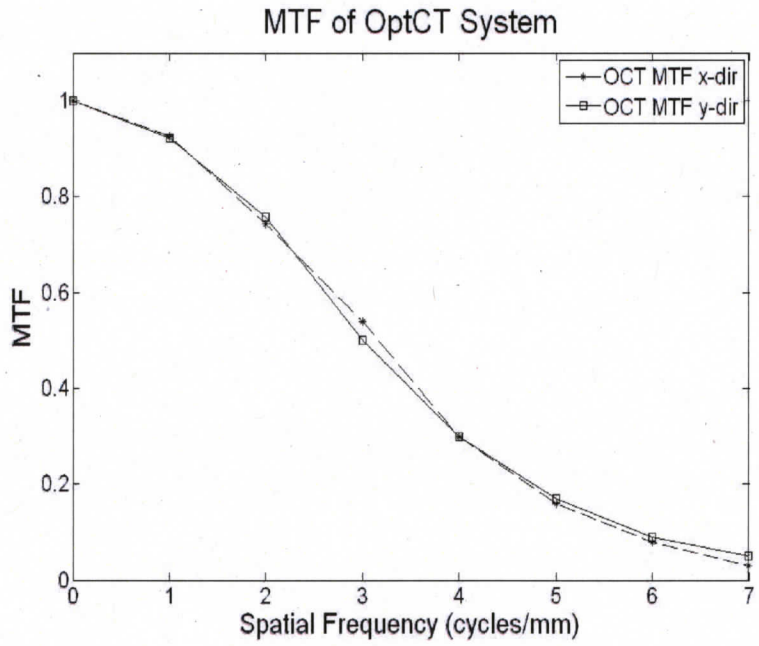

Figure 4.8: MTFs of OptCT imaging system obtained by Fourier transforming line profiles through a two-dimensional slice of the needle phantom in the x- and y-directions.

4.6 Precision of OptCT System in Projection Domain

In this study the precision of individual OptCT projections refers to the standard deviation in detector pixel value about the mean over a set of acquisitions. The precision of projection data was measured using static scans of the fan beam, both through the matching fluid and through polymer gel dosimeters of varying absorbances. Unless the effect of increasing the acquisition number on standard deviation in pixel value was being tested, 720 static acquisitions through the matching fluid or polymer gel phantom were continuously used in order to simulate real scan conditions. Measured in this manner, the precision of the fan beam OptCT system can underscore several characteristics of the imaging chain. In particular, laser power output variation, laser wobble and detector gain fluctuation can be examined [30].

Although the concentrated glycerol matching solvent mixed with water in the bath solution raised the refractive index of the matching liquid to approximately 1.35 in order to mimic that of the gel, it also introduced unwanted wavy patterns in the projection matrices (sinogram) which could at times translate into noise in reconstructed images. The effects of these factors on projection data acquisition and light source quality are examined in the subsequent subsections.

4.6.1 Precision of Static Projections Through Matching Fluid

Noise in fan beam OptCT absorbance measurements is affected by both noise in light-field/calibration scan measurements through the matching medium solution and noise in each projection through the dosimeter [43]. Consequently, it is critical to independently characterize the behaviour of the system in both these situations.

The laser required a one hour warm-up time to stabilize to a constant intensity. The pre-warm-up laser fluctuation is illustrated in figures 4.9(a), 4.9(b) and 4.9(c) which plot intensity for detector elements 32, 96, 160, 224 and 288 after one minute, 30 minutes and one hour laser warm-up periods. Notably, minor phase discrepancies

between the five charted diodes persist until the one hour warm-up period is reached. After one hour, the five detector pixels show a constant response to within an average of 0.7% of each of their mean values. Figure 4.9 does not isolate the response of the laser as a function of time but demonstrates both the combined effect of variation in laser power and detector gain during the warm-up period.

A histogram illustrating the intensities of all 320 photodiode detector elements for a scan of the fan beam through the matching solution with the collimator in place is displayed in figure 4.10(a). The variation in intensity from one detector to the next demonstrates the non-identical gain characteristics of each detector element.

Figure 4.10(b) presents a colour map of detector intensity as a function of 720 static acquisitions through the matching fluid. All detector intensities have been normalized to the intensities of the first acquisition. Very little change in detector intensity (1.47% on average for all detectors) occurs over the course of 720 acquisitions. However, one noteworthy feature of the sinogram data illustrated in figure 4.10(b) for a set of 720 static acquisitions (taking approximately 4 minutes) through the matching fluid is the presence of translucent wavy lines (most apparent for detectors ~240-275 at acquisition numbers ~30-200). The lines appear in the sinogram matrices as a result of movement of the glycerol solute in the matching solvent when the tank medium is disturbed. Although the wavy appearance of the lines is noticeable in the sinogram image, the percent difference in intensity between two adjacent pixels affected by the lines was never found to be more than 5.24%. If the glycerol solution is allowed to sit for at least two minutes after suspending the polymer gel for OptCT scanning, the effects of the wavy patterns are minimized because the glycerol either dissolves into the water component of the matching solution or settles to the bottom of the matching tank.

The significance of the glycerol matching solvent is underlined by comparing the calibration scan through the water tank with no matching fluid, figure 4.11(a) with

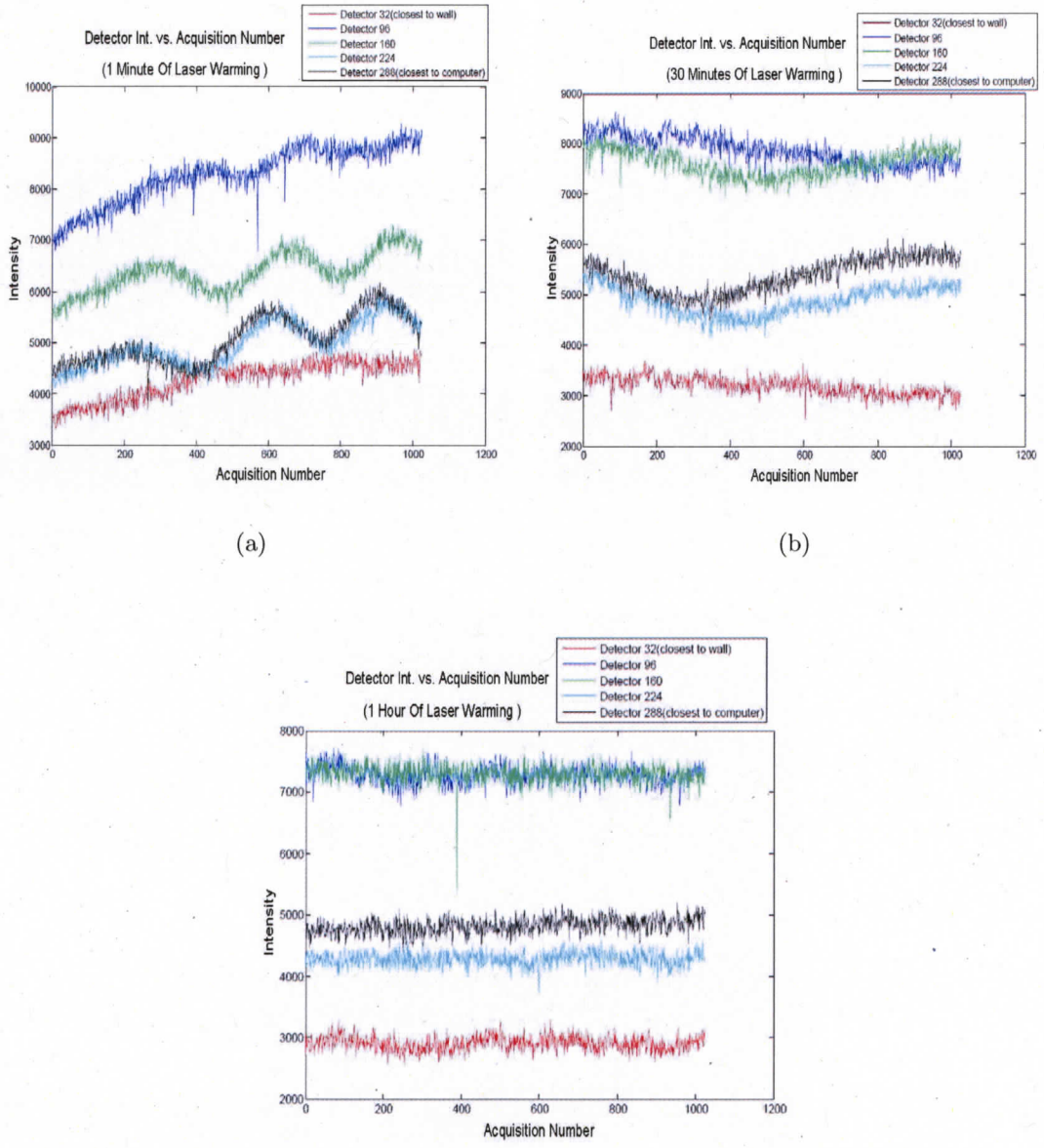

Figure 4.9: Intensity of detector elements 32, 96, 160, 224 and 288 after laser warming period of (a) one minute, (b) 30 minutes, (c) one hour.

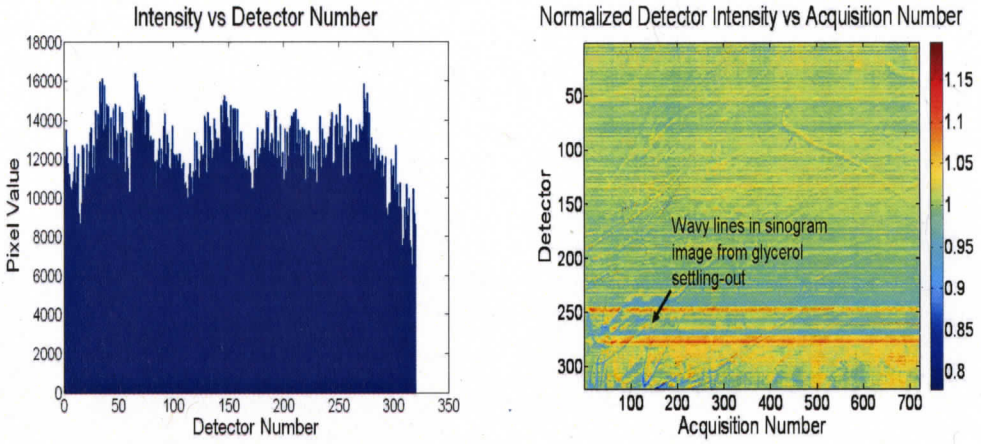

(a) (b)

Figure 4.10: For a scan of the fan beam through the matching solution (a) histogram of detector intensities and (b) detector intensity as a function of acquisition number (intensities normalized to the intensity of the first acquisition).

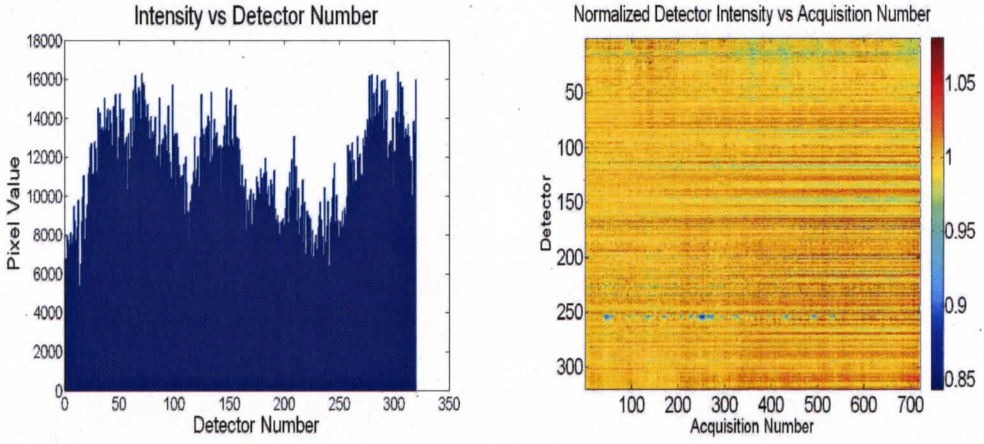

(a) (b)

Figure 4.11: For a scan of the fan beam through only the tank with no matching solution (only air in the scanning tank) (a) histogram of detector intensities, (b) detector intensity as a function of acquisition number (intensities are normalized to the intensity of the first acquisition).

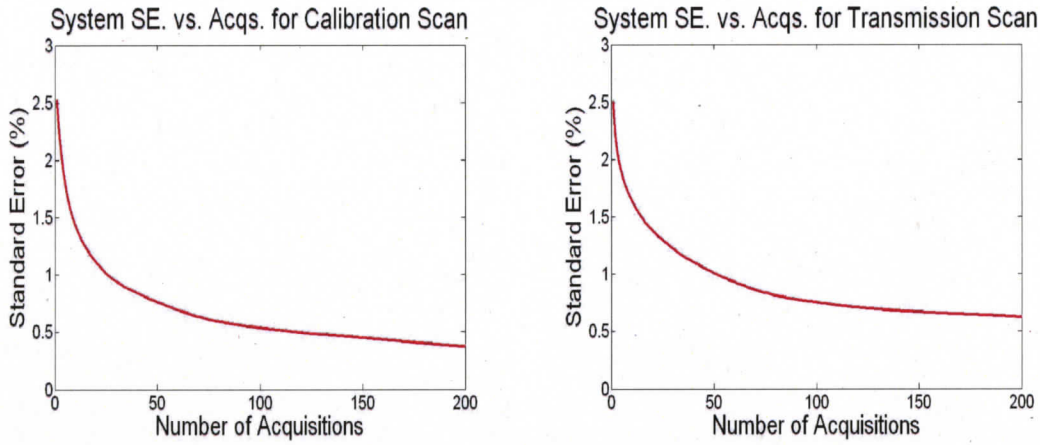

(a) (b)

Figure 4.12: Standard error as a function of acquisition number in (a) calibration scan through the OptCT tank matching fluid, (b) transmission scan at a depth of 3 cm through a NIPAM polymer gel irradiated with a 3×3 cm^2 square photon field through the bottom of the one litre Barex cylinder.

figure 4.10(a) where the glycerol matching fluid is present. In figure 4.10(a), the glycerol solution minimizes the intensity variation from one detector to the next, while in figure 4.11(a) individual variation from one detector to the next is more severe. The intensity variation in figure 4.11(a) is caused by refraction of individual light rays away from the desired straight paths when the rays pass through the front tank wall into the air of the matching tank and from the air of the matching tank into the back wall.

To independently characterize the standard error in both the calibration and transmission scan measurements, two simple experiments were performed. First, a static projection scan consisting of 200 acquisitions of the OptCT fan beam through the glycerol/water matching fluid was conducted. Using the data from the 200 acquisitions, the standard error in pixel value over all acquisitions for each detector was calculated and a mean standard error for all detectors determined. This standard error is plotted in figure 4.12(a). After 200 acquisitions, standard error in the

Table 4.2: Standard error as a function of acquisition number for both calibration and transmission scans.

Acquisition Number	Calibration Scan SE(%)	Transmission Scan SE(%)
4	1.94	1.98
8	1.55	1.73
16	1.22	1.47
32	0.92	1.20
64	0.67	0.91
128	0.49	0.70
155	0.45	0.67
175	0.41	0.65
200	0.34	0.62

calibration scan data decreases to 0.34%. A second identical test was performed to identify noise in transmission scans. The 3×3 cm^2 NIPAM gel was set in place and the fan beam was scanned through it at a depth of 3 cm. Standard error as a function of acquisition number was calculated for this arrangement, as before. The result is plotted in figure 4.12(b). After 200 acquisitions, standard error in transmission data drops to 0.62%. These results characterize the noise-to-signal ratio for the calibration and transmission projection data. Alternatively, the results can be interpreted as the system projection signal-to-noise ratio: for the calibration scan SNR = 100/0.34 = 294:1 and for the transmission scan SNR = 100/0.62 = 161:1. Table 4.2 displays the standard error of calibration and transmission projection data as a function of varying acquisition number. As expected from the laws of sampling statistics, with increasing acquisition number, the measurement standard error or statistical noise in the projection data decreases.

4.7 SNR of OptCT System in the Reconstruction Domain

Two parameters which differentially affect image quality in OptCT are the number of projections used in collecting the CT data, as well as the number of signal acquisitions averaged at each projection angle. Accordingly, one goal of the characterization process was to optimize both the number of projection angles and the number of

acquisitions at each projection angle in order to maximize OptCT image spatial resolution, while minimizing data acquisition and reconstruction time.

Reconstructing images with no dosimeter in place allowed for a reduction in complexity of the scanning chain and was used specifically to investigate whether the presence of ring-artefacts, seen in irradiated polymer gel images produced with the fan beam OptCT system, was a result of temporal instability in laser output or detector gain.

To test for improvement in image quality by increasing the number of acquisitions at each projection angle, a phantom material representative of irradiated 3D dosimeters was necessary. The NIPAM polymer gel irradiated with a 3×3 cm ^{2} photon beam was chosen for this characterization test because of its similar composition to the four-field box and seven-field IMRT dosimetry gels used for verification later in this research.

4.7.1 Appropriate Number of Projections for Each Scan

Collecting fewer projection angles with the fan beam OptCT system results in a shorter total scan time, as indicated in the histograms in figure 4.13. The histograms also demonstrate that scan time increases linearly when five to twenty acquisitions per projection angle are employed. The scan time is faster when a single acquisition per angle is used since data from multiple acquisitions does not have to be stored and averaged together in code. For a scan performed with one acquisition per angle and 0.5 degree projection increments, the total scan time is four minutes and 28 seconds. Four minutes and four seconds of this time is spent running the Matlab-based data acquisition code on the PC while just under 24 seconds is required to port the data from the microcontroller to the PC. The time required to scan the photodiode arrays, 0.288 ms, is not a limiting factor. The system software is currently being optimized in C++ to reduce total scanning time.

The RTAP criteria outlined at the outset of this chapter suggests a one hour

scan time for dosimeter volumes is practical for clinical implementation of OptCT in a radiotherapy environment. Yet, in order to obtain 3% accuracy, also suggested by the RTAP criteria, and avoid streaking artefacts, the dosimeter slice must be sampled with enough projection angles to allow approximately a 1:1 ratio of data points to points in the reconstructed 512 × 512 OptCT image. For this requirement, approximately 512 × 512 = 262144 data points would have to be collected in the sinogram. Such a theoretical argument indicates a projection data matrix collected with 360 projections or 360 × 320 = 115200 data points may result in undersampling artefacts. A projection data matrix with 720 projections or 720 × 320 = 230400 data points is less susceptible to aliasing artefacts. Therefore, 720 projections were used for the scans in this research.

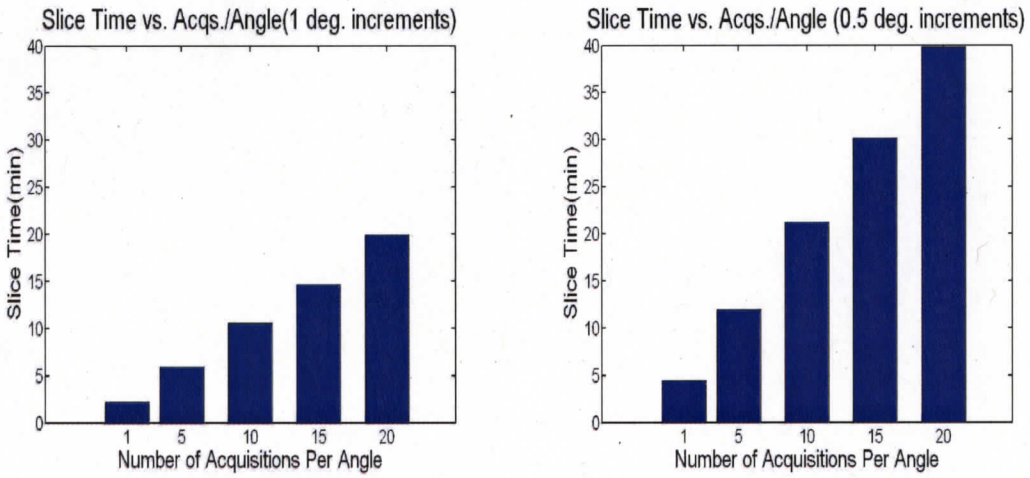

(a) (b)

Figure 4.13: Histogram indicating the time required to scan a slice as a function of the number of signal acquisitions at each projection angle for (a) 360 projection angles and (b) 720 projection angles.

4.7.2 Temporal Stability of OptCT System

The 320 photodiode detectors used for light detection in the OptCT system have different amplification gain values which change slightly over the course of a scan.

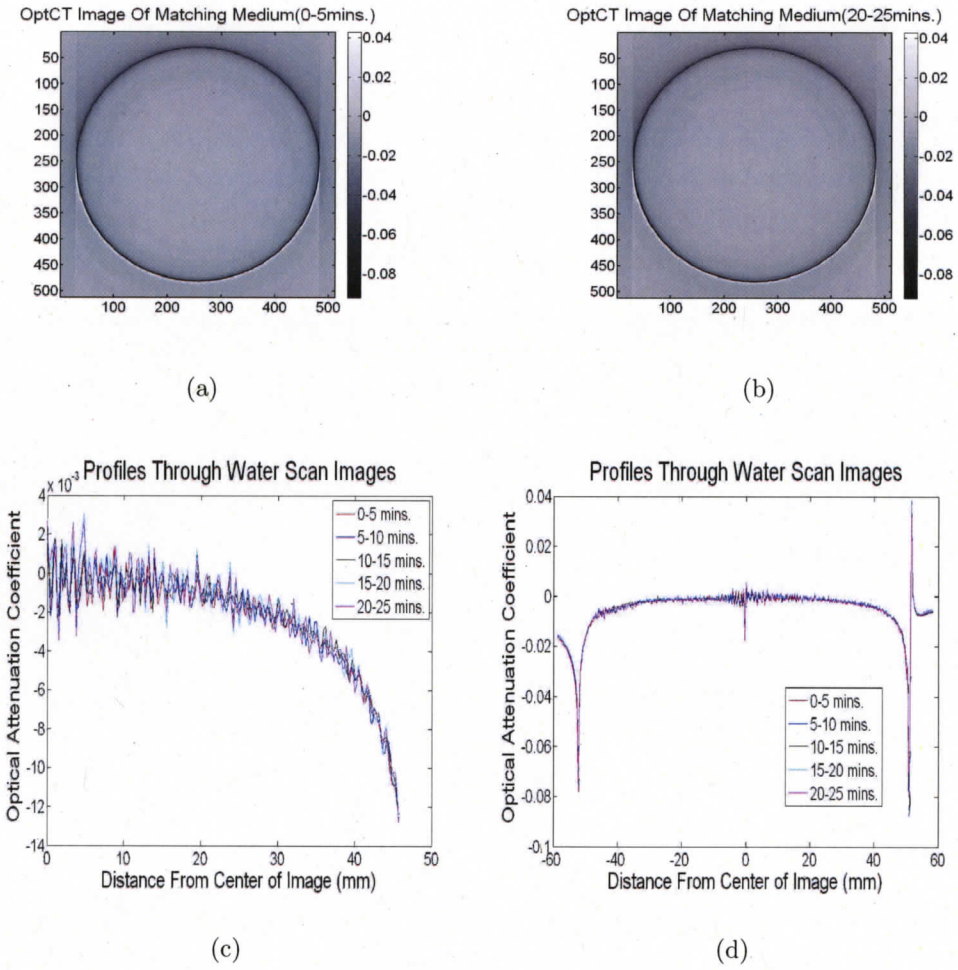

Figure 4.14: OptCT image of the fan beam through the matching solution generated (a) 0-5 mins. after one hour laser warm-up, (b) 20-25 mins. after one hour laser warm-up. (c) OD profile moving radially outward 4.56 cm from the center of the reconstructed images. (d)OD profile across the complete length of the images.

To characterize the effect of this gain non-uniformity, as well as any laser power output variation on reconstructed images, the laser was warmed for one hour and 720 static acquisitions of the fan beam through the matching solution were acquired at five minute intervals over a course of 25 minutes. For each successive five minute interval, the projection data set that was collected was used to reconstruct an image. However, for all data sets, an average of the first 100 acquisitions in the first scan (0-5 mins.) was used as the calibration data. This experiment was designed to map the effect of any temporal system instability on reconstructed images. If the laser power or detector gain had varied notably for transmission scans taken in the time frame from 10-25 minutes, rings in the reconstructed images would have been accentuated. A comparison of figures 4.14(a) and 4.14(b) demonstrates that, as a function of time, the ring artefacts do not increase noticeably in the reconstructed images of the matching medium. This observation is supported by figure 4.14(d) which displays overlaid line profiles through the y-axis of each of the images. Notably, the variation in optical density does not change dramatically as a function of time. The plot also demonstrates that variation in optical density due to faint rings in the water scan reconstructions is largest at the center of the image where a variation of 0.0016 optical density units is seen. For relative comparison, the maximum optical density in the irradiated region of a reconstructed OptCT image of the NIPAM polymer gel irradiated with a 3×3 cm^2 photon field at a slice depth of 1.5 cm was 0.009 optical density units. Using this value, the rings may result in an 18% contribution to structural noise at the center of a raw OptCT image. The variation in optical density decreases to a steady value of 0.0004 (only 4% noise contribution using the previous statistic) at a distance of 15 mm radially outwards from the center of the image. This is illustrated in figure 4.14(c). The gradual drop in optical attenuation coefficients towards the ends (-40 and 40 mm respectively) of the line profiles in figure 4.14(d) and figure 4.14(c) is caused by the loss of transmission data in the vicinity of the

cylinder wall.

Two calibration procedures were attempted to account for the ring artefacts in OptCT images caused by detector temporal instability. First, the standard deviation of individual detector intensities over the course of 720 acquisitions of the fan beam through the matching solution was recorded. This was performed in ten separate trials and the results were averaged together. The data was then used to normalize each calibration data. However, due to the non-linear temporal response of the photodiode detectors, this procedure did not successfully reduce ring artefacts. A second technique involved subtracting "background" images of the matching solution (i.e. no dosimeter in place) from images of irradiated polymer gels. This method was unsuccessful because the ring positions in the background images were not the same as they were in the irradiated gel images.

4.7.3 Appropriate Number of Acquisitions at Each Projection Angle

A second characterization test, analyzing the effect of number of acquisitions per projection angle on reconstructed image SNR, was performed using the NIPAM polymer gel irradiated with a static 3 x 3 cm^2 photon beam. Cross-sectional images of this gel were reconstructed at a depth of 1.5 cm and the mean and standard deviation in pixel value in the polymerized region of the gel were calculated. The SNR was characterized as the ratio of mean to standard deviation in pixel value in the polymerized area. The images used for this experiment were acquired with two, four and eight acquisitions per projection angle and post-processed using a 10 $\times$ 10 sinogram median filter. They are illustrated in figure 4.15. A plot of reconstruction domain SNR as a function of acquisition number is shown in figure 4.15(d) and denotes an increase in reconstruction domain SNR as a function of acquisition number. This increase must be balanced with the increase in time required to take multiple acquisitions at each angle, as demonstrated in figure 4.13(b). In general, in order to minimize reconstruction time and maximize reconstruction domain SNR, eight acquisitions were

used for the OptCT scans in this study. Further research into scanning with higher acquisition numbers per projection is being investigated.

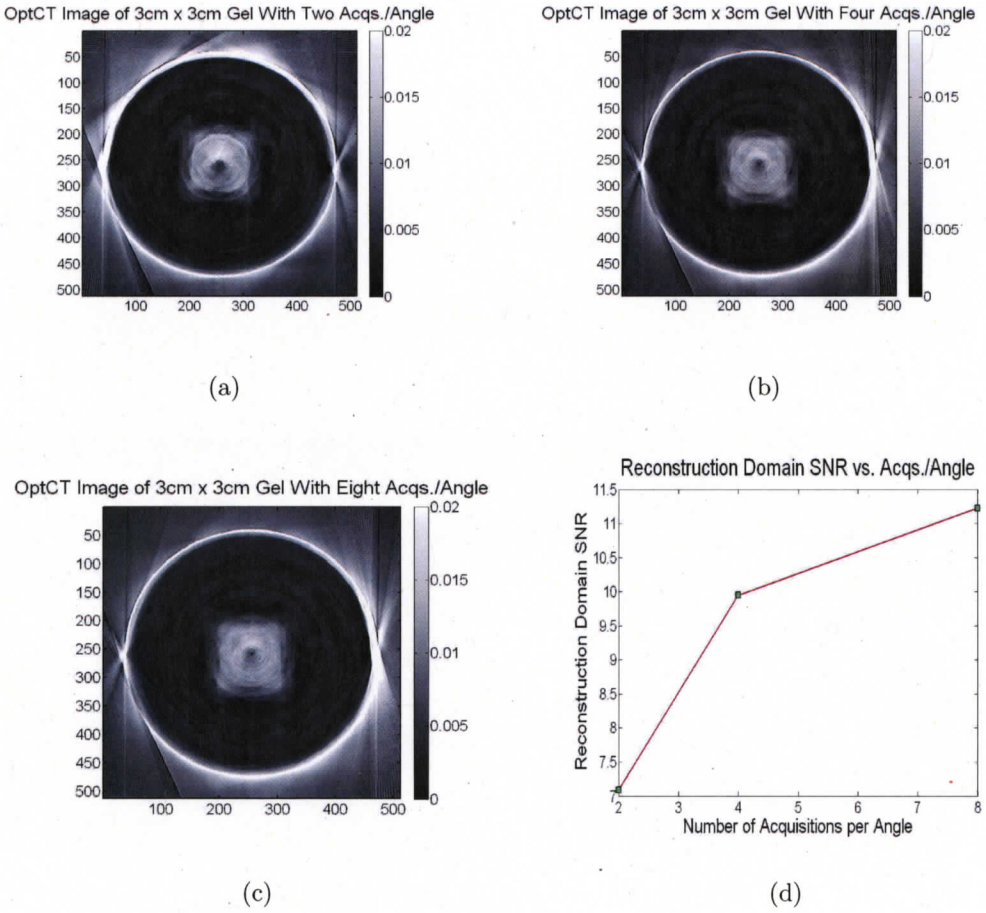

Figure 4.15: OptCT images of the 3 × 3 cm^2 gel at 1.5 cm depth, sinogram-median filtered with a 10×10 median filter with (a) two signal averages per angle, (b) four signal averages per angle, (c) eight signal averages per angle. (d) Reconstruction domain SNR as a function of acquisition number.

Chapter 5

Results and Discussion II - Reconstructed OptCT Images of Irradiated Polymer Gels

The central focus of this chapter is to examine reconstructed OptCT images of irradiated polymer gels. In particular, the chapter addresses reconstructed images of optical attenuation coefficients, conversion of these attenuation coefficients to dose values and comparison of experimentally measured OptCT dose distributions to modeled dose distributions from a commissioned Eclipse treatment planning system.

Three separate dosimetry verification experiments are documented in this chapter. Each experiment begins with a discussion of images of optical attenuation coefficients and filtering methods used to improve reconstruction domain signal-to-noise ratio (SNR), defined as the ratio of the mean pixel value to the standard deviation in pixel value in the polymerized region of the gel image. Conversion of OptCT attenuation images to dose images is then examined. Finally, each section concludes with a quantitative comparison of OptCT and Eclipse dose distributions.

5.1 3×3 cm^2 Field Irradiation

The first dosimetry verification experiment involved a single 6 MV photon beam (field size = 3×3 cm^2, SSD = 98.5 cm) with 500 cGy delivered to a depth of 1.5 cm in one litre of NIPAM gel. The gel was contained in a cylindrical Barex container. The

treatment beam was delivered through the base of the cylindrical container. The goal of this experiment was to investigate small field and steep dose gradient dosimetry.

5.1.1 OptCT Optical Attenuation Images

The first step in experimental dosimetry verification involved reconstructing optical attenuation images of the 3×3 cm^2 irradiated gel. Prior to scanning the dosimeter, 720 static calibration acquisitions of the fan beam through the matching fluid were obtained. A histogram of detector intensities from this calibration data is illustrated in figure 5.1(a). All calibration scan intensities were viewed after collection to ensure a relatively homogeneous intensity of light was striking each detector. After the calibration data was collected, the optical density of the neutral density filter was lowered from 1.95 to 1.45 for the transmission scan. A lower filter optical density was used because, with the gel in place, a higher incident intensity of fan beam light can be passed through the OptCT system without saturating the detectors. When the optical density of the neutral density filter was left unchanged at a value of 1.95 for the transmission scan, the central detectors, which register light passing through the gel, recorded the dark state pixel value of 328 and the transmission data was not useful for reconstruction.

Following the calibration scan, a test transmission scan through the dosimeter was performed to ensure detectors were not saturating or reading the dark state value and to determine if a large portion of the detector dynamic range was being exploited, as required for high contrast in OptCT. The data for this scan is shown in figure 5.1(b). Data was lost in the vicinity of detectors 45 and 275 where the edges of the gel cylinder caused light to refract away from the corresponding detectors. In the reconstruction algorithm, data from these detectors is removed, as is data from the outer detectors (0-40 and 280-320) which receive light that does not pass through the gel cylinder. Transmission data at all 720 angles was subsequently collected with eight acquisitions per angle. Eight signal acquisitions were performed at each

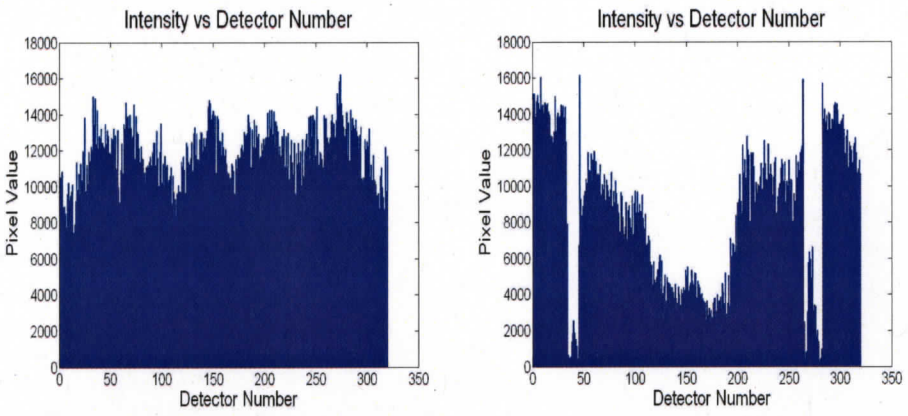

(a) (b)

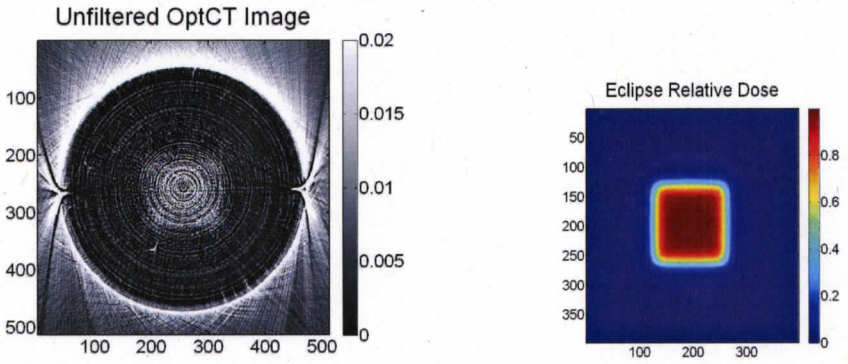

(c) (d)

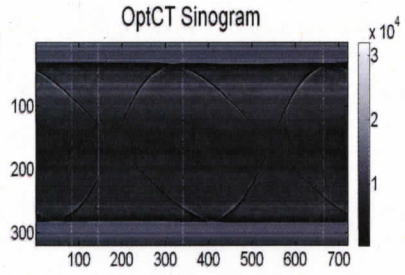

(e)

Figure 5.1: Data for the 3×3 cm^2, irradiated NIPAM gel at a depth of 3 cm showing (a) single calibration acquisition of the fan beam through the matching fluid, (b) single transmission acquisition, (c) raw, reconstructed OptCT image, (d) Eclipse dose, (e) sinogram data.

projection angle to maximize the signal-to-noise ratio, while minimizing acquisition time. The calibration data was then scaled up by a factor of $10^{0.5}$ to account for lowering the optical density of the neutral density filter for the transmission scan.

The reconstructed OptCT image of the 3 × 3 cm^2 gel at 3 cm depth is given in figure 5.1(c). The square 3 × 3 cm^2 region where polymer has formed in the gel is accurately depicted in the reconstructed image, as is the outer edge of the gel cylinder. No additional polymerization has occurred in the un-irradiated region of the gel. As well, the magnitude of the optical attenuation levels in the image reflect the dose deposited in the gel. At the left and right-most segments of the gel cylinder, an artefact due to refraction of light rays at grooves in the cylindrical container is visible. Light ray refraction from these grooves did not noticeably contaminate reconstructed optical attenuation images. The presence of ring artefacts 2-4 pixels in line width in the reconstructed image led to the introduction of filtering operations to improve image quality (see section 5.1.2). The Eclipse dose image of the 3 × 3 cm^2 gel at 3 cm depth is shown in figure 5.1(d) for comparison with OptCT. The sinogram data for this scan, shown in figure 5.1(e), identifies evidence of significant and variable attenuation in the irradiated region of the gel dosimeter.

5.1.2 Filtered OptCT Images

The addition of 1.5 cm tertiary collimation quantitatively reduced the effect of scattered light contaminating OptCT projection data by as much as 13%, as indicated by the intensity histograms in chapter four, resulting in improved image contrast. On the other hand, the collimator increased intensity differences between adjacent detector elements. Because each detector element backprojects to an individual ring in the OptCT image with the fan beam scanner, these intensity differences are a possible source of ring artefacts in the reconstructed images. Although the rings were not located at characteristic positions in the frequency or spatial image domains, as would be the case if they were caused by detector gain inhomogeneity, they were 2-4

pixels in line width on average. This trend was particularly apparent in the region of the reconstructed image where dose had been recorded.

To reduce the effects of ring artefacts, five image processing operations were investigated. The goal of this image processing analysis was to determine whether significant inter-projection or inter-detector variation in intensity was causing the ring artefacts and whether that variation could be suppressed. The effectiveness of each image processing method was quantified, based on the SNR of the output OptCT image. SNR was again defined, for consistency, as the ratio of the mean pixel value to standard deviation in pixel value in the polymerized region of the gel image.

The first image processing method employed median filtering in the spatial domain. Each pixel in the output image was assigned the median value of a 10×10 pixel (2.5×2.5 mm^2) neighbourhood in the input image. The 10×10 neighborhood was selected to maximize image SNR and minimize blurring. The median filtering technique is particularly useful for reducing the effect of segmented ring artefact noise in OptCT images because unrepresentative pixels with low attenuation coefficients in a ring do not noticeably affect the median value in the filtering operation [52]. This filter also does not create new unrealistic pixel values in the presence of ring artefacts. The result of applying this processing step to the image is displayed in figure 5.2(a).

Three variants of the median filtering operation were explored: (i) median filtering pre-reconstruction, grouping 10 individual projection angles together. The result of this operation is illustrated in figure 5.2(b). (ii) median filtering pre-reconstruction, grouping 10 individual detector absorbance values together. The post-processed image from this method is shown in figure 5.2(c). (iii) median filtering pre-reconstruction in two-dimensions, using a 10×10 pixel square neighbourhood to group together square areas in the sinogram data. This result combines both projections and detector elements in the median filtering. The effect of this processing

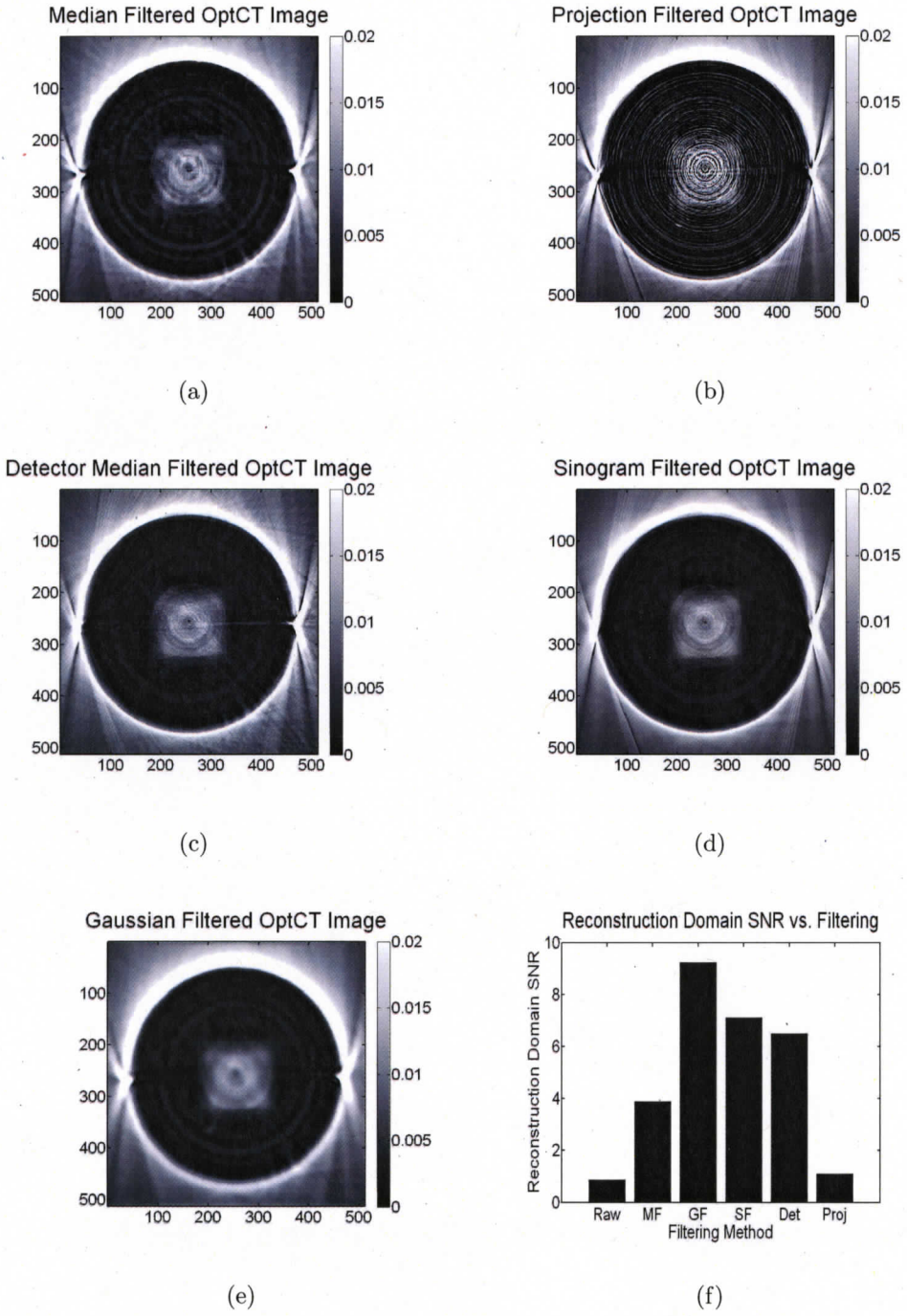

Figure 5.2: OptCT image of 3 by 3 cm^2 gel at 3 cm depth processed using (a) 10 $\times$ 10 median filter in the spatial domain, (b) groups of 10 individual projection angles median filtered together pre-reconstruction, (c) groups of 10 individual detector absorbance values median filtered together pre-reconstruction (d) sinogram data median filtered in two-dimensions over a 10 $\times$ 10 pixel neighbourhood pre-reconstruction (d) Gaussian filter in the frequency domain with a standard deviation of σ=15. (f) SNR as a function of different image enhancement techniques employed.

step is illustrated in figure 5.2(d).

A final filtering procedure was applied to the Fourier transform of the image in the frequency domain. It used a two-dimensional, Gaussian convolution operator with a standard deviation of the $\sigma = 15$. The standard deviation of the Gaussian operator indicates which range of spatial frequencies are removed from the image in processing. Figure 5.2(e) indicates the result of applying this filter to an image of the NIPAM gel irradiated with 3×3 cm^2 field at 3 cm depth. The improvement in image SNR as a result of each of the filtering operations is identified in figure 5.2(f). The image that was smoothed using the Gaussian filter registered the highest SNR at a value of 9.23. Expressed another way, the noise still existing in the image contributed, on average, to 10.8% of the signal. Ideally, to meet the RTAP criteria [40], this figure should be 3%. Loss of spatial resolution is more pronounced with Gaussian filtering, compared to median filtering of the sinogram or median filtering of the detector absorbance values. When median filtering of the sinogram was used, an SNR of 7.11 was achieved; when median filtering of the detector absorbance was used, an SNR of 6.51 was obtained. As well, both median filtering techniques improved the contrast resolution over the Gaussian, frequency domain filtering method.

In summary, because the sinogram median filtering method (using a 10×10 pixel mask on the sinogram data pre-reconstruction) and the Gaussian, frequency domain, filtering technique were the most efficient in raising the reconstruction domain SNR of the OptCT images, they were employed for the remaining dosimetry verification comparisons between OptCT and Eclipse.

5.1.3 Conversion of OptCT Attenuation Images to Dose Images

Before dosimetry verification was performed, the optical attenuation image measured for the 3×3 cm^2 gel was converted to a dose image, using a linear conversion from optical density to dose. A dose calibration curve, as illustrated in figure 5.3(b), was generated independently for each dosimetry experiment by determining the average

optical density in a homogeneously irradiated region of the gel image at 1.5 cm depth (figure. 5.3(a)). A depth of 1.5 cm was chosen because this is the depth where the maximum dose is typically deposited for a 6 MV photon beam [5]. This value was then assigned the maximum dose in the corresponding Eclipse treatment plan. In this manner, a single point was generated on a plot of dose(Gy) as a function of optical attenuation coefficient. Other points were linearly interpolated from this value.

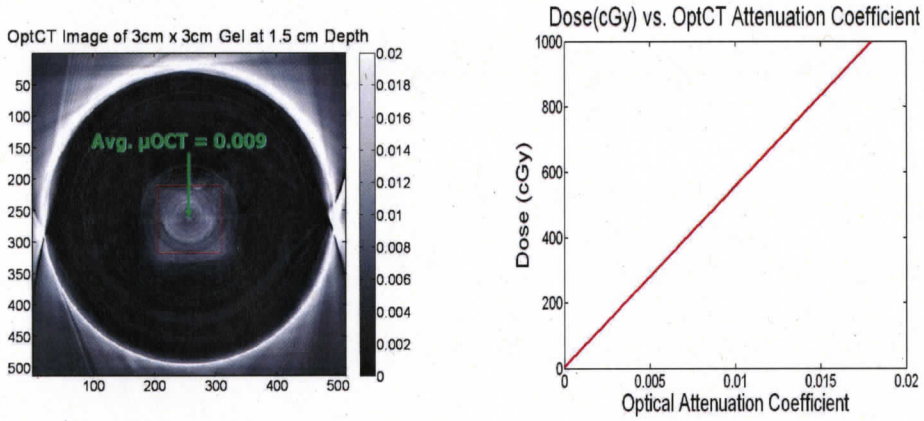

(a) (b)

Figure 5.3: Conversion of optical attenuation coefficients to dose: (a) average optical attenuation coefficient in the 3×3 cm^2 square region (0.009) of the irradiated gel at a depth of 1.5 cm, (b) calibration plot for linear conversion of optical density to dose.

5.1.4 Comparison of OptCT and Eclipse Dose Planes

After converting optical attenuation to dose, OptCT dose was compared to the modeled dose distribution from a commissioned Eclipse treatment planning system. Dose profiles of Eclipse, Gaussian filtered ($\sigma = 15$) and 10×10 sinogram median filtered OptCT images in the x-direction, through a y-pixel value of 278, are plotted in figure 5.4(a). The magnitude of dose for all profiles was normalized to the maximum dose in the Eclipse plan at a depth of 3 cm. The sharp dose gradient, penumbral regions of the x-dose profile indicate a 1-4% dose difference between Eclipse and both sinogram and Gaussian filtered OptCT profiles. The central, 2.4 cm, low dose gradi-

ent region shows an average dose difference of 6% between Eclipse and both sinogram and Gaussian filtered OptCT images. The general shape of the OptCT dose profiles through the irradiated region matches Eclipse. Aside from the noise in the low dose gradient region, the primary difference between Eclipse and OptCT profiles from figure 5.4(a) is indicated by the slightly sharper roll-off in dose in the OptCT profiles at the edge of the field. Because the Eclipse system is known to poorly model small field geometries, it is possible that OptCT is more accurate in depicting the penumbral region of the field in this profile.

Dose difference profiles for the same OptCT image in the y-direction are presented in figure 5.4(b). These profiles were taken through an x-pixel value of 278. Again, dose difference in the sharp dose gradient, penumbral regions of the profile is in the 1-4% range. On average, dose difference in the low dose gradient, central region of the field is 6% between Eclipse and Gaussian filtered OptCT and 8% between Eclipse and sinogram filtered OptCT. The penumbral region on the right side of the field is matched more accurately to Eclipse than the left side of the field in the vicinity of -1.7 cm on the x-axis. Nonetheless, the irradiated region defined in the OptCT dose profile matches that defined by Eclipse. To compare the Eclipse and OptCT dose distributions accurately, the Eclipse dose plane which has a pre-defined spatial resolution of 2.5 mm/pixel was upsampled to match the OptCT dose plane spatial resolution of 0.25 mm/pixel. A two-dimensional, linear interpolation in Matlab was used to upsample the Eclipse dose matrix.

A complete dose difference image was obtained by subtracting the Eclipse dose plane at 3 cm depth from the corresponding OptCT sinogram filtered dose image. The dose difference image is displayed in figure 5.4(d). The magnitude of each pixel is scaled by the value of the maximum dose in the Eclipse treatment plan at 3 cm. Consequently, the image identifies fractional dose difference between OptCT and Eclipse at every point on a 512 $\times$ 512 image matrix. The average dose difference

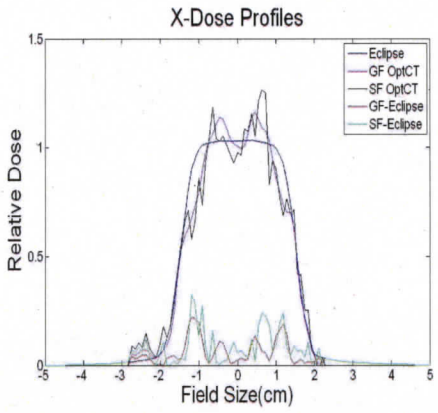

(a)

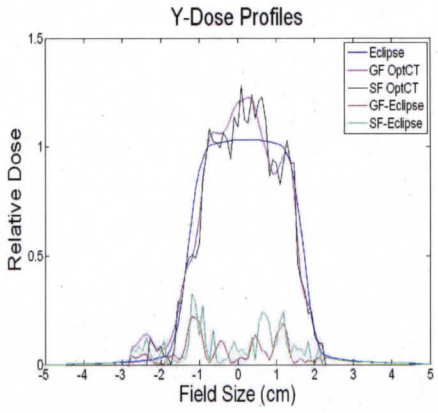

(b)

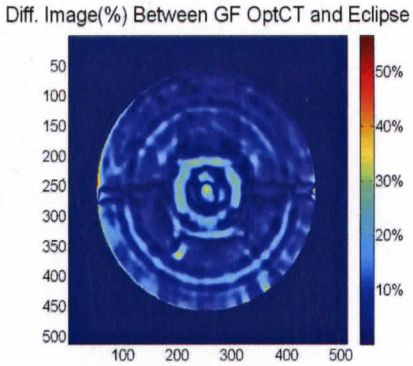

(c)

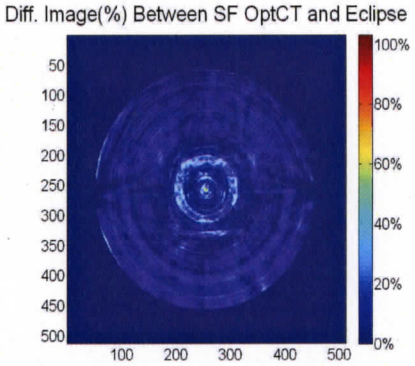

(d)

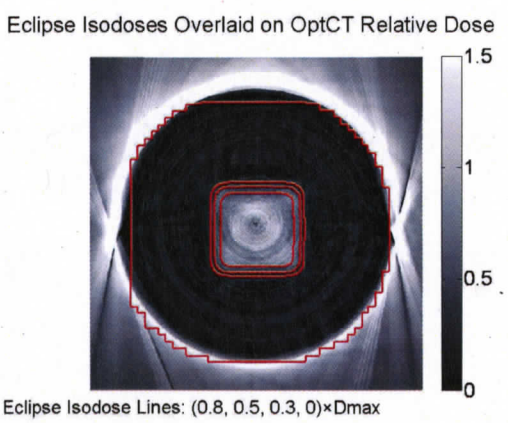

(e)

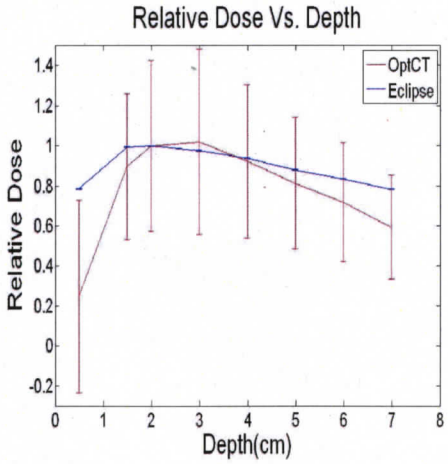

(f)

Figure 5.4: Comparison of OptCT and Eclipse 3 × 3 cm^2 gel dose at a depth of 3 cm using (a) x-dose profiles, (b) y-dose profiles, (c) dose difference between Eclipse and OptCT Gaussian filtered images, (d) dose difference between Eclipse and OptCT 10 × 10 sinogram median filtered images, (e) percent depth dose, (f) isodose overlays.

between Eclipse and sinogram filtered OptCT in a 1.75 cm square around the center of the image is 11.3%. However, dose differences as low as 1 - 2% are also seen in the center square. Additionally, figure 5.4(d) indicates evidence of the sharper fall-off of OptCT dose in the penumbral region compared to Eclipse. A similar dose difference image obtained by subtracting the Eclipse dose from the Gaussian filtered OptCT dose image is illustrated in figure 5.4(c). The average dose difference between Eclipse and Gaussian filtered OptCT in a 1.75 cm square around the center of the image was 8.42%. Notably, rings in the dose difference images contributed to a dose difference increase of 2-6%.

Although the RTAP criteria for dosimetric accuracy [40] of 3% was not met in the bulk of the irradiated region of the 3×3 cm^2 irradiated gel at 3 cm depth, the sample regions of the x- and y-dose profiles identified dose difference values as low as 1-2%. As well, the matching of the dose profiles in the penumbral region showed dose differences of 1-4%. Essentially, the 2-6% dose difference contribution of the ring artefact noise represents the main impediment to accurate OptCT dosimetry.

Figure 5.4(e) presents Eclipse isodose curves for the 3×3 cm^2 irradiated gel at 3 cm depth overlaid on an OptCT, gray-scale dose map. The magnitude of dose in the OptCT image is scaled by the the maximum dose in the Eclipse treatment plan at 3 cm. Eclipse isodose lines denoting 80%, 50%, 30% and 0% of the maximum dose in the Eclipse slice are overlaid on the OptCT image. This image was used to verify that the Eclipse dose image was accurately aligned with the OptCT image, after being upsampled in order to perform dosimetric comparisons. The overlay demonstrates that upsampling the Eclipse image was accurate, since the 0% Eclipse isodose line is overlaid on the gel cylinder wall and the central 80%, 50%, 30% Eclipse isodoses are aligned with the OptCT image polymerized region.

A major advantage of polymer gel dosimetry is its ability to measure multiple dose planes simultaneously and compare areas at different depths in a phantom material.

A measure often used to compare dose at different depths in radiotherapy is a percent depth dose curve. Such a curve measures the dose deposited at varying depths in a medium along the central axis of the radiotherapy beam. It is particularly relevant for planning and commissioning in classical radiotherapy treatment. The Eclipse system uses measured percent depth dose data from an ion chamber measurement for computational dose modeling. A plot of OptCT dose as a function of depth for the 3×3 cm^2 field, NIPAM gel is given in figure 5.4(f). For comparison, the percent depth dose curve is overlaid onto the Eclipse treatment planning system curve. The data is normalized to the Eclipse maximum dose at 1.5 cm for this treatment. OptCT dose values at each depth were found to be accurate to within an average of 7% of the Eclipse values.

5.2 Four-Field Box Irradiation

The second dosimetry verification experiment involved a four-field box treatment plan (6 MV photons, SSD = 98.5 cm) delivered using a 60^o wedge along the longitudinal axis of the treatment beam. This plan was developed to deliver 500 cGy to the isocenter, located at 5 cm depth from the top of the container. The gel phantom used consisted of 500 mL of NIPAM gel in a smaller, Barex "coffee-cup" container. The experiment was designed to investigate: (1) steep dose gradients in the axial plane of the OCT dose distribution, (2) moderate dose gradients in the z-axis of the three-dimensional dosimeter volume and (3) fields which impinged axially through the side of the gel container.

5.2.1 OptCT Optical Attenuation Images

The calibration and transmission data sets collected for the four-field box gel were acquired using the same technique described in the previous section. Calibration data from figure 5.5(a) was employed to ensure that a reasonably homogeneous level of light was hitting all detectors. The transmission test scan in figure 5.5(b) indicates

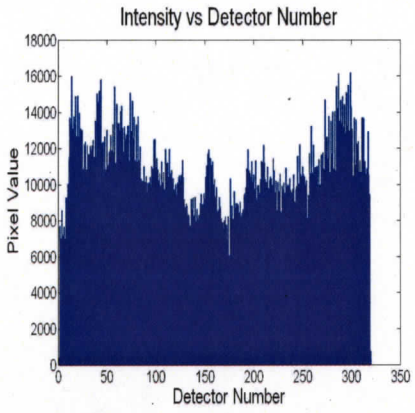

(a)

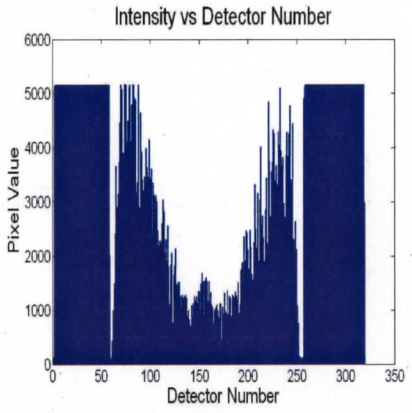

(b)

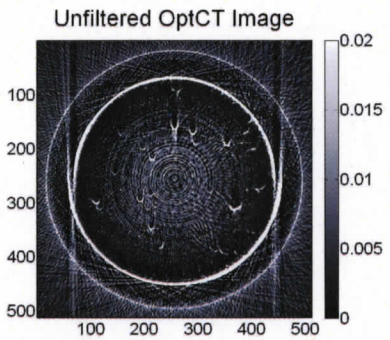

(c)

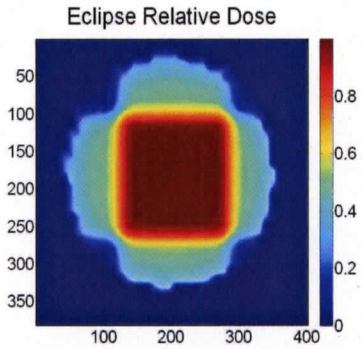

(d)

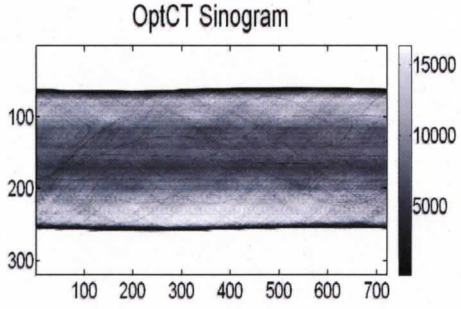

(e)

Figure 5.5: For the four-field box gel: (a) single calibration acquisition, (b) single transmission acquisition (c) raw, reconstructed OptCT image, (d) Eclipse relative dose, (e) sinogram data.

only a small region of data loss at the container edge. Unlike the larger, cylindrical Barex container used with the 3 × 3 cm^2 gel documented in the previous section, the 500 mL "coffee-cup" container utilized in this experiment did not have grooves running down opposing sides of the container. The grooves caused light rays to refract at the cylinder wall and produced faint artefacts when imaging the 1 L Barex cylinder. These artefacts were not apparent when imaging the 500 mL "coffee-cup" container.

The raw reconstructed OptCT image of the four-field box irradiation arrangement delivered to the gel is shown in figure 5.5(c). The four beams used to deliver the treatment were 4.5 cm in width in the x direction. The planned, square dose distribution is reproduced in the axial image of figure 5.5(c). In addition, the optical attenuation recorded in the gel is linearly proportional to the dose delivered to the gel. However, "cupping" artefacts (white cup-shaped regions of notably high optical attenuation) are seen in the image. These were likely caused by refraction or scatter of the fan beam rays at these these points. As previously discussed, refraction and scatter result in some detectors recording significantly higher intensity values than others. When the image was calculated, this uneven distribution of light likely resulted in high optical attenuation, "cupping" artefacts in the images.

The presence of ring artefacts 2-4 pixels in line width still appeared in the raw reconstructed image, while optical attenuation pixel values near the edge of the gel cylinder only faintly display polymerization where the beams entered axially through the side of the container. This indicates: (1) either physically meaningful information was lost from the transmission data due to refraction or scatter of light close to the wall of the cylinder or (2) the gel under-polymerized in this region. The sinogram in figure 5.5(e) indicates no evidence of either faulty detector pixels or a single projection angle with an extremely high intensity value.

5.2.2 Filtered OptCT Images

The relative effectiveness of each of the processing methods on raw OptCT images of four-field gel is identified in figure 5.6(b). The greatest noise reduction was again achieved with Gaussian smoothing ($\sigma = 15$) at the expense of loss in spatial resolution. The Gaussian filtered image had a reconstruction domain signal-to-noise ratio (SNR) of 9.71. Alternatively, the noise contributed to 10.2% of the signal in the irradiated region of the gel. Although the reconstruction domain SNR of the sinogram-median-filtered image (SNR = 7.79) and the 1D absorbance-filtered image (SNR = 7.48) were again slightly lower, the image contrast resolution was improved.

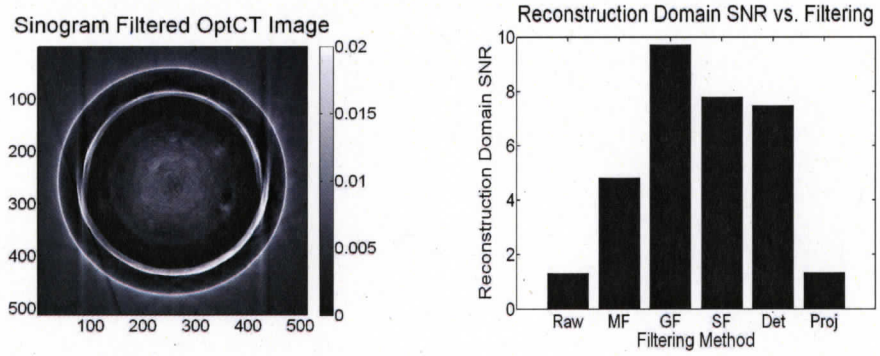

(a) (b)

Figure 5.6: OptCT image of the four-field gel post-processed using (a) sinogram data median filtered in two-dimensions over a 10 × 10 pixel neighbourhood pre-reconstruction. (b) SNR as a function of different image processing techniques employed.

5.2.3 Comparison of OptCT and Eclipse Dose Planes

To verify the dosimetric accuracy of the four-field OptCT image, an OptCT reconstructed dose plane of this gel at isocenter (5 cm depth from the top of the container) was compared to the calculated dose from the Eclipse treatment planning system. A dose profile comparison in the x-direction through a y-pixel value of 235 is displayed in figure 5.7(a). The profiles were normalized to the maximum dose in the Eclipse plan at isocenter. The average dose difference between Eclipse and Gaussian

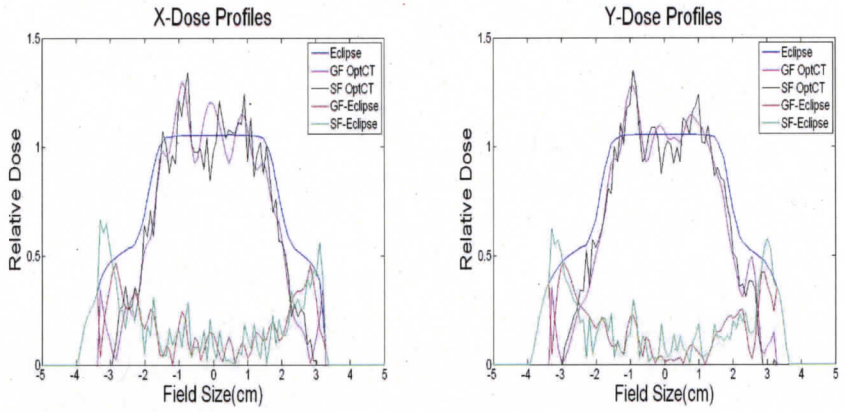

(a)

(b)

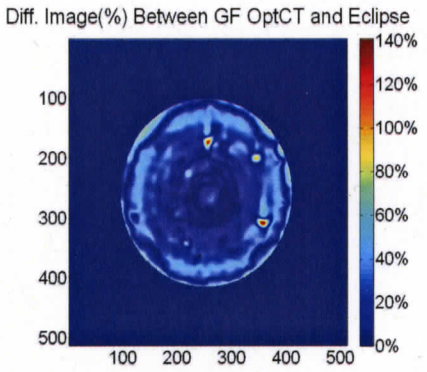

(c)

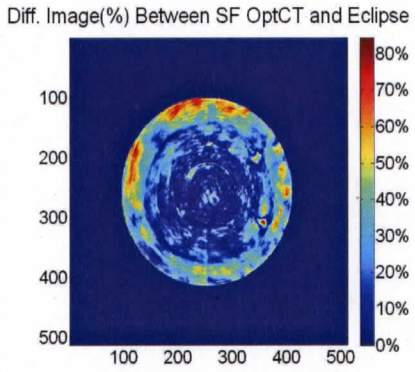

(d)

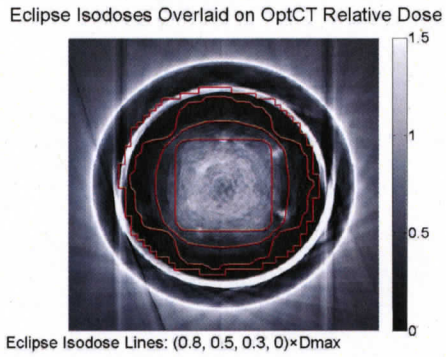

(e)

Figure 5.7: Comparison of filtered OptCT and Eclipse using (a) x-direction dose profiles, (b) y-direction dose profiles, (c) dose difference image between Eclipse and OptCT Gaussian filtered image, (d) dose difference between Eclipse and OptCT 10 × 10 sinogram median filtered, (e) isodose overlays

filtered OptCT image was 16.5% over the central, 4 cm, low dose gradient region of the dose profile, while the dose difference between Eclipse and sinogram filtered OptCT was 16.3% in the same region. A similar trend was evident in the y-direction profile (figure 5.7(b), with the average dose difference between Eclipse and Gaussian filtered OptCT reaching 15.3% and the difference between Eclipse and sinogram filtered OptCT recorded at 17.2%. The central, 4 cm irradiated box was recorded accurately in both the x- and y- dose profiles, while the slope of the OptCT penumbral regions matched that of Eclipse. However, the image indicates no dose deposited by the four, orthogonal radiation beams entering through the sides of the gel container. This may be due to either a loss of the transmission signal near the wall of the container or incomplete polymerization of monomer and co-monomer near the edges of the gel cylinder.

Dose difference images obtained by subtracting the Eclipse four-field box dose plane at 5 cm depth from the corresponding OptCT filtered dose planes are illustrated in figure 5.7(c) and figure 5.7(d). The magnitude of each pixel is scaled by the value of the maximum dose in the Eclipse treatment plan. Consequently, the images show fractional dose difference between OptCT and Eclipse. The average dose difference between Eclipse and Gaussian filtered OptCT dose in a 1.5 cm square around the center of the image was 8.9%. Dose difference between sinogram filtered OptCT and Eclipse for the same 1.5 cm square was 11.2%. For the full, 4.5 cm, central box region, excluding the penumbra, the dose difference between Eclipse and OptCT was 18.1% for sinogram filtered OptCT and 19.6% for Gaussian filtered images.

It appears an image artefact was introduced when reconstructing slices of this gel. Small semi-circles of high optical attenuation appear at the edge of the irradiated 4.5 cm box where light may have refracted significantly in passing from the irradiated portion of the dosimeter to the backround gelatin.

Eclipse isodose curves overlaid on an OptCT, gray-scale dose map are presented in

Figure 5.7(e). The magnitude of dose in the OptCT image is scaled by the maximum dose in the Eclipse treatment plan. Eclipse isodose lines are registered for 80%, 50%, 30% and 0% of the maximum dose in the Eclipse slice. As in the previous verification experiment, the 0% isodose line is overlaid on the gel cylinder wall and the central 80%, 50%, 30% isodoses are aligned with the OptCT irradiated region. This signifies accurate alignment of OptCT and Eclipse for performing dosimetric comparisons.

5.3 Seven-Field IMRT Irradiation

The final dosimetry verification experiment consisted of a seven-field intensity modulated radiation therapy (IMRT) plan delivered with a prescription dose of 6 Gy to a ring-shaped target structure. Both the geometric arrangement and monitor unit settings delivered for this treatment are documented in chapter three. The ring-shaped, PTV of approximately 7.93 cm diameter was contoured on CT slices and a central 1.75 cm diameter circle was labeled as an organ-at-risk (OAR). Consequently, one goal of the treatment was to minimize dose to the central OAR circle. The irradiation pattern was delivered to one litre of NIPAM gel in the large Barex container at a depth of 2.5 cm from the top rim. The central focus of this experiment was to investigate more complex dosimetry protocols with intensity-modulated fields.

5.3.1 OptCT Optical Attenuation Images

Calibration data collected with no dosimeter in place for this experiment is shown in figure 5.8(a) and demonstrates reasonable detector homogeneity across the arrays. The local dip in intensity at the centre of the calibration histogram can be attributed to refraction of the associated light rays by a small angle in the z-direction. Such an intensity dip can be compensated for by a slight movement of the lens either towards or away from the aperture of the matching tank. However, if this effect is inherent in both the calibration and transmission data, application of the Beer's law pre-processing step will compensate for it. The transmission data for the IMRT gel

scan, figure 5.8(b), illustrates that the IMRT gel exploits the full dynamic range of the detector pixel values. From the transmission projection data, the attenuating ring structure is visible from the two dips in intensity at the center of the histogram. These represent the two sides of the ring. As was the case for the 3×3 cm^2 field gel, transmission data is lost from detectors 34-49 and 266-282 on either side of the Barex cylinder due to refraction away from the corresponding detectors.

The raw, reconstructed OptCT image of the seven-field IMRT gel is presented in figure 5.8(c). The entrance fields are visible at the edge of the dosimeter volume, while the ring structure planned in Eclipse in figure 5.8(d) is seen in the polymerized region of the gel. The central region inside the irradiated circle where the OAR was placed in the plan has received little dose. The sinogram in figure 5.8(e) also indicates no evidence of any detector pixels with large and varying values or projection angles with sharp discontinuities from the rest of the data set. In addition, the variable attenuation from the ring structure of the irradiated gel can be seen along the center of the sinogram.

5.3.2 Filtered OptCT Images

Using the previously established definition of SNR as the ratio of the mean pixel value to the standard deviation in pixel value in the polymerized region of the gel image, processed images of the seven-field, IMRT gel are quantitatively compared for accuracy in the histogram of figure 5.9(b). The greatest improvement in noise reduction is achieved with Gaussian smoothing ($\sigma = 15$). This image has a reconstruction domain SNR of 7.59 (noise contributes to 22.3% of the signal in the irradiated region of the gel). The reconstruction domain SNR of the sinogram-median-filtered image (SNR = 6.44) and the 1D absorbance-filtered image (SNR = 6.66) are lower. However, the contrast resolution of these images is increased.

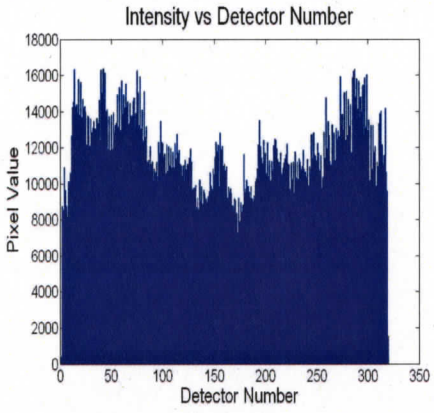

(a)

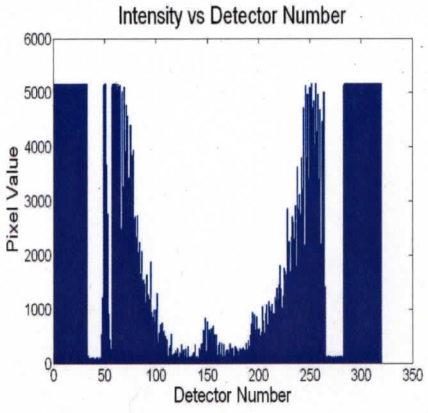

(b)

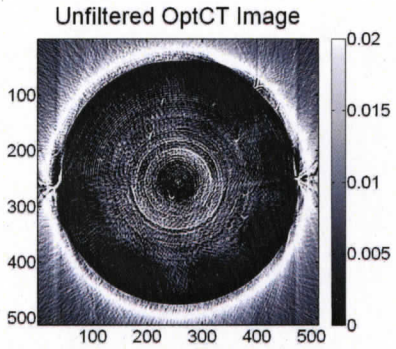

(c)

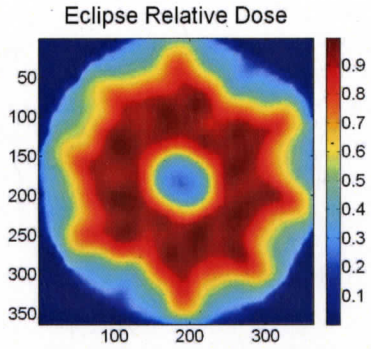

(d)

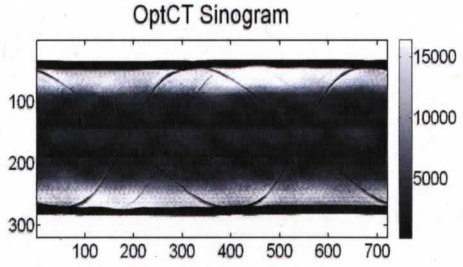

(e)

Figure 5.8: For the seven-field, IMRT gel: (a) single calibration acquisition, (b) single transmission acquisition, (c) raw, reconstructed OptCT image, (d) Eclipse relative dose, (e) sinogram data.

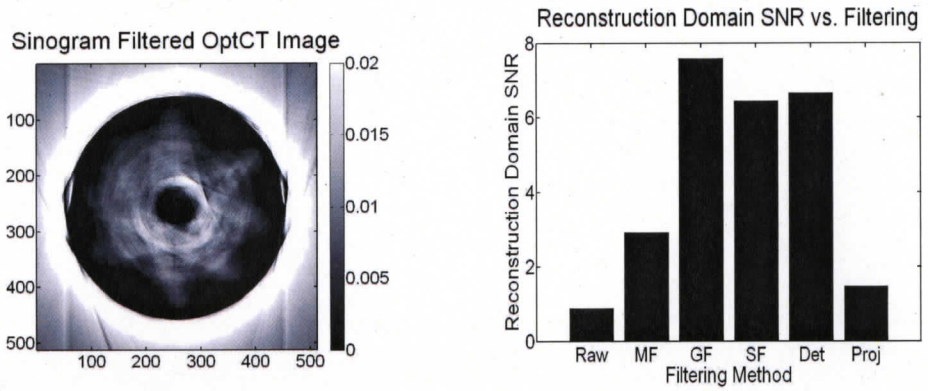

(a) (b)

Figure 5.9: OptCT image of the seven-field IMRT gel processed using (a) sinogram data median filtered in two-dimensions over a 10 × 10 pixel neighbourhood pre-reconstruction. (b) SNR as a function of different image processing techniques employed.

5.3.3 Comparison of OptCT and Eclipse Dose Planes

A dose profile comparison in the x-direction through a y-pixel value of 400 is presented in figure 5.10(a). Due to the complexity of the seven-field irradiation, only the sinogram filtered OptCT dose was compared to Eclipse for this experiment. The profiles were normalized to the maximum dose in the Eclipse plan at isocenter. The average dose difference between Eclipse and the sinogram filtered OptCT image profile was 4.4% in the central 5 cm section of this profile and 8.6% at the penumbral edges. The large rise in the OptCT dose profile at the edge of the field denotes the wall of the gel cylinder and has no dosimetric significance. The y-direction profile in figure 5.10(b) was taken through an x-pixel value of 400. The average dose difference between Eclipse and the sinogram filtered OptCT was 8.1% in the central region of the profile and 10.9% at the penumbral edges. The wall of the gel cylinder again results in a large apparent increase in OptCT dose at the edge of the field. However, this is not relevant for dosimetry verification.

A dose difference image was obtained by subtracting the Eclipse dose plane at

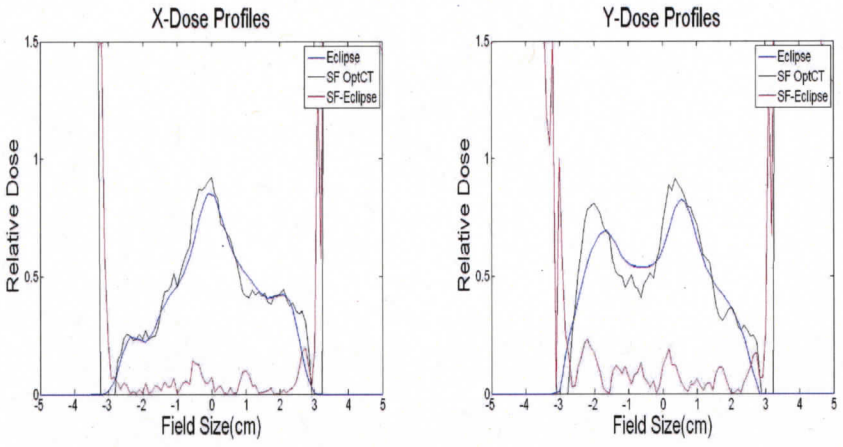

(a)

(b)

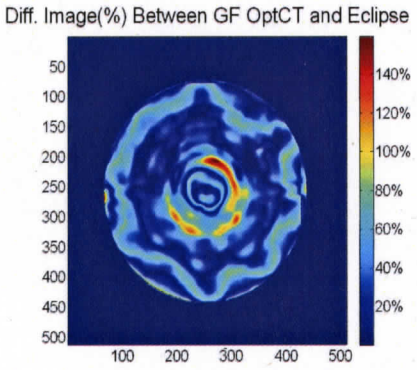

(c)

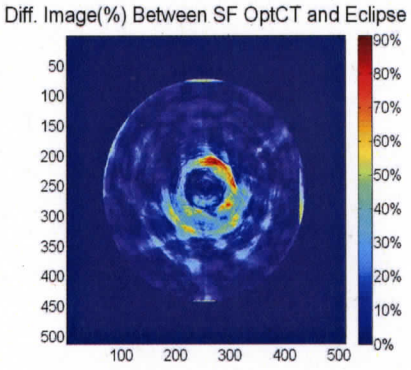

(d)

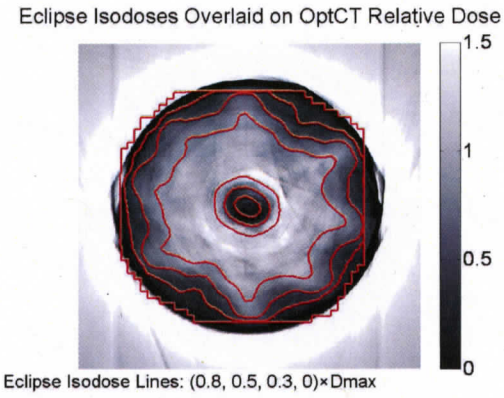

(e)

Figure 5.10: Comparison of filtered OptCT and Eclipse images of the seven-field IMRT irradiation using (a) x-dose profiles, (b) y-dose profiles, (c) dose difference image between Eclipse and OptCT Gaussian filtered image, (d) dose difference between Eclipse and OptCT 10×10 sinogram median filtered, (e) isodose overlays.

isocenter from the corresponding OptCT filtered dose. Figure 5.10(d) illustrates the two-dimensional dose difference between Eclipse and sinogram filtered OptCT. The magnitude of each pixel is scaled to the maximum dose in the Eclipse treatment at 2.5 cm depth. A rectangle 2.2 cm in width and 1.1 cm in height was defined over pixels 138-226 (x-direction) and 300-344 (y-direction) in the dose difference image to calculate an average measure of dosimetric agreement between the two planes. The average dose difference between Eclipse and sinogram filtered OptCT in this rectangular area of the image was 6.7%.

The dose difference image between Eclipse and Gaussian filtered OptCT is displayed in figure 5.10(c). The average dose difference between Eclipse and Gaussian filtered OptCT dose in the 2.2 cm by 1.1 cm rectangle was higher than 20%. The Gaussian frequency domain, processing method resulted in unwanted effects at the edges of the dose distribution for this OptCT map. Specifically, the high frequency components of the image at the edge of the IMRT dose distribution where dose values drop-off sharply, have been removed from the OptCT image using the filtering operation. This suggests that sinogram median filtering, detector filtering or Gaussian filtering using a convolution factor with a σ value greater than 15 (to allow lower spatial frequencies to be represented in the image) is necessary to perform fan beam OptCT dosimetry for a complex seven-field case.

Dose difference is greatest in both images near the perimeter of the gel cylinder and at the upper right portion of the inner ring. The edge effect resulting from refractive loss of fan beam transmission data near the cylinder walls may have contributed to the 0.45 mm loss of dose data in the OptCT image at each of the entrance fields. Optical attenuation coefficient values between 0.02 and 0.03 (comparatively high values) have been converted to doses larger than the maximum prescribed dose of 600 cGy on the upper right portion of the inner part of the ring structure. Such large attenuation coefficients were likely calculated in the reconstructed OptCT image because of an

unusually high density of scattering micro-particles in this region of the gel matrix.

Eclipse 80%, 50%, 30% and 0% isodose curves are overlaid on an OptCT, gray-scale dose map in figure 5.10(e). The magnitude of dose in the OptCT image is scaled by the the maximum dose in the Eclipse treatment plan. The 0% Eclipse isodose line coincides well with the cylinder wall. Moreover, the entrance fields modeled by the Eclipse system are seen in the OptCT gel image. Additionally, a low dose, 1.75 cm central circle exists in the OptCT distribution, where the image has correctly reconstructed a zone of sparing for the organ-at-risk, as predicted by the Eclipse plan. Lastly, the accuracy of the overlaid isodose lines signifies that accurate alignment of OptCT and Eclipse was established when performing the dose difference comparisons highlighted in the previous paragraphs [13].

Chapter 6

Conclusions

6.1 Conclusions

A prototype fan beam OptCT scanner has been designed, constructed, characterized and tested with preliminary gel dosimetry protocols. The overall goal in system design and implementation was to satisfy the RTAP criteria (spatial resolution of $1\times1\times1$ mm^3, imaging time of 60 minutes, dose accuracy within 3% and precision within 1%) [40].

The scanner uses a number of design features new to OptCT dosimeter readout technology. Specifically, the light source for the system is a 60^o fan of 543 nm, green laser light subtended from a line generating lens. The fan beam source allows for collection of transmitted intensity values through a single slice of the dosimeter without the need of translation of a single, linear laser beam. Such a fan beam source also results in reduced scattered light intensity from out-of-plane slices. Further, when combined with the translational and rotational stages and the micro-controller software of the system, the fan beam allows scanning of cross-sections up to 19 cm in diameter in 2-4 minutes. For full volumetric scanning, dosimeters 10 cm in height can be scanned in three hours and 20 minutes, using one signal acquisition per angle over a total of 360 projection angles in a reconstructed slice. Although such a scan time is two hours and 20 minutes above the RTAP limit of 60 minutes suggested by

Oldham [40], it accomodates a reasonably-sized, 10 cm dosimeter volume with a full set of 360 projection angles.

The central focus of this research was not speed, but rather the most accurate measurement of optical attenuation coefficients possible in the 3D dosimeter volume. As was previously indicated, a large fraction of the total scan time for a single slice is spent running the Matlab-based data acquisition code on the PC. Further optimization of the system software in C++ is underway to reduce scanning time. Previous experience with the software suggests it can be substantially accelerated. The matching medium tank, containing the 1 L glycerol/3 L de-ionized water matching solution which the dosimeter is immersed in, was specifically constructed so the incident rays of the fan beam would strike the front and back walls at perpendicular incidence, thus minimizing refraction at each interface. The homogeneity of calibration scan intensity histograms indicates the combination of tank and matching solution was successful in reducing the effects of refraction for the fan beam of laser light passing through the scanner apparatus. As well, the custom built, CNC-machined, acrylic collimator rejected scattered radiation accepted by the detector arrays by up to 13%. The addition of this collimation proved to quantitatively increase the accuracy of the projection data transmission profiles. The results of the image processing operations applied to the raw images in this study suggest that one source of ring artefact noise in reconstructed images may be inter-detector intensity variation. The rings, on average 2-4 pixels in line-width in the reconstructed images, represent the most significant impediment to accurate optical metrology and dosimetric verification with the OptCT system.

Characterization procedures for the scanner were performed to benchmark the temporal stability of the laser light source, the variation in detector pixel value as a function of number of acquisitions, the axial spatial resolution of the OptCT system, the absorbance dynamic range of the scanner and the ideal scan parameters.

After one hour, the detector intensity was constant to within 0.7% of of the mean for all detectors. This constant temporal laser stability is essential for accurate optical imaging as fluctuations in laser output power cause concomitant variations in reconstructed optical attenuation coefficients. The absorbance dynamic range of the scanner of 1.7 is comparable to state-of-the art scanners in the field [43].

Calibration scans through the matching solution and transmission scans through the 3×3 cm^2 irradiated dosimeter identified a standard error in pixel value of 0.34% for calibration scans and a standard error of 0.62% for transmission scans. Further, the OptCT scanner is capable of 0.25 $\frac{mm}{lp}$ spatial resolution in the axial plane of the transmission scan, dictated by the 30% value of the modulation transfer function. Additionally, a 0.8 mm spatial resolution was achieved on the z-axis of the three-dimensional dosimeter volume, as defined by the detector element height in each array. Geometric distortion was found to be negligible when a matching solution of refractive index 1.35, consisting of 1 L of glycerol and 3 L of water, was used.

Three dosimetry verification experiments were conducted to test the dosimetric accuracy and spatial agreement between the fan beam OptCT calculated dose and the theoretically calculated dose from the Eclipse treatment planning system. To reduce the effects of ring artefacts in the raw OptCT images, comparisons were carried out between Eclipse and OptCT images filtered in the sinogram space with a 10×10 pixel median filter, as well as between Eclipse and Gaussian filtered OptCT images.

The first dosimetry verification experiment investigated a single 3×3 cm^2 photon beam delivered to 1 L of NIPAM gel in a cylindrical Barex container. This experiment examined small field and steep dose gradient dosimetry. The shape of both x- and y- OptCT dose profiles matched well with Eclipse modeled dose distribution data. X-dose profiles showed a 1-4% dose difference in the penumbral region of the 3×3 cm^2 field and a 6% difference between Eclipse and OptCT in the central, 2.4 cm wide, low dose gradient region. Similar results were obtained for the y-dose profile.

The higher dose difference value in the low dose gradient region due to noise from the ring artefacts was the principal impediment to accurate dosimetric matching of the profiles. Multiple slices through the 3×3 cm^2 gel were used to record a central axis percent depth dose curve from Gaussian filtered and sinogram filtered OptCT images. On average, the OptCT dose at each depth on the percent depth dose curve was accurate to within 7% of the Eclipse data.

A second verification experiment evaluated dosimetric and spatial agreement between OptCT and Eclipse for a four-field box treatment with a 60^o wedge along the longitudinal axis, (6 MV photons, SSD = 96.5 cm). This case examined steep dose gradients in the axial plane of the OptCT dose distribution, moderate dose gradients in the z-axis of the three-dimensional dosimeter volume, as well as fields which impinge axially through the side of the container. Subtraction images between OptCT and Eclipse revealed 8-11% difference in the central 1.5 cm square region inside the four-field box area. The entrance fields through the side of the gel container were not accurately preserved within one centimeter of the edge of the cylinder wall in this experiment. This indicated either that data was lost in the vicinity of the wall due to refraction or that under-polymerization of the monomer and co-monomer species occurred in this region.

The final experiment involved a seven-field intensity modulated irradiation of a 1 L volume of NIPAM gel in a Barex cylinder. For this complex irradiation, the entrance fields modeled by the Eclipse system were accurately recorded in the OptCT gel image. Additionally, a low dose, 1.75 cm central circle was preserved in the OptCT distribution where the image correctly reconstructed a zone of sparing for the planned organ-at-risk. Dosimetric comparison between sinogram filtered OptCT and Eclipse through x- and y- pixel values of 400 revealed a 4.4% average dose difference in the x-dose profile and an 8.1% average dose difference in the y-dose profile. Because the IMRT experiment was performed with the gel housed in the

more optically transparent Barex cylinder, the resultant images show that, with the exception of ring noise, artefacts were suppressed and the complex spatial pattern deposited by the IMRT fields was accurately measured in the NIPAM gel.

In summary, while still in the prototypical stage, the fan beam OptCT scanner has provided promising initial images of reconstructed optical attenuation coefficients. Its spatial resolution of 0.25 $\frac{mm}{lp}$ (MTF value at 30%) in the plane of the scan satisfied the RTAP criteria, as did the spatial resolution of 0.8 mm in the z-direction (defined by the detector height). Moreover, the precision of the scanner in the projection domain for static calibration (0.62%) and transmission (0.34%) scans met the RTAP precision criteria of 1%. Precision of scanning in the reconstruction domain remains an area for current research. The RTAP scanning time criteria was met for dosimeter cylinders less than 6.7 cm in height with one signal acquisition per angle over a total of 360 projection angles. However, the dosimetric accuracy, nominally 7% in low dose gradient regions and 5% on the field edges, constitutes the most significant area for further quantitative analysis. Perhaps the two chief limitations to the scanner are the noise in dose profiles from ring artefacts and the loss of dosimetric information near the edge of the gel cylinder. Sinogram median filtering using a 10 $\times$ 10 pixel neighbourhood and Gaussian filtering with a standard deviation of 15 $\frac{lp}{mm}$ were shown to be strong but temporary solutions for removing outlying low attenuation values caused by ring artefacts. Nonetheless, the physical basis for the ring artefacts has been investigated in this study and the results may facilitate future refinement of the scanner.

6.2 Directions for Future Research

Several elaborations to the basic prototype scanner and collimator outlined in this study could prove useful. First, the current collimator thickness of 1.5 cm was optimized at the outset of this research, based on central axis scatter fraction tests

performed with varying thicknesses of tertiary collimation. With the final tertiary collimation in place, a 13% reduction was observed. However, the increased intensity variation between detector pixels associated with the collimation was not anticipated. Accordingly, further experimentation investigating the incidence of ring artefacts with different tertiary collimation thicknesses would likely prove useful. More specifically, a set of full collimators which attach directly to all detectors could be constructed to identify the magnitude of ring artefacts, the quantitative transmission profile intensity changes and the scatter rejection with varying thicknesses of collimation.

A second area for future research could focus on improving scanning time with optimization of the projection data collection code in C++. As previously stated, this study focused on accurate optical metrology. Care was taken to write software that provided consistent, accurate projection data collection without truncating the data because of limitations with the data transfer rate from the micro-controller to the PC. The fan beam scanning geometry allows for implementation of continuous rotation of the dosimeter in a single slice during projection data collection (rather than stopping at each projection) in order to significantly improve scan times.

Further directions for advancing the scanning properties of the OptCT system could include: (1) optimizing the system to allow for dual scanning of both light scattering polymer gels and light absorbing polyurethane plastics. The two 3D dosimeter options may provide different advantages for dose readout of different treatments. (2) further developing the scanner to allow scanning of non-symmetrical phantom geometries. Such a refinement would require both adjusting the reconstruction algorithm and compensating for any new refraction effects due to the introduction of a non-symmetrical dosimeter geometry.

Lastly, a wide variety of current and possible future research avenues exist where fan beam OptCT readout of 3D dosimeters could be applied, including experimental verification of such treatments as arc, tomotherapy, heavy ion therapy and micro-

beam radiation therapy. Additionally, the preliminary dose verification of this study indicates three-dimensional dosimetry could prove useful for verifying regions of dose distributions which are poorly calculated by a software planning system.

Bibliography

[1] J. Van Dyk. *The Modern Technology of Radiation Oncology: A Compendium for Medical Physicists and Radiation Oncologists.* Medical Physics Publishing, Madison, Wisconsin, 1999.

[2] P. Hoban, T. Kron and P. Metcalfe. *The Physics of Radiotherapy X-Rays From Linear Accelerators.* Medical Physics Publishing, St. Louis, Missouri, 2004.

[3] W. Hendee and G. Ibbott. *Radiation Therapy Physics.* John Wiley and Sons Inc., Hoboken, New Jersey, 1996.

[4] H. Dobbs, N. Parker, P. Hobday and J. Husband. The Use of CT in Radiotherapy Treatment Planning. *Radiother. Oncol.*, 37:133–141, 1983.

[5] F. Khan. *The Physics of Radiation Therapy.* Lippincott, Williams, and Wilkins, Philadelphia, Pennsylvania, 2003.

[6] D. Yana and D. Lockman. Organ/Patient Geometric Variation in External Beam Radiotherapy and its Effects. *Medical Physics*, 28(4):593–602, 2001.

[7] K. Langen and D. Jones. Organ Motion and Its Management. *Int. J. Radiation Oncology Biol. Phys*, 50(1):265–278, 2001.

[8] A. Berson, R. Emery, L. Rodriguez, G. Richards, T. NG, S. Sanghavi, and J. Barsa. Clinical Experience Using Respiratory Gated Radiation Therapy: Comparison of Free-Breathing and Breath-Hold Techniques. *Int. J. Radiation Oncology Biol. Phys*, 60(2):419–426, 2004.

[9] F.H. Attix. *Introduction to Radiological Physics and Radiation Dosimetry.* Wiley-VCH Verlag, Strauss, Morlenbach, 2004.

[10] P. Almond, P. Briggs, B. Coursey, W. Hanson, M. Saiful Huq , R. Nath and D. Rogers. Ionization Chamber Dosimetry for Photon and Electron Beams. *Medical Physics*, 9:1847–1870, 1999.

[11] P. Almond and H. Svensson. Ionization Chamber Dosimetry for Photon and Electron Beams. *Acta Radiol. Ther. Phys. Biol.*, 16:177, 1977.

[12] C. Baldock. Historical Overview of the Development of Gel Dosimetry: A Personal Perspective. *Journal of Physics:Conference Series*, 56:14–22, 2006.

[13] J.C. Gore. Measurement of Radiation Dose Distributions by Nuclear Magnetic Resonance (NMR) Imaging. *Phys. Med. Biol.*, 29:1189–1197, 1984.

[14] J. Schreiner. Review of Fricke Gel Dosimeters. *Journal of Physics:Conference Series*, 3:9–21, 2004.

[15] J. Schulz, F. de Guzman, B. Nguyen and J. Gore. Dose-Response Curves for Fricke-Infused Agarose Gels as Obtained by Nuclear Magnetic Resonance. *Phys. Med. Biol.*, 35:1611–1622, 1990.

[16] P. Alexander, A. Charlesby and M. Ross. The Degradation of Solid Polymethylmethacrylate by Ionizing Radiations. In *Proceedings of the Royal Society*, page 392. 1954.

[17] C. Audet and J. Schreiner. Radiation Dosimetry by NMR Relaxation Time Measurements of Irradiated Polymer Solutions. In *Proceedings of Society of Magnetic Resonance in Medicine*. 1991.

[18] K. McAuley. Fundamentals of Polymer Gel Dosimeters. *Journal of Physics:Conference Series*, 56:35–44, 2006.

[19] A. Jirasek. *Fourier Transform Raman Spectroscopy of Polyacrylamide Gels for use in Radiation Dosimetry.* PhD thesis, 2002.

[20] J.L. Schreiner, A. Fuxman and K. McAuley. Modeling of Free-Radical Crosslinking Copolymerization of Acrylamide and N,N-Methylenebis(Acrylamide) for Radiation Dosimetry. *Macromolecular Theory and Simulations*, 12:647–662, 2003.

[21] R J Senden, P De Jean, K B McAuley, and L J Schreiner. Polymer gel dosimeters with reduced toxicity: a preliminary investigation of the nmr and optical dose-response using different monomers. *Physics in medicine and biology*, 51(14):3301–14, Jul 2006.

[22] J. Adamovics and M. Maryanski. A New Approach to Radiochromic Three-Dimensional Dosimetry-Polyurethane. *Journal of Physics:Conference Series*, 3:172–175.

[23] Y. Deene, K. Vergote. C. Claeys and C. Wagter. The Fundamental Radiation Properties of Normoxic Polymer Gel Dosimeters: A Comparison Between a Methacrylic Acid Based Gel and Acrylamide Based Gels. *Physics in Medicine and Biology*, 51(3):653, 2006.

[24] M.J. Maryanski, R.J. Schulz, G.S. Ibbott, J.C. Gatenby, J. Xie, D. Horton and J.C. Gore. Magnetic resonance imaging of radiation dose distributions using polymer gel dosimeters. *Phys. Med. Biol.*, 39:1437–1455, 1994.

[25] M. Lepage. Magnetic Resonance in Polymer Gel Dosimetry: Techniques and Optimization. *Journal of Physics:Conference Series*, 56:86–94, 2006.

[26] Y De Deene, C De Wagter, W De Neve, and E Achten. Artefacts in multi-echo T2 imaging for high-precision gel dosimetry: II. analysis of b1-field inhomogeneity. *Phys Med Biol*, 45(7):1825–39, 2000.

[27] M. Hilts, C. Audet, C. Duzenli and J. Robar. Polymer Gel Dosimetry Using X-Ray Computed Tomography: Feasibility and Potential Application to Stereotactic Radiosurgery. *Phys. Med. Biol.*, 45:2559–2571.

[28] M. Maryanski, G.S. Ibbott, P. Eastman, R.J. Schulz and J.C. Gore. Radiation Therapy Dosimetry Using Magnetic Resonance Imaging of Polymer Gels. *Med. Phys.*, 23(5):699–705, 1996.

[29] K. Jordan. Advances in Optical CT scanning For Gel Dosimetry. *Journal of Physics:Conference Series*, 3:115–121, 2004.

[30] M. Oldham and L. Kim. Optical-CT Gel-Dosimetry II: Optical Artifacts and Geometrical Distortion. *Med. Phys.*, 31:1093–1104, 2004.

[31] M.L. Mather, A.K. Whittaker and C. Baldock. Ultrasound Evaluation of Polymer Gel Dosimeters. *Phys. Med. Biol.*, 47:1449–1458, 2002.

[32] L. Rintoul, M. Lepage and C. Baldock. Radiation Dose Distribution in Polymer Gels by Raman Spectroscopy. *Applied spectroscopy*, 57(1):51–7, Jan 2003.

[33] G.T. Herman. *Image Reconstruction From Projections.* Academic Press, Oval Road, London, 1980.

[34] J. Radon. Uber Due Bestimmung Von Funktionen Durch Ihre Intergralwerte Langs Gewisser Mannigfaltigkeiten (On the Determination of Functions from Their Integrals Along Certain Manifolds). *Berichte Saechsische Akademie der Wissenschaften*, 29:262–277, 1917.

[35] J.T. Bushberg, J.A. Seibert, E.M. Leidholdt JR. and J.M. Boone. *The Essential Physics of Medical Imaging.* Lippincott, Williams and Wilkins, Philadelphia, Pennsylvania, 2002.

[36] W.R. Hendee and E.R. Ritenour. *Medical Imaging Physics.* Mosby-Year Book, Inc., St. Louis, Missouri, 1992.

[37] A.C. Kak and M. Slaney. *Principles of Computerized Tomographic Imaging.* IEEE Press, New York, New York, 1988.

[38] S. Webb. *The Physics of Medical Imaging.* Adam Hilger, Bristol, England, 1988.

[39] J. C Gore, M. Rande, M. J Maryanski, and R. J Schulz. Radiation Dose Distributions in Three Dimensions From Tomographic Optical Density Scanning of Polymer Gels: (i) Development of an Optical Scanner. *Phys. Med. Biol.*, 41:2695–2704, 1996.

[40] M. Oldham, J.H. Siewerdsen, A. Shetty, and D.A. Jaffray. High Resolution Gel Dosimetry by Optical-CT and MR Scanning. *Med. Phys.*, 28(7):1436–1445, 2001.

[41] K.J. Jordan, R.G. Kelly and J.J. Battista. Optical CT Reconstruction of 3D Dose Distributions Using the Ferrous Benzoic Xylenol (FBX) Gel Dosimeter. *Medical Physics*, 25:1741–1750, 1998.

[42] S.J. Doran, K.K. Koerkamp, M.A. Bero, P. Jenneson, E.J. Morton and W.B. Gilboy. A CCD-Based Optical CT Scanner for High-Resolution 3D Imaging of Radiation Dose Distributions: Equipment Specifications, Optical Simulations and Preliminary Results. *Phys. Med. Biol.*, 46:3191–3213, 2001.

[43] N. Krstajic and S.J. Doran. Characterization of a Parallel-Beam CCD Optical-CT Apparatus for 3D Radiation Dosimetry. *Phys. Med. Biol.*, 52:3693–3713, 2007.

[44] J. G Wolodzko, C. Marsden, and A. Appleby. CCD Imaging for Optical Tomography of Gel Radiation Dosimeters. *Med. Phys.*, 26(11):2508–2513, 1999.

[45] R. Senden, P. DeJean, K. McAuley, M. Rogers and L.J. Schreiner. Initial Experience With a Commercial Cone Beam Optical CT Unit for Polymer Gel Dosimetry I: Optical Dosimetry Issues. *Journal of Physics: Conference Series*, 56:179–182, 2006.

[46] M. Kerker. *The Scattering of Light and Other Electromagnetic Radiation.* Academic, New York, New York, 1969.

[47] C.F. Bohren and D.R. Huffman. *Absorption and Scattering of Light by Small Particles.* Wiley and Sons, New York, New York, 1998.

[48] N. Krstajic and S.J. Doran. Focusing Optics of a Parallel Beam CCD Optical Tomography Apparatus for 3D Radiation Gel Dosimetry. *Phys. Med. Biol.*, 51:2055–2075, 2006.

[49] P. Seutens. *Fundamentals of Medical Imaging.* Cambridge University Press, Cambridge, UK, 2002.

[50] M. Oldham, J.H. Siewerdsen, S. Kumar, J. Wong and D.A. Jaffray. Optical-CT gel-dosimetry I: Basic Investigations. *Med. Phys.*, 28(7):1436–1445, 2003.

[51] H. Sakhalkar M. Oldham and P. Guo. An Investigation of the Accuracy of an IMRT Dose Distribution Using Two- and Three-Dimensional Dosimetry Techniques. *Med. Phys.*, 35:2072–2080, 2008.

[52] R.E. Woods R.C. Gonzalez. *Digital Image Processing.* Prentice Hall, Upper Saddle River, New Jersey, 2002.